High spin correlations in topological and rainbow lattices

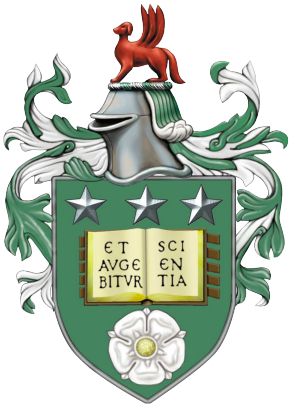

Lucy Sarah Byles

The University of Leeds
School of Physics and Astronomy

Submitted in accordance with the requirements for the degree of

Doctor of Philosophy

September, 2025

Declarations

The candidate confirms that the work submitted is her own, except where work which has formed part of jointly-authored publications has been included. The contribution of the candidate and the other authors to this work has been explicitly indicated below. The candidate confirms that appropriate credit has been given within the thesis where reference has been made to the work of others.

Chapter summary

- Chapter 2 of this thesis includes work appearing in: L. Byles, G. Sierra and J. K. Pachos. "Q-deformed rainbows: a universal simulator of free entanglement spectra". In: *New J. Phys.* 26 013055 (31 Jan. 2024). DOI: 10.1088/1367-2630/ad19f7 where all analytical and numerical work is attributed to me with the exception of the 'prime number spectrum' appearing in Section 2.6.2, which was devised by Germán Sierra. This work was conducted under the general guidance and supervision of Germán Sierra and Jiannis K. Pachos.

- Chapter 3 contains background material only and no published work.

- Chapter 4 includes work from the publication: L. Byles, E. Forbes and J. k. Pachos. "Demonstrating anyonic non-Abelian statistics with a minimal d = 6 qudit lattice". DOI: 10.48550/arXiv.2408.03377. arXiv: 2408.03377v2. The minimal anyonic system was conceived and designed by myself and Ewan Forbes. Subsequent analysis of this system was lead by myself with supporting discussion from Ewan Forbes. Figures 4.5 - 4.9 were developed in collaboration with Ewan Forbes. Sections 4.3.1 and 4.6 are unpublished additions to this work with magic state analysis performed by myself. This work was conducted under the guidance and supervision of Jiannis K. Pachos.

- Chapter 5 contains unpublished work. The dense encoding scheme and error analysis were performed by myself under the guidance and supervision of Jiannis k. Pachos. The linear optical circuits presented in Section 5.4 are attributed to Matthew D. Horner.

Acknowledgements

It feels only right to begin by thanking my supervisor, Professor Jiannis K. Pachos, without whom none of this would have been possible. I am deeply grateful for his support and guidance throughout the past four years, as well as for his infectious enthusiasm for all things quantum. I will be forever glad that picking up his textbook *'Introduction to Topological Quantum Computation'* as an undergraduate set me on the path that would eventually lead to this thesis. I would also like to thank Dr Almut Beige, whose advice on matters physics-related and otherwise has meant a great deal to me over the last few years.

A huge thanks must also go to the people who have made the last four years of the PhD some of the best so far. One of the constant highlights has been Dungeons and Dragons with the Birmingham physics gang; Patrick, Carlos, James, James, Sam, Maddie, Jonny, and Ari. Our fortnightly sessions and weekends away have meant so much to me that I can almost forgive you all for choosing to live so far away. Another great distraction from PhD life has been time spent climbing with Maya, Izzy, Sam, and Jack, (thank you to Maya and Izzy especially for making the weekday morning sessions fun enough to survive the early starts). To the theory group, past and present, thank you all for the fun times both in and out of the office and I look forward to many more Friday beers and pub quiz victories to come. I am also incredibly grateful to the Hubert Road girls; Annie, Erica, Hannah, Jas, and Alice, for reminding me that there is far more to life than studying and for keeping me from imploding under the pressure of past exam seasons. Alice especially, I am so glad that we both ended up in Leeds together; your stories of life as the *real* kind of doctor have been invaluable for putting bad days in the office into perspective. Finally, to Anna, my oldest best friend: however far apart we've been, you have been a constant source of support and encouragement throughout, and thank you for teaching me your peanut butter tofu recipe that has kept me going over the last few years.

Finally, and most of all, I thank my mum, my dad, and my sister. Truly, I would not be where I am without you, and I am endlessly grateful for your support, encouragement, and patience throughout this entire process. Thank you for being willing to travel so far up to come and visit me in Leeds, and for always giving me a place to flee when the thesis writing became too much. I really couldn't have asked for better people to have in my corner throughout it all.

Abstract

Quantum simulations are an invaluable tool in condensed matter physics, enabling the precise generation and control of physical phenomena abstracted from the complexity of the underlying many-body system. At the heart of such complexity lies entanglement, the intrinsically quantum correlations that have attracted renewed interest as a fundamental resource in quantum computation and information. In this thesis, we explore the use of one- and two-dimensional lattice models to simulate and harness such correlations for next-generation quantum technologies.

We begin in one dimension with a spin-chain model that allows complete control over bipartite correlation structures. Specifically, we introduce a model of nearest-neighbour couplings and transverse field terms, whose exact solution yields a q-deformed rainbow ground state formed from a tensor product of q-deformed singlets, each with directly tunable entanglement. This framework acts as a universal simulator of free-fermion entanglement spectra, with numerical studies confirming high-fidelity realisations across a range of examples.

We then turn to strong correlations in two dimensions, where topologically ordered systems host exotic quasiparticles known as anyons. Braiding non-Abelian anyons enacts unitary transformations on a logically encoded fusion space, offering a natural pathway to fault-tolerant quantum computation. Using Kitaev's quantum double model $\mathbf{D}(\mathbf{G})$, we focus on the smallest non-Abelian instance, $\mathbf{D}(\mathbf{S}_3)$, realised on a lattice of $d = 6$ qudits. We develop a minimal protocol in which braiding and fusion are simulated solely through operators that create and measure anyons, demonstrating that $\mathbf{D}(\mathbf{S}_3)$ anyons generate magic states, a vital resource for universal quantum computation. Finally, a dense encoding scheme is presented, rendering the minimal realisation of this protocol accessible with current quantum technologies and a circuit model for realisation within the framework of linear optics is presented. Notably, error analysis of this encoding scheme reveals an inherent passive protection provided by the topological encoding, extending beyond conventional notions of topological fault tolerance.

List of Abbreviations, Symbols and Conventions

Abbreviations

LOCC	Local Operations and Classical Communication
RG	Renormalization Group

Symbols

S_A	Von Neumann entropy for subsystem A
$SU(n)$	The special unitary group of degree n
$SU(n)_q$	The q-deformation of $SU(n)$
q	Deformation parameter
ϵ_i	Single-particle entanglement energy
J_i, h_i	Coupling and magnetic field terms for the Hamiltonian $\mathcal{H}_n$
$\tilde{J}_i$, $\tilde{h}_i$	Effective coupling and magnetic field terms from the RG approach
R^{ab}	The braiding matrix for anyons a and b
F_d^{abc}	The fusion matrix for anyons a, b and c fusing to d
$\mathcal{B}_n$	The n-strand braid group
b_i	The braid group generator for the clockwise exchange of strands i and $i+1$
$\mathbf{S}_3$	The permutation group of three objects
$\mathcal{C}$	Conjugacy class
Γ	Irreducible representation
χ^Γ	Character of the irreducible representation Γ

Conventions

The Pauli matrices are given by

$$\sigma^x = \begin{pmatrix} 0 & 1 \\ 1 & 0 \end{pmatrix}, \qquad \sigma^y = \begin{pmatrix} 0 & -i \\ i & 0 \end{pmatrix}, \qquad \sigma^z = \begin{pmatrix} 1 & 0 \\ 0 & -1 \end{pmatrix}.$$

The inhomogeneous XX model refers to the Hamiltonian

$$\mathcal{H}_{XX} = \frac{1}{2}\sum_{i=1}^{N} J_i \left(\sigma_i^x \sigma_{i+1}^x + \sigma_i^y \sigma_{i+1}^y\right),$$

acting on N spin-$\frac{1}{2}$ particles.

Contents

List of Figures

Chapter 1

Introduction

1.1 Motivation

"More is different," as P. W. Anderson famously declared over half a century ago [1], remains a foundational principle of modern physics. At its heart lies the concept of emergence: the idea that large assemblies of particles, each governed by simple and well-understood microscopic laws, can collectively give rise to novel macroscopic phenomena that cannot be inferred from their parts in isolation. Such interactions underpin key phenomena in condensed matter physics, including superconductivity [2, 3], topological phases of matter [4, 5, 6], and quantum magnetism [7, 8, 9]. A central challenge in the study of quantum many-body systems therefore lies in our ability to describe and categorise these underlying structures of correlations that give rise to such emergent behaviour.

In the traditional sense, this interconnectivity may be understood through the strength of interactions that arise when particles influence one another directly. In quantum mechanics, however, a more abstract notion of correlation emerges in the form of entanglement. This 'spooky action at a distance' describes the phenomenon whereby the states of two or more particles cannot be specified independently, even when separated by large distances. Entanglement therefore lies at the core of the distinction between classical and quantum

descriptions of nature and has remained a central focus of both theoretical investigation [10, 11, 12] and experimental verification [13, 14, 15, 16] of quantum mechanics. More recently, entanglement has also emerged as an important resource within quantum information and computation, whereby the complex interplay between constituent particles can be harnessed to achieve exponential reductions in computational cost. Indeed, entanglement underpins a wide range of quantum protocols [17, 18], with several schemes, such as teleportation [19, 20], able to be realized exclusively with the use of entangled states.

In recent years, one of the central challenges in quantum science has been the construction of a universal quantum computer. Such a device offers the potential to harness the power of quantum mechanics to solve problems otherwise intractable on purely classical hardware [21]. A particularly appealing route toward this goal is provided by topological quantum computation [22], which exploits the manipulation of exotic quasiparticles that emerge in strongly correlated two-dimensional systems known as *anyons* [23]. The braiding of these anyons enacts unitary operations on a topologically protected fusion space, offering a model of computation that is inherently robust against local sources of environmental noise [24, 25]. However, the physical systems expected to host such anyons, such as fractional quantum Hall states or topological superconductors, remain highly complex and experimentally challenging to control [26, 27, 28, 29]. To address this challenge, lattice simulations provide an exactly solvable framework for the controlled creation and manipulation of non-Abelian anyons within a strongly correlated setting. It is within this context that the present thesis explores the use of spin lattice models in simulating, characterising, and ultimately harnessing emergent quantum correlations as practical resources for quantum computation.

1.2 Structure of thesis

This thesis is structured as follows.

Chapter 2

Non-interacting models give rise to highly ordered structures of ground state correlations with the potential to facilitate exponential reductions in complexity. In this chapter we present a spin-$\frac{1}{2}$ chain with position-dependent XX couplings and magnetic fields, that can reproduce arbitrary structure of free fermion correlations across a bipartition. In particular, by choosing appropriately the strength of the magnetic fields we can obtain any single particle energies of the entanglement spectrum with high fidelity. To demonstrate the versatility of our method we consider certain examples, such as a system with homogeneous correlations and a system with correlations that follow a prime number decomposition.

Chapter 3

In this chapter we present relevant background material for Chapters 4 and 5. We provide an overview of the structure of anyon models and the basic operations they support. We then introduce Kitaev's quantum double model, in which these anyons appear as localised excitations on a lattice of d-dimensional spins.

Chapter 4

Lattice implementations of anyonic models offer a powerful framework to explore non-Abelian statistics while realising intrinsic quantum error correction. In this chapter we consider a lattice of $d = 6$ qudits that supports $\mathbf{D}(\mathbf{S}_3)$ non-Abelian anyons. We present a method for implementing both braiding and fusion evolutions using only static combinations of the operators that create and measure anyons. This provides a minimal and fully topological protocol, demonstrating that $\mathbf{D}(\mathbf{S}_3)$ anyons can generate magic states, an essential resource for universal quantum computation.

Chapter 5

In this chapter, we present a dense encoding of the protocol introduced in Chapter 4, enabling a proposed implementation of the non-Abelian quantum double model $\mathbf{D}(\mathbf{S}_3)$ on a photonic simulator. Within this framework, we demonstrate the fault-tolerant execution of key anyonic operations, including braiding and fusion, and identify a noise threshold below which the anyonic encoding surpasses conventional gate-based approaches.

Our analysis shows that topological encoding in photonic platforms remains robust against dominant error channels, such as dephasing, without requiring active error correction or dynamical protection. This intrinsic resilience highlights photonic systems as a natural platform for scalable anyonic quantum computation.

Chapter 6

We then close this thesis with concluding remarks and discussion.

Chapter 2

Q-Deformed Rainbows: a Universal Simulator of Free Entanglement Spectra

2.1 Introduction

Quantum entanglement is simultaneously one of the most fundamental and perplexing features of quantum mechanics. Arising from the superposition principle of quantum states, entanglement refers to the phenomenon whereby the quantum state of a composite system cannot be decomposed into independent states of its constituent parts, even when those parts are spatially separated. As a consequence, measurements performed on one subsystem can exhibit correlations with outcomes on another that cannot be explained classically. For many years, the existence of such a phenomenon was widely disputed, being believed to be in direct contradiction with accepted ideas of local realism [10, 30, 31]. In 1964 however, John Bell formulated a theoretical framework for analysing correlations between two entangled spin-$\frac{1}{2}$ particles, showing that there is a measurable contradiction between the statistical predictions of quantum mechanics and those of any local realistic or 'hidden variables' theory [12]. These results culminated in a set of

inequalities, now known as the 'Bell inequalities', which must hold true for any local realistic description of such a system. Later, experimental results demonstrated the violation of these Bell inequalities, providing explicit experimental verification for the quantum mechanical description of entanglement in many-body systems [32, 33, 13].

For pure bipartite systems, two chosen subsystems A and B are described as entangled if the pure state $|\psi\rangle$ describing the composite system cannot be expressed as a tensor product of pure states in the individual subsystems, i.e.,

$$|\psi\rangle \neq |\psi_A\rangle \otimes |\psi_B\rangle \,. \tag{2.1}$$

States of the form $|\psi_A\rangle \otimes |\psi_B\rangle$ are referred to as product states and exhibit no non-classical correlations between the degrees of freedom of subsystems A and B. Beyond its foundational role in quantum theory, the characterisation of quantum correlations within such entangled states has become central to quantum information theory [34, 35]. Within this framework, quantum entanglement is viewed as a valuable resource [36], enabling information-processing tasks that would be impossible (or highly inefficient) within classical or separable quantum frameworks. A paradigmatic example is provided by superdense coding, in which the use of a shared entangled pair of spin-$\frac{1}{2}$ particles allows two classical bits of information to be transmitted through the communication of a single qubit [37]. This perspective has motivated extensive research into the generation, manipulation, and structural characterisation of entanglement in quantum many-body systems, where distinct entanglement patterns are known to underpin a wide range of physical phenomena [38].

The formal characterisation of these quantum correlations naturally requires the introduction of measures for their quantification (as will be discussed further in Section 2.2). One such choice of measure is the entanglement entropy S_A, defined as the von Neumann entropy of the reduced density matrix $\rho_A = \mathrm{Tr}_B\left(|\psi\rangle\langle\psi|\right)$ of a bipartite system

$$S_A = -\mathrm{Tr}(\rho_A \log(\rho_A)). \tag{2.2}$$

In addition to the detection of entanglement, the scaling behaviour of the entanglement entropy with variation of the bipartition also encodes the properties of the underlying physical system. The ground states of local quantum lattice Hamiltonians for example, typically obey an 'area law' such that the entanglement entropy is proportional to the size of the boundary of the chosen subsystem, A [39, 40]. In 2010, Vitagliano, Riera and Latorre demonstrated that continuous tuning of the parameters of the inhomogeneous XX model allowed for a controlled transition of the ground state entanglement entropy from obeying an area law to a volume law [41]. The ground state of this model is termed the 'concentric singlet phase' [41] or simply 'rainbow state' [42], due to its distinctive structure of maximally entangled valence bonds connecting pairs of sites distributed symmetrically across the centre of the chain. This simple model hosts a rich variety of properties [43, 44] and has been the subject of much interest in recent years [45, 46, 47, 48].

In this work we present a generalisation of the rainbow state model, whereby, with the introduction of staggered transverse field terms to the inhomogeneous XX model, the degree of entanglement between each concentric pair on the chain can be independently varied. Using a Real-Space Renormalization Group approach we derive recursive expressions for the induced effective coupling and transverse field terms. These expressions have an elegant description in terms of the formalism of q-deformed algebra [49, 50]. For a chain of $2N$ sites the ground state is a tensor product of N concentric q-deformed singlets, each with an associated deformation parameter, q_i, dependent on the transverse field and coupling parameters of our model. The variation of these physical parameters allows for the generation of any arbitrary set of single-particle entanglement energies, thereby enabling the complete controllability of entanglement within this bipartite system. This model thus serves as a powerful resource for quantum technologies that require the simulation of specific patterns of quantum correlations [51, 52, 53]. To verify the validity of our results we perform a detailed numerical analysis. This analysis reveals that appropriate choices of the values of the transverse field parameter, and ordering of the degree of entanglement ensures a high fidelity between the exact ground state and the q-deformed

rainbow.

In order to demonstrate the applicability of our method, we consider two special cases. First, we consider the homogeneous case $q_1 = q_2 = \cdots = q_N$ such that each concentric pair has the same degree of entanglement, mirroring the concentric singlet state of the rainbow chain but generalized to arbitrary degrees of entanglement. Second, we explore a scenario presented by Germán Sierra, where the entanglement energies of individual particles follow what we refer to as the 'prime number spectrum,' or more precisely, are given by the logarithm of the prime numbers. Under this particular choice, the eigenvalues of the density matrix become the so-called square-free integers, which are integers whose prime factorization solely comprises individual prime numbers without any higher powers. In this way our model highlights an interesting connection between the decomposition of free-system entanglement spectra in terms of single particle energies and the decomposition of integers in terms of prime numbers.

This chapter is organised as following. In Section 2.2, we provide a brief overview of the manifestation of entanglement within pure states on a bipartite lattice. In particular, it is shown that the structure of correlations in free-fermion systems allows for the exponential simplification of the entanglement spectrum in terms of a set of single-particle entanglement energies $\{\epsilon_i\}$. In Section 2.3 we introduce a one-dimensional simple spin model composed of variable nearest-neighbour coupling and transverse field terms. Through the application of a real-space renormalization group approach, an exact description of the ground state is found in terms of concentric pairs of q-deformed singlets. In Section 2.4, we analyse the entanglement properties of this exact ground state, demonstrating that specific selection of the coupling and transverse field terms allows for the exact tuning of the single-particle entanglement energies that completely define the full entanglement spectrum. A fidelity optimisation protocol is introduced in Section 2.5 and its efficacy explicitly demonstrated with application to two specific case scenarios in Section 2.6. Finally, in Section 2.7, we provide concluding remarks and outlook.

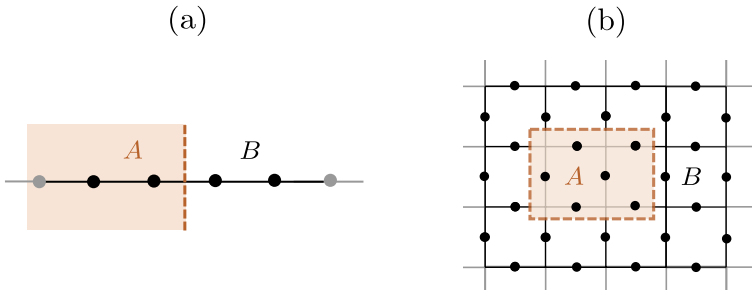

Figure 2.1: Bipartitions of (a) one-dimensional and (b) two-dimensional lattice models into complimentary subsystems A and B.

2.2 Entanglement in bipartite systems

Consider a quantum many-body system partitioned into two complementary subsystems A and B as illustrated in Figure 2.1. The states of each subsystem are elements of the corresponding Hilbert spaces, $|\psi_A\rangle \in \mathbf{H}_A$ and $|\psi_B\rangle \in \mathbf{H}_B$, respectively. The Hilbert space of the total bipartite system is thus given by the tensor product of the subsystem Hilbert spaces,

$$\mathbf{H} = \mathbf{H}_A \otimes \mathbf{H}_B, \tag{2.3}$$

such that the total state vector satisfies $|\psi\rangle \in \mathbf{H}_A \otimes \mathbf{H}_B$. A pure state $|\psi\rangle$ is said to be entangled if it cannot be expressed as a tensor product of pure states in the individual subsystems, i.e.,

$$|\psi\rangle \neq |\psi_A\rangle \otimes |\psi_B\rangle \,. \tag{2.4}$$

States of the form $|\psi_A\rangle \otimes |\psi_B\rangle$ are referred to as product states and exhibit no entanglement between the degrees of freedom of subsystems A and B. The condition for factorisability can be formalised through the Schmidt decomposition [54], which asserts that any pure state $|\psi\rangle$ of the composite system can be written as

$$|\psi\rangle = \sum_{i=1}^{\chi} \alpha_i \, |i_A\rangle \otimes |i_B\rangle \,, \tag{2.5}$$

where $\{|i_A\rangle\}$ and $\{|i_B\rangle\}$ form orthonormal bases for $\mathbf{H}_A$ and $\mathbf{H}_B$ respectively, and $\{\alpha_i\}$ are positive real Schmidt coefficients satisfying $\sum_i |\alpha_i|^2 = 1$. The integer χ, known as the Schmidt rank, obeys $1 \leq \chi \leq \min(\dim(\mathbf{H}_A), \dim(\mathbf{H}_B))$, with $\chi > 1$ necessarily indicating entanglement between A and B.

For such a bipartite system one may define the reduced density matrix across a given subsystem. For subsystem A

$$\rho_A = \mathrm{Tr}_B \left(|\psi\rangle \langle\psi| \right), \tag{2.6}$$

where Tr_B denotes the partial trace over the degrees of freedom of B. The reduced density matrix ρ_A fully characterises the state of subsystem A and possesses eigenvalues $\{\lambda_i\}$ equal to the squared Schmidt coefficients, $\lambda_i = |\alpha_i|^2$ [55]. These eigenvalues encode the bipartite correlations between A and B and satisfy the normalisation condition $\mathrm{Tr}(\rho_A) = \sum_i \lambda_i = 1$.

The reduced density matrix for the pure states of a bipartite system completely describes the correlations between the two subsystems. When it comes to quantifying these correlations however, there exist a variety of measures to choose from, each with distinct, yet closely related, physical interpretations [56]. Here we briefly introduce the two measures most relevant for our study of tuneable quantum correlations, outlining their particular suitability for the analysis of non-interacting one-dimensional spin chains as will be relevant for our model introduced in Section 2.3.

The entanglement entropy, S_A, is defined as the von Neumann entropy of the reduced density matrix, ρ_A, via

$$\begin{aligned} S_A &= -\mathrm{Tr}(\rho_A \log(\rho_A)), \\ &= -\sum_i \lambda_i \log(\lambda_i). \end{aligned} \tag{2.7}$$

For a pure product state $|\psi_A\rangle \otimes |\psi_B\rangle$, ρ_A is itself a pure state, and $S_A = 0$. Conversely, for a system of N spin-$\frac{1}{2}$ particles, the subsystem A containing $L \leq \frac{N}{2}$ sites is maximally entangled with B when $S_A = L \log(2)$. For all pure states as will be considered here, the

entanglement entropy is also notably identical across a given bipartition for each subsystem, i.e. $S_A = S_B$. The entanglement entropy is widely recognised as the foundational quantifier of pure-state entanglement [57]. Indeed several other common entanglement monotones [58] including concurrence [59] and entanglement of formation [60, 61], reduce to the entanglement entropy for such pure states. An additional common generalization of the von Neuman entanglement entropy is the Renyi entropy [62, 63]

$$S_A^{(\alpha)} = \frac{1}{1-\alpha} \log\left(\mathrm{Tr}(\rho_A^{\alpha})\right), \tag{2.8}$$

which returns the familiar measure S_A in the limit $\alpha \to 1$.

Although the von Neumann entropy provides a useful scalar measure of a quantum state's entanglement, in 2008 Li and Haldane demonstrated that the full spectrum of eigenvalues of the reduced density matrix $\{\lambda_i\}$ can provide a more detailed characterisation of the correlations within a system [64]. This 'entanglement spectrum', $\{E_i\}$, constructed as

$$E_i = -\log(\lambda_i), \tag{2.9}$$

may be viewed as the eigenvalues of an 'entanglement Hamiltonian' $\mathcal{H}_{\mathrm{ent}} = -\log(\rho_A)$ acting only on the degrees of freedom of subsystem A [65, 66, 67, 68]. This exponential relationship, $\lambda_i = e^{-E_i}$, results in the dominant quantum correlations depending predominantly on the 'lowest' part of the entanglement spectrum. In the case of a weak entanglement, the 'excited states' eigenvalues of H_{ent} are separated from the ground state eigenvalue by a large energy gap [69]. In the special case of a simple product state with vanishing entanglement entropy, this energy gap tends to infinity as there is only one non-zero eigenvalue of the reduced density matrix over either subsystem.

The entanglement spectrum serves as a powerful diagnostic tool for the properties of the 'parent' Hamiltonian, $\mathcal{H}$. This was first demonstrated by Li and Haldane in the context of fractional quantum Hall systems, whereby the low-lying levels of the entanglement spectrum were shown to reflect the gapless edge excitations predicted by the

bulk–boundary correspondence [64]. More generally, the structure of the entanglement spectrum can reveal the presence of topological order [70, 71, 72, 73], symmetry-protected phases [74], and conformal field theory spectra in critical systems [75]. Interestingly, the entanglement Hamiltonian $\mathcal{H}_{\text{ent}}$ is often shown to directly inherit features of the parent Hamiltonian $\mathcal{H}$. In particular, spin models that map to free fermion systems necessarily also have Gaussian entanglement Hamiltonians (see Appendix A.1). Such non-interacting models as we will discuss in the following, have entanglement spectra fully described in terms of a reduced set of single-particle energies $\{\epsilon_i\}$. This exponential reduction in complexity directly facilitates the construction of our universal simulator of free entanglement spectra as will be introduced in Section 2.3.

2.2.1 Free fermion models

In the context of quantum spin systems, a model is termed non-interacting if its many-body dynamics can be reduced to a set of independent single-particle modes, such that the full Hamiltonian decomposes into a sum of commuting single-particle contributions. For spin-$\frac{1}{2}$ lattice models, as considered here, such an analysis can be performed via a mapping from Pauli spin operators to fermionic or bosonic mode operators.

Consider, for example, the XX model consisting of a chain of N spin-$\frac{1}{2}$ particles with nearest neighbour interactions and an external magnetic field. The Hamiltonian for this model takes the form

$$\mathcal{H}_{XX} = \frac{1}{2}\sum_{i=1}^{N-1}(\sigma_i^x\sigma_{i+1}^x + \sigma_i^y\sigma_{i+1}^y), \tag{2.10}$$

where i labels the spin under action and σ_i^μ with $\mu = x, y, z$ are the respective Pauli matrices acting at site i. With the application of the Jordan-Wigner transformation [76, 77, 78] this chain of spins may be mapped onto an equivalent system of fermions. This transformation takes the form

$$c_i = \left(\prod_{j=0}^{i-1}\sigma_j^z\right)\frac{\sigma_i^x - i\sigma_i^y}{2}, \tag{2.11}$$

such that by construction these fermionic mode operators c_i, satisfy the canonical commutation relations $\{c_i^\dagger, c_j\} = \delta_{ij}$, $\{c_i, c_j\} = 0$. Under this mapping, the XX Hamiltonian becomes

$$\mathcal{H}_{XX} = \sum_{i=0}^{N-1} (c_i^\dagger c_{i+1} + c_{i+1}^\dagger c_i), \tag{2.12}$$

describing the nearest-neighbour hopping of spinless fermions on a one-dimensional lattice [79]. Crucially, all operator products are at most quadratic in the mode operators c_i. There are no higher order terms, such as $c_i^\dagger c_j^\dagger c_i c_j$, which would mediate 'interactions' between fermions.

The general form of such a quadratic fermionic Hamiltonian may be given by

$$\mathcal{H} = \sum_{i,j=1}^{N} \left[A_{ij} c_i^\dagger c_j + \frac{1}{2}(B_{ij} c_i^\dagger c_j^\dagger + \text{h.c.}) \right], \tag{2.13}$$

where the Hermiticity of $\mathcal{H}$, requires that the $N \times N$ matrices A and B must be Hermitian and anti-symmetric respectively. The terms $c_i^\dagger c_i$ denote on-site chemical potential terms, while $(c_i^\dagger c_j^\dagger + c_i c_j)$ describe 'superconducting' or 'pairing' terms typically due to the coupling of the system with a bath.

In general, obtaining the exact solution of a model on N sites requires the diagonalisation of the 2^N-dimensional Hamiltonian $\mathcal{H}$. Here we show however, that in the absence of such superconducting terms ($B = 0$), the diagonalisation of Hamiltonians of the form (2.13) can be achieved via the exponentially simpler diagonalisation of the N-dimensional kernel Hamiltonian A.

The eigenmodes in the diagonal basis of $\mathcal{H}$, are given by a linear combination of the original modes as

$$\tilde{c}_j^\dagger = \sum_{i=1} u_{ij} c_i^\dagger, \tag{2.14}$$

where u is the $N \times N$ unitary that diagonalises A. In terms of these new modes, the Hamiltonian $\mathcal{H}$ becomes

$$\mathcal{H} = \sum_{j=1}^{N} \epsilon_j \tilde{c}_j^\dagger \tilde{c}_j, \tag{2.15}$$

with eigenenergies

$$\epsilon_j = (u^\dagger A u)_{jj}, \quad j = 1, 2, \ldots, N. \tag{2.16}$$

In this new basis of states $\tilde{c}_j^\dagger |0\rangle$, the system is described by a set of N independent uncorrelated modes. The unitarity of u preserves the fermionic properties of the transformed mode operators such that $\{\tilde{c}_i^\dagger, \tilde{c}_j\} = \delta_{ij}$ and $\{\tilde{c}_i, \tilde{c}_j\} = 0$. We note that the number operators $\tilde{n}_j = \tilde{c}_j^\dagger \tilde{c}_j$ trivially commute with the Hamiltonian

$$[\tilde{n}_j, \mathcal{H}] = 0, \tag{2.17}$$

such that the populations of the new modes are well-defined quantum numbers, uniquely labelling the eigenstates of the system. This diagonalization results in an exponential reduction in complexity in the description of the properties of the system [80]. Since the Hamiltonian is diagonal in the occupation-number basis of the modes $\tilde{c}_j$, its eigenstates are given by Fock states of the form

$$|\{n_j\}\rangle = \prod_{j=1}^{N} (\tilde{c}_i^\dagger)^{n_j} |\mathbf{0}\rangle \,, \tag{2.18}$$

where each occupation number n_j can take only the values 0 or 1 due to the Pauli exclusion principle. Each such configuration corresponds to a distinct many-body eigenstate. As there are two possible occupations for each of the N independent modes, the total number of many-body eigenstates is 2^N, matching the dimension of the fermionic Hilbert space. The energy of a given many-body state is simply the sum of the single-particle energies ϵ_j associated with the occupied modes. For example, the complete many-body energy spectrum, consisting of 2^N distinct eigenvalues, is generated by the N single-particle energies $\{\epsilon_j\}$ according to

$$E_k^f(\{\epsilon\}) = E_0 + \sum_{j=1}^{N} \epsilon_j n_j(k), \quad k = 1, 2, \ldots, N, \tag{2.19}$$

where ϵ_j are the single-particle energies as defined in Eq. (2.16), k runs over the many-body spectrum and E_0 is some reference 'vacuum energy'. Note that in the case of free fermions the Pauli exclusion principle dictates that $n_j(k) \in \{0, 1\}$, whereas for bosonic systems $n_j(k)$ has no upper bound.

In the presence of additional superconducting terms, an analogous procedure may be performed with the inclusion of $c_i^\dagger$ terms in the definition of $\tilde{c}_j$ as in Eq. (2.14) [81]. All free fermion Hamiltonians as in (2.13) therefore describe analytically tractable models circumventing the exponential growth in complexity arising in generic quantum many-body systems. Despite their simple structure however, these exactly solvable models host a range of non-trivial physical phenomena [80]. For example, with the inclusion of non-interacting transverse field terms σ_i^z, the free-fermion Hamiltonian $\mathcal{H}_{XX}$ provides a direct platform for the observation of a quantum phase transition [82]. Additionally, the reduced structure of these models often enables simplified descriptions of the correlations between different constituent subsystems [83, 84]. In particular, as demonstrated in Appendix A.1, the entanglement spectrum of a spin model described by non-interacting fermions may also be expressed in the form (2.19). In the following, we exploit this exponential simplification in complexity, with the introduction of a non-interacting model for which the tuning of the physical parameters allows for the exact generation of the N single-particle energies completely defining the full 2^N-value entanglement spectrum.

2.3 The q-Deformed Model

In the previous section, we reviewed approaches to characterising entanglement in pure bipartite states, with particular emphasis on the entanglement spectrum, which encodes the complete correlations between subsystems through the eigenvalue structure of the reduced density matrix. In this section, we introduce a local spin chain of $2N$ sites whose free-fermion structure admits the entanglement spectrum decomposition of Eq. (2.19). By varying the physical parameters of the model, one achieves direct control over the single-particle energies and, consequently, the full entanglement spectrum, thereby enabling

precise manipulation of free-fermion correlations in a one-dimensional chain.

In order to introduce our model for a chain of $2N$ spin-$\frac{1}{2}$ particles, we first present a two-site Hamiltonian that allows for direct continuous variation of the degree of entanglement between its spins.

2.3.1 Two-Spin Hamiltonian

Consider the two-spin Hamiltonian

$$\mathcal{H}_{(1)} = J_1 \left(\sigma_{-1}^x \sigma_1^x + \sigma_{-1}^y \sigma_1^y\right) + h_1 \left(\sigma_{-1}^z - \sigma_1^z\right), \tag{2.20}$$

where $\sigma_i^{x,y,z}$ are the standard Pauli matrices acting on site i of the chain with labelling as shown in Figure 2.2(a). J_1 describes a relative coupling strength between the two spins, while h_1 moderates magnetic field terms anti-symmetric about the centre of the chain. The ground state of $\mathcal{H}_(1)$ is given by

$$|\psi_1\rangle = \frac{1}{\sqrt{[2]_{q_1}}} \left(q_1^{-\frac{1}{2}} |\uparrow\downarrow\rangle_{-1,1} - q_1^{\frac{1}{2}} |\downarrow\uparrow\rangle_{-1,1}\right), \tag{2.21}$$

and has ground state energy

$$E_1 = -[2]_{q_1} J_1, \tag{2.22}$$

where

$$q_1 = e^{\gamma_1}, \;\; \sinh\gamma_1 = \frac{h_1}{J_1}, \tag{2.23}$$

and $[x]_q$ is the so-called quantum dimension

$$[x]_q = \frac{q^x - q^{-x}}{q - q^{-1}}. \tag{2.24}$$

This ground state is the singlet of the quantum group $SU(2)_{q_1}$ [85]. Such q-deformed valence bonds have been considered in relation to a range of many-body models (see Appendix A.2) [86, 87, 88, 89], including the anisotropic q-deformed generalization of

the spin-1 AKLT chain as considered in [90, 91]. In the limit $h_1 \to 0$ such that $q_1 \to 1$, we recover the maximally entangled singlet state of the standard $SU(2)$ Lie algebra. The degree of entanglement between this pair is directly related to the value of the deformation parameter, q_1, which is in turn directly related to our coupling and transverse field parameters via equation (2.23). To investigate this, we bipartition the system down the centre of the chain into region A, and its complement B. The reduced density matrix of (2.21) is then determined for region A. The corresponding Rényi entropy of order α is given by

$$S_{A,1}^{(\alpha)} = \frac{1}{1-\alpha} \ln \frac{1+q_1^{2\alpha}}{(1+q_1^2)^\alpha}, \qquad \alpha > 0, \alpha \neq 1 \tag{2.25}$$

and takes the maximum value $\ln 2$ when $q_1 = 1$ for all α as shown in Figure 2.2(b). This expression for the Rényi entropy reflects a symmetry of our model as under the transformation $h_1 \to -h_1$, such that $q_1 \to \frac{1}{q_1}$, the value of the Rényi entropy of order α is unchanged.

By considering the limit of $S_{A,1}^{(\alpha)}$ as $\alpha \to 1$ we obtain the expression for the von Neumann entanglement entropy of the pair

$$S_{A,1} = \ln(1+q_1^2) - \frac{q_1^2}{1+q_1^2} \ln q_1^2. \tag{2.26}$$

This entropy can be varied continuously to achieve all values in the maximal range $0 \leq S_{A,1} \leq \ln 2$, by varying $0 \leq q_1 \leq \infty$, or equivalently $-\infty \leq \frac{h_1}{J_1} \leq \infty$. We see that by varying the physical parameters of our model we can achieve all degrees of pairwise entanglement between the two spins.

2.3.2 $2N$-Spin Hamiltonian

The simple two-spin Hamiltonian presented above is the basis on which we construct our general model for a chain of any even number of spins. We now consider a chain of $2N$

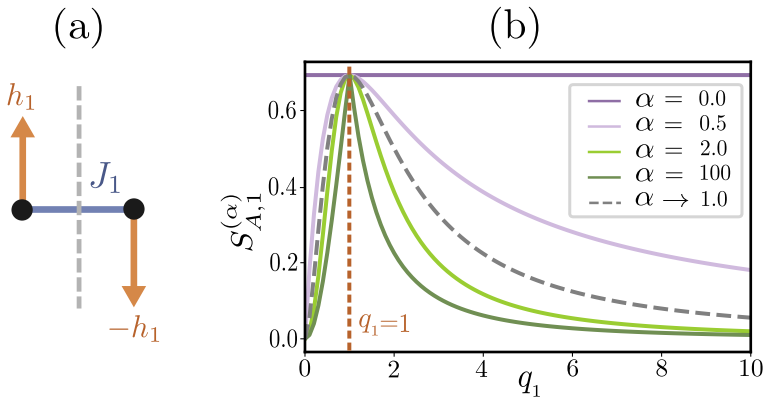

Figure 2.2: (a) The two-spin Hamilonian $\mathcal{H}_1$ with coupling strength J_1 and anti-symmetric transverse field terms h_1. (b) The variation of the Rényi entropy, $S^{(\alpha)}_{A,1}$ for the groundstate of this model (2.21) as a function of the deformation parameter q_1, for a range of fixed values of α.

spin-$\frac{1}{2}$ particles with the following Hamiltonian

$$\mathcal{H}_{(N)} = \sum_{i=1}^{N} h_i \left(\sigma^z_{-i} - \sigma^z_i\right) + J_1 \left(\sigma^x_{-1}\sigma^x_1 + \sigma^y_{-1}\sigma^y_1\right) + \sum_{i=2}^{N} J_i \left(\sigma^x_{-i}\sigma^x_{-(i-1)} + \sigma^y_{-i}\sigma^y_{-(i-1)} + \sigma^x_{i-1}\sigma^x_i + \sigma^y_{i-1}\sigma^y_i\right). \quad (2.27)$$

We have introduced the site labelling $\{-N, -(N-1), \ldots, -2, -1, 1, 2, \ldots, N-1, N\}$ such that sites $-i$ and i are equidistant from a central bipartition of the chain, as shown in Figure 2.3. In order to find the ground state of our model we use the Real-Space Renormalization Group approach as first introduced by Ma and Dasgupta in [92] and later developed by Fisher with the application of the method to the Random Transverse Field Ising Chain [93, 94]. This approach allows us to consider the ground state properties of random quantum chains by iteratively decimating the degrees of freedom with highest energy in order to derive an overall effective low-energy model.

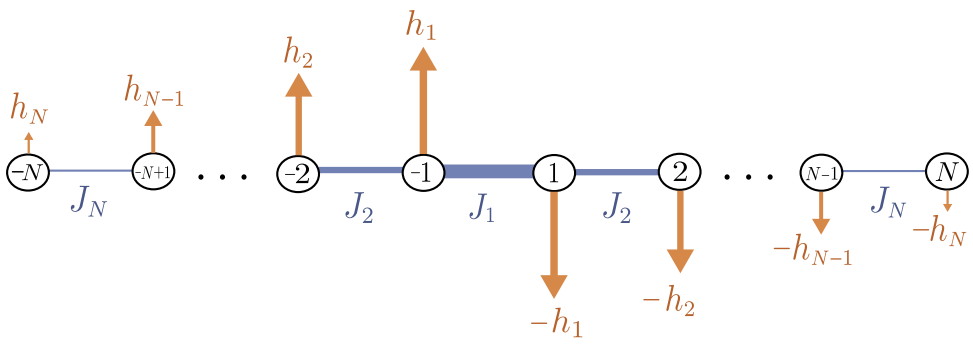

Figure 2.3: The q-deformed spin model for a chain of $2N$ sites. The blue lines represent the XX coupling terms, J_i, and the orange arrows represent the magnitude and direction of the transverse magnetic field, h_i. The magnitude of both the coupling and transverse field are symmetric about the centre of the chain, with decreasing strength moving outwards.

Rainbow Model Renormalization Group

In the limit, $h_i = 0$, our Hamiltonian (2.27) is equivalent to that of the inhomogeneous XX model acting on a chain of $2N$ spins

$$\mathcal{H}_{XX} = \sum_{i=1}^{2N} J_i \left(\sigma_i^x \sigma_{i+1}^x + \sigma_i^y \sigma_{i+1}^y\right), \tag{2.28}$$

where we have re-adopted the standard site labelling $\{1, 2, \ldots, 2N-1, 2N\}$. Using the Renormalization Group (RG) approach for some random coupling profile, the highest energy term such that $J_i \gg J_{i-1}, J_{i+1}$, is identified and diagonalised independently of the rest of the chain. The local Hamiltonian $J_i \left(\sigma_i^x \sigma_{i+1}^x + \sigma_i^y \sigma_{i+1}^y\right)$ has a unique singlet ground state separated from the excited triplet states by an energy gap of order J_i. At zeroth order in perturbation theory, the couplings to neighbouring spins are neglected, such that the total ground state factorizes into the ground state of this two-site problem and the as yet undefined states of the remaining spins. The zeroth-order ground state of the system is therefore

$$|\psi\rangle = |\psi_{j<i}\rangle \otimes |\psi_i^-\rangle \otimes |\psi_{j>i}\rangle, \tag{2.29}$$

where $|\psi_i^-\rangle = \frac{1}{\sqrt{2}}(|\uparrow\downarrow\rangle_{i,i+1} - |\downarrow\uparrow\rangle_{i,i+1})$ is the maximally entangled singlet ground state of the two-site XX model and $|\psi_{j<i}\rangle$, $|\psi_{j>i}\rangle$ refer to the state of the spins to the left and right of the singlet respectively. To compute higher order corrections to the ground state of our system we consider the spins i and $i+1$ to be 'frozen' into this singlet state. Perturbation theory is then employed to find the effect induced by quantum fluctuations on the neighbouring spins, as shown in [41]. It is found that an effective coupling arises between sites $i-1$ and $i+2$ of strength

$$\tilde{J}_{i-1,i+2} = \frac{J_{i-1}J_{i+1}}{J_i}. \tag{2.30}$$

In this way the coupling between sites i and $i+1$ is replaced by effective longer range interaction that captures the low-energy properties of the model. For a random coupling profile, successive iterations of this procedure yield a 'random singlet phase', as singlets form between the pairs of spins most strongly coupled after each decimation (see Figure 2.4(a)). In [41] Vitagliano, Riera and Latorre demonstrated how a coupling profile that decays exponentially away from the centre of the chain produces a special form of ground state known as the 'concentric singlet phase'. This ground state is also known as the 'rainbow state', due to its distinctive structure of a series of singlets symmetrically distributed around the centre of the chain as shown in Figure 2.4. For any given bipartition, the entanglement entropy is directly proportional to the number of singlets 'cut' by the bipartition. Thus, for such a coupling profile, the area law of entanglement entropy is maximally violated.

In the absence of transverse fields, the rainbow model emerges as a special case of our Hamiltonian $\mathcal{H}_{(N)}$, illustrating that even strictly local interactions can give rise to ground states with volume-law entanglement scaling [41]. Owing to this feature, it has been widely employed to investigate entanglement properties in both one- and higher-dimensional spin systems [43, 45, 47]. Building on this foundation, we show that within a real-space RG framework, the inclusion of transverse fields extends the construction by introducing additional tunable parameters associated with the quantum deformation

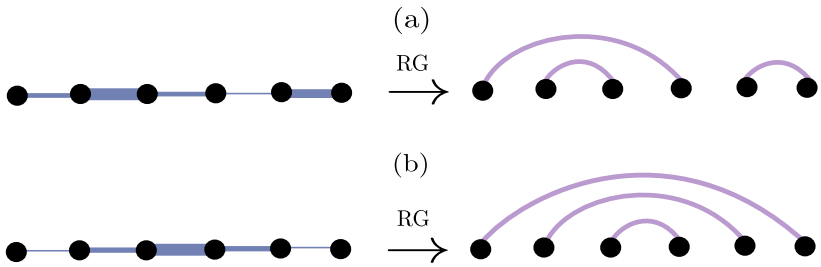

Figure 2.4: (a) For a random coupling, the inhomogeneous XX model yields a corresponding random singlet phase. (b) When the coupling strength decays exponentially away from the centre of the chain, the Real-Space Renormalization Group produces the 'rainbow' ground state.

q. This generalization grants control not only over the entanglement entropy but also over the full entanglement spectrum, thereby enabling precise and analytically tractable manipulation of bipartite correlation structures.

q-Deformed Rainbow Model Renormalization Group

We now apply the Real-Space RG approach to the generalised model defined in (2.27). In the limit $J_1, h_1 \gg J_2, h_2$, this yields the ground state

$$|\psi\rangle = |\psi_{i<-1}\rangle \otimes |\psi_1\rangle \otimes |\psi_{i>1}\rangle\,, \tag{2.31}$$

to zeroth-order in perturbation theory, where $|\psi_1\rangle$ is the q_1-deformed singlet as defined in equation (2.23). To compute corrections to the ground state at higher orders, second-order perturbation theory is used, as illustrated in Figure 2.5 (see also Appendix A.3). We derive an effective Hamiltonian of the form (2.20) acting between sites -2 and 2 with a renormalized coupling

$$\tilde{J}_2 = \frac{4J_2^2}{[2]_{q_1}^2 J_1}, \tag{2.32}$$

and transverse field terms

$$\tilde{h}_2 = h_2 - \frac{2\left(q_1 - \frac{1}{q_1}\right)J_2^2}{[2]_{q_1}^2 J_1}. \tag{2.33}$$

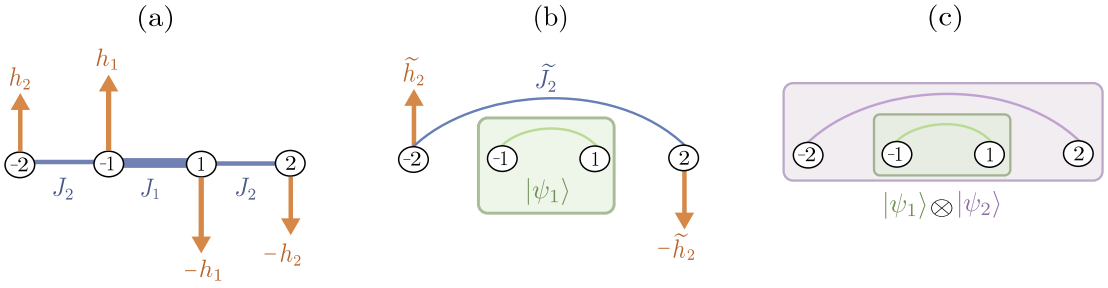

Figure 2.5: The Real-Space RG procedure. (a) $\mathcal{H}_{(2)}$ acting on a chain of four spins. For $J_1, h_1 \gg J_2, h_2$ perturbation theory yields a q-deformed singlet $|\psi_1\rangle$ between the central two spins. (b) These spins are integrated out and an effective Hamiltonian of the form (2.20) is found to act between sites -2 and 2 with renormalized coupling $\tilde{J}_2$ and transverse field $\tilde{h}_2$. (c) Diagonalization of this effective Hamiltonian yields the ground state $|\psi\rangle = |\psi_1\rangle \otimes |\psi_2\rangle$. The difference in colour of the bonds between the two pairs indicates the difference in correlations that can be achieved by appropriately tuning J_1, J_2, h_1 and h_2.

In the case that $\tilde{J}_2, \tilde{h}_2 \gg J_3, h_3$ this effective Hamiltonian can be diagonalised to yield an additional q_2-deformed singlet, $|\psi_2\rangle$, between sites -2 and 2, where $q_2 = e^{\gamma_2}$, $\sinh\gamma_2 = \frac{\tilde{h}_2}{\tilde{J}_2}$.

If the couplings throughout the chain are selected such that $\tilde{J}_i, \tilde{h}_i \gg J_{i+1}, h_{i+1}$, then repeated iterations of this renormalization process will eventually yield the overall ground state

$$|\psi\rangle = |\psi_1\rangle \otimes |\psi_2\rangle \otimes \cdots \otimes |\psi_N\rangle\,, \tag{2.34}$$

where

$$|\psi_i\rangle = \frac{1}{\sqrt{[2]_{q_i}}}\left(q_i^{-\frac{1}{2}}\,|{\uparrow\downarrow}\rangle_{-i,i} - q_i^{\frac{1}{2}}\,|{\downarrow\uparrow}\rangle_{-i,i}\right), \tag{2.35}$$

and for $i > 1$

$$q_i = e^{\gamma_i} \text{ with } \sinh\gamma_i = \frac{\tilde{h}_i}{\tilde{J}_i}. \tag{2.36}$$

The renormalized coupling and transverse field parameters for the effective Hamiltonian between spins $-i$ and i are given by the recursive expressions

$$\tilde{J}_i = \frac{4J_i^2}{[2]^2_{q_{i-1}}\tilde{J}_{i-1}}, \tag{2.37}$$

$$\tilde{h}_i = h_i - \frac{2\left(q_{i-1} - \frac{1}{q_{i-1}}\right) J_i^2}{[2]_{q_{i-1}}^2 \tilde{J}_{i-1}}. \tag{2.38}$$

From equations (2.37) and (2.38), we see that the expressions for $\tilde{J}_i$ and $\tilde{h}_i$ are dependent on all previous $\tilde{J}_{j<i}$, $\tilde{h}_{j<i}$. By fixing all previous $i-1$ values, it is always possible to vary the associated physical parameters J_i and h_i such as to achieve any $1 \leq q_i \leq \infty$. In this way, we will show that the deformation of each q-singlet can be individually tuned to achieve any degree of pairwise entanglement between a given pair of spins.

2.4 Entanglement Properties of the q-Deformed Rainbow

The state (2.34) has a tensor product form. Subsequently, the reduced density matrix across a central bipartition admits the tensor product decomposition

$$\rho_A = \rho_1 \otimes \rho_2 \otimes \cdots \otimes \rho_N, \tag{2.39}$$

where each ρ_i is diagonal, given by

$$\rho_i = \begin{pmatrix} \frac{1}{1+q_i^2} & 0 \\ 0 & \frac{q_i^2}{1+q_i^2} \end{pmatrix}. \tag{2.40}$$

This decomposition yields simple expressions for many of the entanglement properties of the q-deformed rainbow, as we will see in the following.

2.4.1 Rényi and von Neumann entropies

Using the reduced density matrix tensor product decomposition we derive the form of the Rényi entropy of order α of the ground state (2.34) across a central bipartition

$$S_A^{(\alpha)} = \frac{1}{1-\alpha} \sum_{i=1}^{N} \ln \frac{1+q_i^{2\alpha}}{(1+q_i^2)^\alpha}, \quad \alpha > 0, \alpha \neq 1. \tag{2.41}$$

In the limit $\alpha \to 1$ we obtain an expression for the von Neumann entropy of the ground state

$$S_A = -\sum_{i=1}^{N} \left[\ln\left(1+q_i^2\right) - \frac{q_i^2}{1+q_i^2} \ln q_i^2 \right]. \tag{2.42}$$

In Section 2.3.1 we found the von Neumann entropy, $S_{A,1}$, of a single pair of spins -1 and 1 as a function of the deformation parameter q_1, as given by (2.25). By extending this definition to that of the von Neumann entropy of the state $|\psi_i\rangle$ between spins $-i$ and i

$$S_{A,i} = \ln\left(1+q_i^2\right) - \frac{q_i^2}{1+q_i^2} \ln q_i^2, \tag{2.43}$$

it is clear that the total von Neumann entropy is a sum of the individual von Neumann entropies of each concentric pair of spins on the chain. This is also true for the Rényi entropy, and is a natural consequence of the tensor product form of the reduced density matrix. By independently varying each q_i, we can therefore achieve all degrees of entanglement in the allowed maximal range $0 \leq S_A \leq N \ln 2$.

2.4.2 Entanglement Spectrum

As discussed in Section 2.2.1, the Hamiltonian $\mathcal{H}_{(N)}$ permits an exact mapping to a free fermion model of the generalised form (2.13). As a result, Wick's theorem enables the construction of the corresponding bipartite entanglement spectrum from a set of single-particle entanglement energies as

$$E_j^f(\{\epsilon\}) = E_0 + \sum_{i=1}^{N} n_i(j)\epsilon_i, \tag{2.44}$$

where E_0 is a normalization constant and each $n_j = \{0, 1\}$ [95]. This simplification describes an exponential reduction in complexity, such that the 2^N-value entanglement spectrum for the central bipartition of $\mathcal{H}_{(N)}$ is completely described by just N single-particle energies.

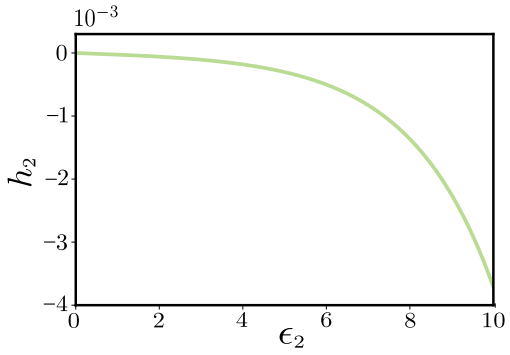

Figure 2.6: The values of h_2 required to generate any $0 \leq \epsilon_2 \leq 10$ for fixed $J_1 = h_1 = 1$, $J_2 = 0.01$ ($\epsilon_1 = -2\sinh^{-1}(1)$). Any desired value of ϵ_2 in this range can be obtained by selecting the corresponding value of h_2.

For our q-deformed rainbow, we find that

$$E_0 = \sum_{i=1}^{N} \ln(1 + q_i^2), \tag{2.45}$$

and

$$\epsilon_i = -\ln q_i^2. \tag{2.46}$$

Hence, the deformation parameters, q_i, of the q-deformed singlets directly determine the single-particle entanglement energies. As each q_i can take any value in the range $0 \leq q_i \leq \infty$, each ϵ_i can be individually tuned to take any value $-\infty \leq \epsilon_i \leq \infty$.

By combining (2.36) and (2.46) we derive the simple relationship

$$\gamma_i = -\frac{\epsilon_i}{2}. \tag{2.47}$$

This in turn yields an expression for the required ratio of the renormalized parameters for a given pair in order to produce a specific desired single-particle entanglement energy

$$\frac{\tilde{h}_i}{\tilde{J}_i} = -\sinh\left(\frac{\epsilon_i}{2}\right). \tag{2.48}$$

As a result, each single particle energy of the entanglement spectrum can be directly

obtained by appropriately tuning a single effective magnetic field. In Appendix A.4 we expand these expressions to derive closed forms for the required ratio of the physical coupling parameters. In Figure 2.6 the dependence of ϵ_2 on h_2 for a fixed set of example values $J_1 = h_1 = 1$ and $J_2 = 0.01$ is illustrated. For the shown range, any desired ϵ_2 can be simulated by simply reading off the corresponding value of h_2. In this way, by fixing all previous $i-1$ single-particle entanglement energies, ϵ_i can be tuned to any desired value by appropriately varying h_i.

2.5 Fidelity Optimisation

In the previous section we have demonstrated how controlled variation of the parameters of our model in the strong inhomogeneity limit $\tilde{J}_i, \tilde{h}_i \gg J_{i+1}, h_{i+1}$ allows for the generation of any arbitrary pattern of correlations given in terms of the entanglement entropy (2.42) or the single-particle entanglement energies (2.48). In this section we present how the parameters of our model can be chosen such that the fidelity is maximised for any desired entanglement profile. Here, we define the fidelity as a measure of the 'closeness' of two quantum states, $|\psi_A\rangle$ and $|\psi_B\rangle$, given by the squared overlap, $|\langle\psi_A|\psi_B\rangle|^2$ [34]. To optimise the choice of parameters for any desired correlation profile, we start by considering the variation of the fidelity between the exact ground state of our model and the q-deformed rainbow for the case $N = 2$. These results can then be used to inform the fidelity optimisation for larger spin chains.

2.5.1 Optimising h_2

In Section 2.3.1, we noted that a symmetry of our two-site Hamiltonian (2.20) results in the preservation of the von Neumann entropy, $S_{A,1}$, under the transformation $h_1 \to -h_1$. Here, we will show that although $S_{A,2}$ possesses a similar symmetry under the transformation $\tilde{h}_2 \to -\tilde{h}_2$, one of these values will yield a significantly higher fidelity than the other corresponding to the choice of sign of $\frac{h_1}{J_1}$.

In Figure 2.7 we plot the fidelity between the q-deformed rainbow (2.34) on four sites

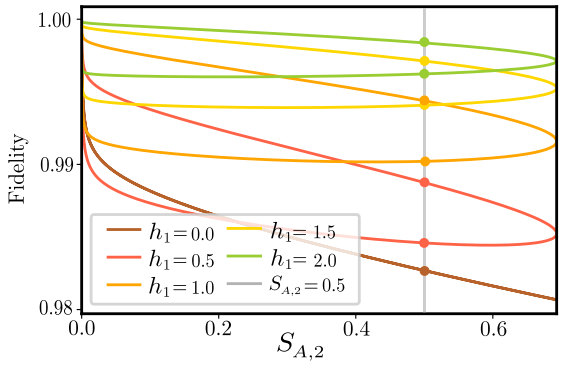

Figure 2.7: Variation of the ground state fidelity with the entanglement entropy of the outer pair for different fixed values of h_1 with $J_1 = 1$ and $J_2 = 0.1$. The grey line shows an example of a desired outer entanglement entropy, $S_{A,2} = 0.5$. The two intersections with each curve for $h_1 > 0$ indicate two possible values of h_2 to generate the desired $S_{A,2}$ with a distinct difference in fidelity. This choice can be used to optimise the accuracy of our model.

and the exact ground state of (2.27) as a function of the entanglement entropy between sites -2 and 2 for a range of constant values of h_1. For each curve J_1, h_1 and J_2 are fixed such that $S_{A,2}$ is a function of h_2. We see that for any desired value of $S_{A,2}$, for example $S_{A,2} = 0.5$ as indicated by the vertical grey line, the two intersections with each curve indicate two values of h_2 that correspond to the same degree of entanglement, but with a distinct difference in fidelity. As described these two solutions arise due to the natural symmetry of the entanglement entropy about $\tilde{h}_2 = 0$, for which the degree of entanglement between sites -2 and 2 is maximised. To find the physical transverse field value $h_2^{\max}$ that maximises $S_{A,2}$ we substitute $\tilde{h}_2 = 0$ into equation (2.33) to obtain

$$h_2^{\max} = \frac{2\left(q_1 - \frac{1}{q_1}\right) J_2^2}{[2]_{q_1}^2 J_1}. \tag{2.49}$$

The symmetry of the entanglement entropy $S_{A,2}$ about $h_2^{\max}$ is shown in Figure 2.8(a) for the case $J_1 = h_1 = 1$, $J_2 = 0.1$. By mapping these values onto the plot of fidelity with $S_{A,2}$ as shown in Figure 2.8(b), we see that we have a 'high fidelity branch' corresponding to $h_2 \geq h_2^{\max}$ ($\tilde{h}_2 \geq 0$) and a 'low fidelity branch' for $h_2 \leq h_2^{\max}$ ($\tilde{h}_2 \leq 0$). For any desired value of $S_{A,2}$, the fidelity is clearly maximised by choosing the appropriate value of

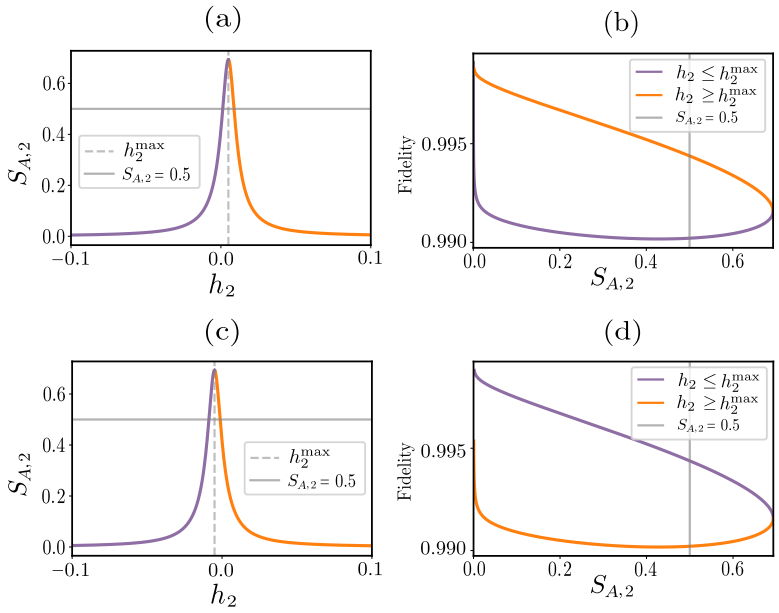

Figure 2.8: (a) For fixed $J_1 = h_1 = 1, J_2 = 0.1$, the variation of $S_{A,2}$ is symmetric about $h_2^{\max}$. (b) A given value of $S_{A,2}$ is achieved with higher fidelity with selection of h_2 from the branch $h_2 \geq h_2^{\max}$. (c) As h_1 changes sign this symmetry is retained, but as shown in (d) the higher fidelity branch now corresponds to $h_2 \leq h_2^{\max}$.

$h_2 \geq h_2^{\max}$. In contrast, if the sign of h_1 is reversed while J_1 remains fixed, as shown in Figures 2.8(c) and 2.8(d), the opposite is true, and the fidelity is maximised by selecting the value of h_2 from the branch $h_2 \leq h_2^{\max}$. In this way, for fixed couplings J_1 and J_2, the magnitude and direction of the applied magnetic field terms h_1 and h_2 can be selected such as to maximise the accuracy of our model.

2.5.2 Optimising Order of Pairs

Our system has a symmetry with respect to which pair of spins i and $-i$ is used to tune a certain single particle entanglement energy ϵ_k. We can use this freedom, in conjunction with the optimisation procedure of the previous subsection, to optimise the overall fidelity of our chain simulator.

Consider the case in which we want to use our model to generate a given pair of two-site von Neumann enanglement entropies, for example, $S_{A,i} = 0.2$ and $S_{A,j} = 0.6$. Our simulator has the freedom in the choice $i = 1, j = 2$ or $i = 2, j = 1$. In Figure 2.9

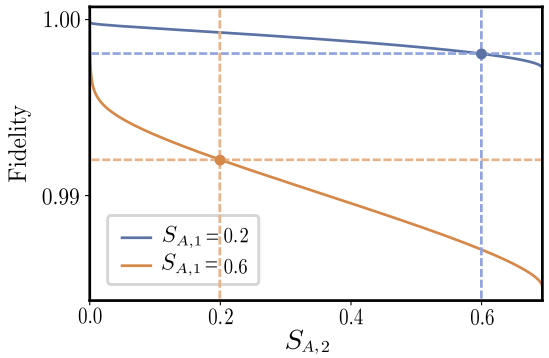

Figure 2.9: Fidelity as a function of $S_{A,2}$ with fixed $S_{A,1} = 0.2$ and 0.6. Dashed lines indicate the higher fidelity achieved when the ordering $S_{A,1} = 0.2, S_{A,6} = 0.6$ is imposed.

we plot the two curves corresponding to $S_{A,1} = 0.2$, and $S_{A,1} = 0.6$ for $J_1 = 1$, $J_2 = 0.1$ and h_1 tuned accordingly. The analysis of the previous subsection has been applied to restrict to the appropriate high fidelity branch $h_2 \geq h_2^{\max}$. From Figure 2.9 we observe that our model can be used to achieve $S_{A,1} = 0.2, S_{A,2} = 0.6$ with a significantly higher fidelity than $S_{A,1} = 0.6, S_{A,2} = 0.2$. The importance of the ordering of the degrees of entanglement is further illustrated in Figure 2.10 with a direct comparison of the fidelity with the degree of entanglement between one pair when the other is maximally entangled. For all values of $S_{A,i}$, it is observed that the fidelity is maximised when the maximally entangled state lies between sites -2 and 2.

In Appendix A.5 an exact relationship between our chosen parameters and the fidelity is given for the case $N = 2$. For any desired set of single-particle energies ϵ_i, ϵ_j or entropies $S_{A,i}, S_{A,j}$ the corresponding field and coupling terms can be substituted into equation (A.40) in order to directly determine the ordering that will optimise the fidelity.

2.5.3 Fidelity Analysis for Larger Chains

In the previous two subsections we have shown that appropriate choices of the values of the transverse field parameters, and ordering of the degree of entanglement allow us to optimise the fidelity and thereby the accuracy of our model for the case $N = 2$. Although the simplest non-trivial implementation of our model, these techniques derived for the

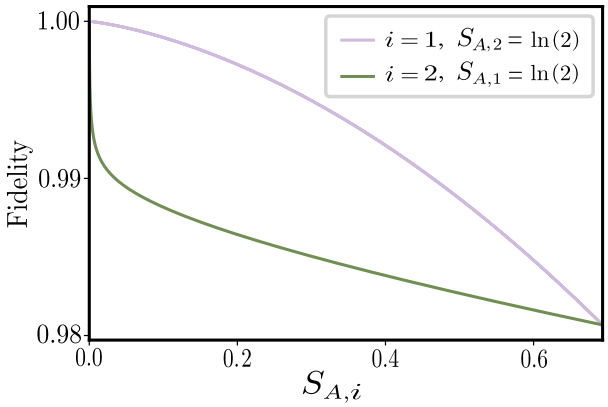

Figure 2.10: Fidelity between the four-site q-deformed rainbow and the exact ground state for one maximally entangled pair and a second pair with varying entanglement entropy. Fidelity is shown to be maximised when the maximally entangled pair is between sites -2 and 2.

four-spin chain can also be used to optimise the fidelity of our simulator on larger chains. For example, in Section 2.6.2 we will introduce an example of a non-uniform spectrum that our model can simulate known as the 'prime number spectrum', in which the single-particle entanglement energies for a chain with N pairs are the logarithms of the first N prime numbers. Performing a numerical optimisation procedure for this spectrum on 10 sites with a coupling profile of the form $J_i = 10^{-\frac{i(i-1)}{2}}$ we find that the fidelity is maximised when $\{\epsilon\} = \{\ln 3, \ln 11, \ln 7, \ln 5, \ln 2\}$. Choosing our coupling and transverse field terms such as to produce the single-particle energies in this order ensures that the ground state of (2.27) matches our q-deformed ground state with a fidelity > 0.988. To highlight the importance of this choice we note that in contrast, using our simulator to produce the same spectrum with alternate ordering $\{\epsilon\} = \{\ln 11, \ln 2, \ln 3, \ln 5, \ln 7\}$, yields a fidelity of only 0.878 to three decimal places.

Thus, our analysis for the case $N = 2$ also aids in the application of our simulator to larger chains. For larger chains however, there are additional features that we must discuss. We start by noting that, although our model is theoretically exact up to the thermodynamic limit, in practice, the balance between the rapid decay of our coupling and transverse field parameters ensuring the validity of our real-space RG approach and

the finite precision of computational methods, only allows us to numerically simulate small system sizes. Such restrictions were discussed in the original work on the rainbow state model [41]. To perform error analysis on the system for larger chains we must therefore choose a coupling profile and single-particle entanglement energy spectrum known to yield a high fidelity. Here we will consider the effect of random errors on the simulation of the optimised prime number spectrum on 8 sites, $\{\epsilon\} = \{\ln 3, \ln 7, \ln 5, \ln 2\}$ for the coupling profile $J_i = 10^{-\frac{i(i-1)}{2}}$. This spectrum can be achieved with a fidelity > 0.983. For some fixed Δ we generate a profile of random errors $\{\delta_i\} \in [-\Delta, \Delta]$, such that our parameters $J_i \to J_i + \delta_i$ and $h_i \to h_i + \delta_i$. For these altered parameters, equations (2.37), (2.38), (2.46) and (2.48) can be used to find the new entanglement spectrum and q-deformation parameters. These values can then be used to find a modified form of the q-deformed rainbow ground state. By taking the overlap between this state and the q-deformed rainbow for our desired entanglement profile we calculate a value for the fidelity. For each Δ this process is repeated 10,000 times and an average value for the fidelity calculated. The results for a selected range of Δ are shown in Figure 2.11. We observe that as mentioned above, this drop in fidelity with the increasing size in error is related to the size of the weakest parameters in our model. As the size of the couplings and transverse fields increase from left to right we observe a drop in the fidelity each time the size of the error exceeds the magnitude of one of these parameters. Naturally, as our parameters become smaller with an increasing number of sites on our chain, the accuracy of our model becomes increasingly sensitive to errors.

2.6 Special Cases

We have shown how the tuning of the parameters of our model allows for the generation of any arbitrary set of single-particle entanglement energies. In this section we highlight two interesting applications: the case in which all deformation parameters are equal, and the reproduction of the single-particle entanglement energies for the 'prime number spectrum' introduced below.

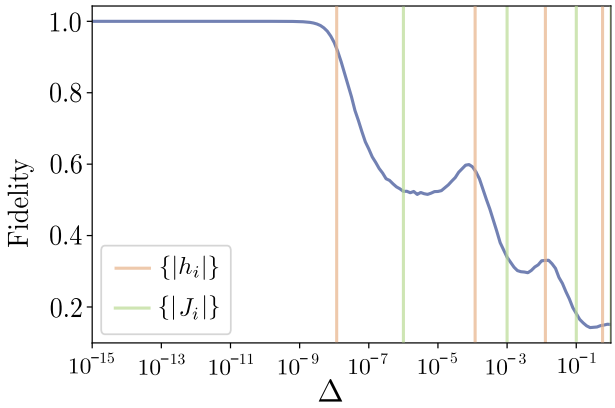

Figure 2.11: Simulation fidelity for $\{\epsilon\} = \{\ln 3, \ln 7, \ln 5, \ln 2\}$ for the coupling profile $J_i = 10^{-\frac{i(i-1)}{2}}$ in the presence of errors $\delta_i \in [-\Delta, \Delta]$ calculated over 10,000 randomised profiles. We observe that the fidelity remains high until Δ becomes of the order of the weakest parameter h_4. Additional significant drops in fidelity occur each time the size of the error exceeds the magnitude of one of these parameters.

2.6.1 The $q_1 = q_2 = \cdots = q_N = q$ Case

In the rainbow state model, the ground state is a tensor product of concentric maximally entangled singlets, or in the language of our model, $q_i = 1$, for all i. Here, we show how the parameters of our model can be chosen such that all deformation parameters take the same value, $q_i = q$, for some chosen q in the allowed range $0 < q < \infty$. In this way, each concentric pair on our chain shares the same degree of pairwise entanglement, and all single-particle entanglement energies are equal.

We have defined $q_1 = e^{\sinh^{-1}\left(\frac{h_1}{J_1}\right)}$ and $q_{i>1} = e^{\sinh^{-1}\left(\frac{\tilde{h}_i}{\tilde{J}_i}\right)}$, such that the condition $q_1 = q_i \implies \frac{h_1}{J_1} = \frac{\tilde{h}_i}{\tilde{J}_i}$. Re-arranging equation (2.23) and setting $q_1 = q$ yields

$$\frac{h_1}{J_1} = \frac{1}{2}\left(q - \frac{1}{q}\right), \tag{2.50}$$

for some desired $q > 0$.

For all other pairs of sites the relations for the renormalised couplings must be used. For example, by dividing equation (2.33) by equation (2.32) and equating with (2.50) we

obtain

$$h_2 = \frac{2J_2^2}{h_1}\frac{\left(1-q^2\right)^2}{\left(1+q^2\right)^2}. \tag{2.51}$$

For any fixed value of J_2 this relation can be easily implemented to find the required transverse field parameter to produce some desired $q > 0$.

In the same way, the ratio of equations (2.37) and (2.38) can be equated with (2.50) in order to obtain the general formula

$$h_i = \frac{4J_i^2}{h_{i-1}}\frac{\left(1-q^2\right)^2}{\left(1+q^2\right)^2}, \quad i > 2. \tag{2.52}$$

By iterating through and systematically determining each successive value of the required transverse field for some fixed coupling profile, these relations allow us to produce a one-dimensional chain in which each concentric pair shares the same degree of pairwise entanglement.

In Figure 2.12 the variation of the fidelity with system size is plotted for a range of values of q. For each fixed number of sites on the chain, the fidelity increases with the value of q, corresponding to a better simulation of chains with a lower degree of entanglement between the pairs. The case with lowest fidelity corresponds to the reproduction of the rainbow state with $q = 1$ such that $h_i = 0$ for all i. For each fixed value of q, as the number of sites on the chain increases the fidelity drops off, rapidly for the increase from 2 to 3 pairs, then more slowly up to 5 pairs.

2.6.2 Prime Number Spectrum

Prime numbers play an important role in number theory. The Fundamental Theorem of Arithmetic [96] states that every natural number greater than one can be uniquely factorised as a product of prime numbers

$$N = 2^{n_2}3^{n_3}\ldots p^{n_p}\ldots, \tag{2.53}$$

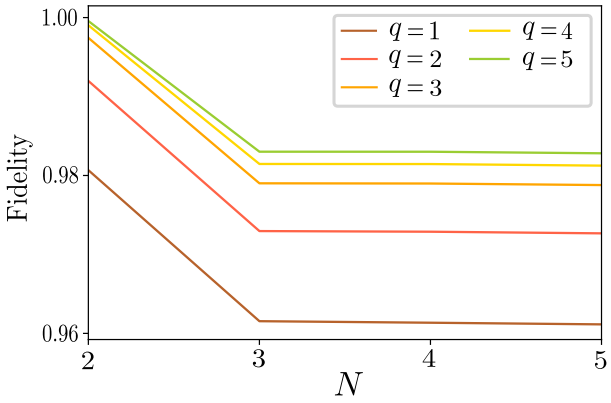

Figure 2.12: Variation of the fidelity with system size for the case of homogeneous entanglement $q_1 = \cdots = q_N = q$.

where p is a prime and n_p counts the number of times that p appears in the factorisation of N. In this way, prime numbers can be thought of as the building blocks of all natural numbers.

Let us introduce the Möbius function, $\mu(n)$:

$$\mu(n) = \begin{cases} 1, & n = 1, \\ (-1)^r, & n = p_1 \dots p_r, \\ 0, & \exists p, p^2 | n, \end{cases} \tag{2.54}$$

where p are prime numbers. The symbol $p^2|n$ means that p^2 divides n. A square free integer is an integer whose factorization into products of primes does not contain any square of a prime numbers. $\mu(n)$ is therefore non-vanishing only on square free integers with value $+1$ if it contains an even number of primes and -1 if it contains an odd number of primes.

In number theory, the Möbius function plays a central role in multiplicative arithmetic and in the inversion of divisor sums. Most notably, it appears in the Möbius inversion formula, which allows arithmetic functions to be uniquely recovered from their cumulative sums over divisors. In this sense, $\mu(n)$ acts as an inclusion–exclusion weight that removes overcounting arising from shared prime factors. The Möbius function also

features prominently in analytic number theory, where it is closely connected to the distribution of prime numbers through identities involving the Riemann zeta function, such as

$$\frac{1}{\zeta(s)} = \sum_{n=1}^{\infty} \frac{\mu(n)}{n_s}, \tag{2.55}$$

From this perspective, $\mu(n)$ encodes cancellations between contributions from different prime factorizations.

These properties motivate an analogy with Fermi statistics, in which primes are interpreted as fermionic degrees of freedom subject to an exclusion principle. The vanishing of $\mu(n)$ for integers divisible by higher powers of primes mirrors the prohibition of multiple occupancy, while the alternating sign $(-1)^r$ reflects the parity of the number of occupied modes [97].

Let us now consider an entanglement spectrum of the form

$$\lambda_k = \frac{A_F \mu(k)}{k^s}, \;\; A_F, s > 0, \; k = 1, \ldots, \infty. \tag{2.56}$$

The normalization of the eigenvalues implies that

$$1 = \sum_{k=1}^{\infty} \lambda_k = A_F \prod_p (1 + p^{-s}) = A_F \frac{\zeta(s)}{\zeta(2s)}, \tag{2.57}$$

where we have used the Euler product formula

$$\zeta(s) = \prod_p \frac{1}{1 - p^{-s}}, \;\; \mathrm{Re}(s) > 1. \tag{2.58}$$

Using equation (2.9), the entanglement energies for this spectrum are given by

$$E_k = -\ln \lambda_k = -\ln A_F + s \ln k. \tag{2.59}$$

Where k is any square free integer. We equate this expression with that of the spectrum

of a free fermionic system

$$-\ln A_F + s\ln k = E_0 + \sum_{i=1}^{N} n_i(k)\epsilon_i. \tag{2.60}$$

If k is a square free integer then from the Fundamental Theorem of Arithmetic one has

$$k = 2^{n_2}3^{n_3}\ldots p^{n_p}\ldots, \quad n_i = 0, 1, \tag{2.61}$$

such that taking the logarithm of (2.61) yields

$$\ln k = \sum_{p:prime} n_p \ln p, \quad n_p = 0, 1. \tag{2.62}$$

Hence, equation (2.60) is solved by

$$E_0 = -\ln A_F = \frac{\zeta(s)}{\zeta(2s)}, \tag{2.63}$$

$$\epsilon_p = s\ln p. \tag{2.64}$$

The parameter s can be thought of as an entanglement temperature since it is common to all eigenenergies. The relation (2.64) has also been considered in [98, 97] with $\ln p$ being the single-particle energies of the primon gas. The partition function of this gas is related to the Riemann zeta function, $\zeta(s)$. In recent work, a prime number eigenvalue spectrum has also been experimentally realised by application of holographic optical traps [99], in agreement with previous theoretical results [100].

This example spectrum (2.64), motivated by the interesting parallel between the decomposition of integers in terms of prime numbers and the decomposition of free-system entanglement spectra in terms of single-particle energies, provides an example of a non-uniform entanglement spectrum that can be reproduced using our q-deformed model. To implement this spectrum for some finite number of pairs with fixed coupling profile $\{J_i\}$, the required values of the set $\{h_i\}$, can simply be read off from equations

(A.29), (A.30) and (A.31) in Appendix A.4.

2.7 Conclusions

In summary, the one-dimensional spin-chain model presented here exhibits complete controllability over the free-particle entanglement in a bipartite system. As illustrated through two representative cases, this controllability enables the high-fidelity simulation of arbitrary free-fermion correlations, providing an invaluable tool for quantum technologies whenever specific patterns of quantum correlations are required [51, 52, 101]. Our scheme is a generalisation of the rainbow states of concentric maximally entangled singlets to the case of concentric pairs, each one with variable entanglement parametrised by a single deformation parameter q. The entanglement over a set of N pairs is easily tuned with the appropriate choice of only N independent transverse field terms. Moreover, the construction of this universal simulator in terms of simple local coupling and field terms only, enables direct accessibility for implementation across a range of experimental platforms. Rydberg atom arrays for example, provide a powerful platform for the precise control over local spin-$\frac{1}{2}$ interactions, providing a direct path for the simulation of this quantum spin system [102, 103, 104].

The q-deformed rainbow ground state of our model was obtained through a Real-Space Renormalization Group approach. To test the validity and applicability of our method we compared the fidelity of the predicted theoretical model with the exact diagonalisation of the spin system. The employed perturbation method has a symmetry in terms of the ordering of the concentric entangled states. By taking advantage of this symmetry we find the optimal order of magnetic fields that gives the best fidelities. Finally, we apply our method to two case scenarios. First, we consider the homogeneous case of concentric pairs with the same entanglement. Second, we consider the case of single particle energies of the entanglement spectra that are parametrised by the logarithms of the prime numbers as derived by Germań Sierra. This model is inspired by the similarity between the decomposition of free-system entanglement spectra in terms of single particle

energies and the decomposition of integers in terms of prime numbers. In recent experimental work, holographic techniques have been developed allowing for the tuning of the energy spectrum of the single-particle Schrödinger equation [99]. Notably a 'prime number quantum potential', $V_N(x)$, can be applied such that the single-particle Schrödinger equation has the lowest N prime numbers as eigenvalues. These techniques demonstrate an interesting procedure for the reproduction of arbitrary sequences of integers as energy spectra with possible applicability to this work.

In the absence of transverse fields, our model reduces to the maximally entangled rainbow ground state [41], a simple one-dimensional system that has been utilised in quantifying the limits of entanglement distribution [47], state engineering [45], and quantum channel performance [44]. Extensions to higher dimensions and quenched dynamics have further established the rainbow chain as an invaluable platform for studying entanglement spreading and non-equilibrium physics in inhomogeneous chains [43, 47, 105, 106]. Building on this foundation, our universal simulator combines the inhomogeneous coupling structure with a quantum-group-inspired q-deformation, enriching the original construction with an additional tunable degree of freedom while retaining exact analytical control. This deformation opens new avenues for extending the physics of rainbow states. For instance, Samos Sáenz de Buruaga et al. [107, 108] demonstrated that folding the inhomogeneous rainbow spin-1/2 chain about its centre yields effective one-dimensional models with symmetry-protected topological order. Applying a similar folding strategy to the q-deformed rainbow chain thus suggests the possibility of realizing a topological phase with characteristics precisely controlled by the deformation parameter q.

Chapter 3

Anyons and the Quantum Double Model

3.1 Introduction

Having concluded our investigation of quantum correlations in one-dimensional systems, we now take the step up to two dimensions. Here, exotic particles can appear with exchange statistics interpolating between those of bosons and fermions. These particles fall into two categories: Abelian anyons whose exchange may yield any arbitrary phase factor, and the more remarkable non-Abelian anyons, the braiding of which may enact unitary operations on the combined wavefunction. Although direct experimental observation of these particles is a highly non-trivial task, lattice models have been developed that allow for the simulation of quantum systems that give rise to certain properties of anyons [109, 110, 111, 112, 113]. Among lattice models that host non-Abelian anyons, Kitaev's quantum double construction [22] has emerged as a powerful tool, providing an exactly solvable framework where anyonic excitations arise from the algebra of a finite group $\mathbf{G}$.

In this chapter we provide a brief overview of the background material for anyonic models as will be relevant in the following two chapters. We start by defining the basic

components required to describe a given model, including the R and F matrices that form the description of all anyonic braiding operations. In Section 3.3 we will then present the construction of Kitaev's quantum double model, in which these anyons appear as localised excitations on a lattice of spins.

3.2 Components of an Anyonic Model

Formally, an anyonic model is a mathematical structure that characterizes the fusion and braiding properties of quasiparticle excitations in a topologically ordered system. The definition of such a model may be broken down into several key components. Firstly, a given model necessarily consists of a finite set of particle types (anyon species), always including the trivial vacuum particle $\mathbf{1}$. Anyonic models must be closed under fusion, a process whereby pairs of anyons come together to form composite anyons as represented in terms of anyonic worldlines in Figure 3.1(a). In general, for non-Abelian anyons, this outcome is not unique and the fusion of two non-Abelian anyons may produce multiple distinct composite anyons. Mathematically we represent the possible fusion outcomes or 'channels' of anyons a and b as

$$a \times b = \sum_c N_{a,b}^c c. \tag{3.1}$$

The fusion co-efficients $N_{a,b}^c$ are non-negative integers indicating the total number of ways that anyons a and b may fuse to a given anyon c. $N_{a,b}^c = 0$ means that there is no way that anyons a and b can fuse to c while $N_{\mathbf{1}}^{ab} > 0$ indicates that a is the antiparticle of b and vice versa.

For the pairwise fusion of non-Abelian anyons $a \times b = c + d + \ldots$ one may define a multi-dimensional anyonic basis indexed by these possible fusion outcomes $\{|a, b \to i\rangle\}$, with $i = c, d, \ldots$. In general, the set of all possible ways that a collection of anyons can fuse to a given outcome is known as the fusion space of the anyons. The states spanning this basis are labelled by the different intermediate outcomes and the dimension of the fusion space

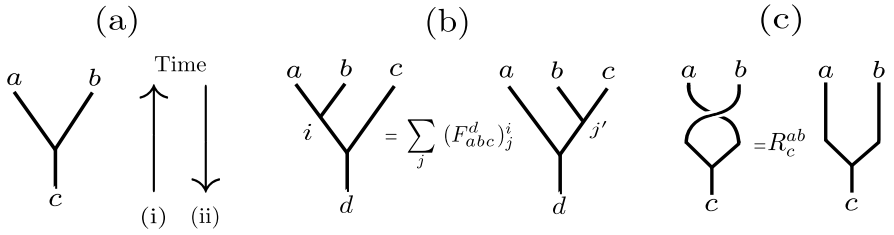

Figure 3.1: Fundamental anyonic processes. (a) Pairwise (i) creation and (ii) fusion. (b) The basis transformation described by the F matrix. (c) The phase induced by anti-clockwise braiding of anyons with fixed fusion channel.

corresponds to the multiplicity of the fusion outcome. Notably, the fusion space is a non-local degree of freedom: it cannot be accessed or manipulated through local operations or classical communication (LOCC) on individual anyons. The encoding of logical states within this fusion space, therefore provides a means of encoding quantum information non-locally such that it is intrinsically protected from local environmental perturbations. The controlled manipulation of the fusion space, and therefore the encoded quantum information, is achieved using non-local topological operations such as anyonic braiding and fusion [114].

Consider now the fusion of three anyons a, b, c to some fixed outcome d. Anyonic fusion is a pairwise process, such that in order to uniquely define a fusion basis for this process, one must assign an order in which the fusion processes occur. The associated Hilbert space may be indexed by the possible intermediate fusion outcomes $a \times b \to i$ such that $i \times c \to d$ as shown on the left-hand side of Figure 3.1(b). Each state in this Hilbert space compactly takes the form $|(a, b), c \to i, c \to d\rangle$. Fusion associativity $(a \times b) \times c = a \times (b \times c)$ however dictates that this same Hilbert space can equivalently be spanned by the states as represented on the right-hand side of Figure 3.1(b), for intermediary composite anyons j. Mapping between these two representations therefore requires the description of a basis transformation known as the fusion matrix F^d_{abc}. The action of this mapping may be described in the anyonic basis as

$$|(a, b), c \to i, c \to d\rangle = \sum_j (F^d_{abc})^i_j \, |a, (b, c) \to a, j \to d\rangle \, . \tag{3.2}$$

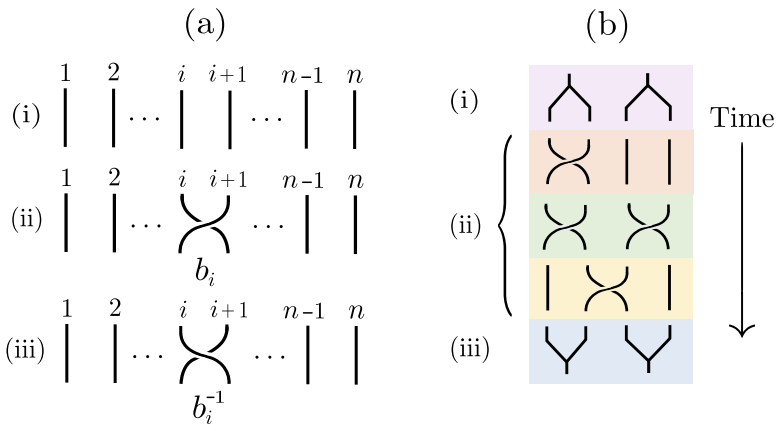

Figure 3.2: (a)(i) The n-strand braid group $\mathcal{B}_n$. (ii) The braid generator b_i exchanges strands i and $i+1$ in a clockwise manner, while in (iii) the inverse operation b_i^{-1} exchanges the strands in an anti-clock-wise manner. (b) A simple illustration of the core components of topological quantum computation. (i) *State initialization*: anyons are created in pairs from the vacuum. (ii) *Computation*: unitary operations are enacted via the braiding of non-Abelian anyons. (iii) *Measurement*: Fusion of anyons provides a measurement on the result of the computation process.

For non-Abelian anyons a, b, c, F^d_{abc} is in general a multi-dimensional unitary matrix.

The final ingredient in defining an anyonic model is some description of the braiding of pairs of anyons. Consider the fusion of two anyons a and b to fixed outcome c. If these two anyons undergo a counter-clockwise exchange before fusing, fusion commutativity $a \times b = b \times a$ dictates that their total charge c remains unchanged. Assigning a distinct basis state to each configuration, the swapping of two particles on a line therefore induces an isomorphism between these states described by the braiding operator

$$R_{\circlearrowleft} \left| a, b \to c \right\rangle = R^{ab}_c \left| b, a \to c \right\rangle , \tag{3.3}$$

where $R_{\circlearrowleft}$ corresponds to the anti-clockwise exchange of a and b anyons, as shown in Figure 3.1(c). For fusion processes with a unique fusion channel this mapping corresponds to the possible acquisition of a simple phase factor, R^{ab}_c. For the non-Abelian fusion of two X anyons, the fusion multiplicity generates a diagonal unitary matrix R^{XX} with entries $(R^{XX})^i_i \equiv R^{XX}_i$.

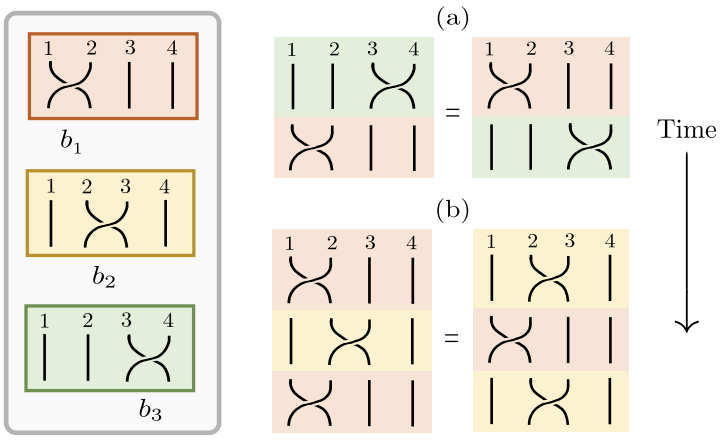

Figure 3.3: The three generators b_1, b_2 and b_3 of $\mathcal{B}_4$ obey the Yang-Baxter equations (a) $b_1 b_3 = b_3 b_1$ and (b) $b_1 b_2 b_1 = b_2 b_1 b_2$.

The F and R matrices encode the associativity and braiding properties of anyons, respectively. In the framework of topological quantum computation, quantum gates are realised through the braiding of anyonic worldlines, inducing unitary transformations on the multi-dimensional fusion space of non-Abelian anyons. Consider the worldlines of n anyons, as shown in Figure 3.2. The topologically distinct paths of n anyons in space-time form the n-strand braid group $\mathcal{B}_n$. The generators of this group may be represented as b_i, $(i = 1, \ldots, n-1)$, where b_i acts to exchange the strands i and $i+1$ in an anti-clockwise manner as shown in Figure 3.2(a). These generators obey the defining relations known as the Yang-Baxter equations

$$b_i b_{i+1} b_i = b_{i+1} b_i b_{i+1}, \qquad 1 \leq i \leq n-2 \tag{3.4}$$

$$b_i b_j = b_j b_i \quad \text{for } |i-j| > 1, \quad 1 \leq i, j \leq n-1, \tag{3.5}$$

represented graphically in Figure 3.3 [115, 116]. According to the formalism of modular tensor categories, the full representation of braid group actions—and hence the quantum gate set—is specified by the fusion rules and the corresponding F and R matrices of the anyon model [117]. It is important to note that the F and R matrices of a given model cannot be chosen arbitrarily, but must satisfy a set of consistency relations known as the

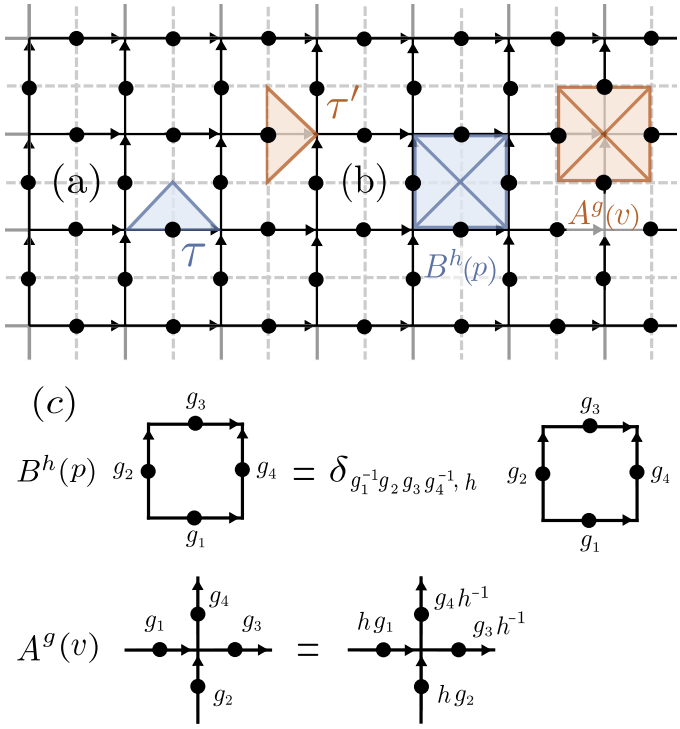

Figure 3.4: The lattice construction of the quantum double model $\mathbf{D}(\mathbf{G})$. The solid (dotted) lines denote the direct (dual) lattice with underlying orientation as indicated by arrows. $d = |\mathbf{G}|$-dimensional qudits are positioned on each link of the direct lattice. (a) Direct and dual triangles τ and τ' form the basis for single qudit operators $L^g_\pm$ and $T^h_\pm$ respectively. (b) Closed loops of these direct (dual) triangles construct the plaquette (vertex) projection components $B^h(p)$ ($A^g(v)$). (c) Action of the plaquette operator $B^h(p)$ (top) and vertex operator $A^g(v)$ (bottom) on the group elements composing the respective plaquette or vertex.

pentagon and hexagon relations [114]. By selecting solutions to these equations that are compatible with a given set of fusion rules, one therefore obtains a complete description of the topological behaviour of an anyonic model.

3.3 Kitaev's Quantum Double model

In the previous section, we have provided an abstract overview of the defining features of anyonic models. We now present the quantum double model $\mathbf{D}(\mathbf{G})$, as first introduced by Kitaev in 2003 [22]. This exactly solvable lattice model is constructed using the Drinfeld quantum double of a finite group $\mathbf{G}$, where the choice of $\mathbf{G}$ uniquely determines the

anyonic content of the model and their associated fusion and braiding statistics. Within this framework, anyons emerge as localized, coherent excitations on the lattice, each characterized by a distinct electric charge and magnetic flux component, in one-to-one correspondence with the irreducible representations of $\mathbf{D}(\mathbf{G})$ [118, 119].

Let $\mathbf{G}$ be any finite group with cardinality $|\mathbf{G}|$. The quantum double model $\mathbf{D}(\mathbf{G})$ may then be defined on any oriented two-dimensional lattice. For the purposes of this thesis we thus choose to consider a two-dimensional square lattice with orientation convention as shown in Figure 4.4. On each link of the lattice, a $d = |\mathbf{G}|$-dimensional Hilbert space or 'qudit' is positioned with orthonormal basis indexed by $\{|g\rangle : g \in \mathbf{G}\}$. Four linear operators are introduced with action

$$L_+^g |z\rangle = |gz\rangle\,, \qquad T_+^h |z\rangle = \delta_{h,z} |z\rangle\,, \tag{3.6}$$

$$L_-^g |z\rangle = |zg^{-1}\rangle\,, \qquad T_-^h |z\rangle = \delta_{h^{-1},z} |z\rangle\,. \tag{3.7}$$

for some $z, g, h \in \mathbf{G}$, on any $|\mathbf{G}|$-dimensional qudit. These operators $L_\pm^g$ and $T_\pm^h$ may be represented by dual and direct triangles respectively, as shown in Figure 4.4(a). Using this notation, we may define a local gauge transformation $A^g(v)$ as a closed loop of $L_\pm^g$ triangles around a given vertex v

$$A^g(v) = L_\pm^g \otimes L_\pm^g \otimes L_\pm^g \otimes L_\pm^g, \tag{3.8}$$

where the following orientation convention is applied

$$L^g = \begin{cases} L_+^g & \text{if the oriented edge points into the vertex,} \\ L_-^g & \text{if the oriented edge points out of the vertex.} \end{cases} \tag{3.9}$$

Similarly, we introduce the magnetic charge operator

$$B^h(p) = \sum_{h_1 h_2 h_3 h_4 = h} T_\pm^{h_1} \otimes T_\pm^{h_2} \otimes T_\pm^{h_3} \otimes T_\pm^{h_4}, \tag{3.10}$$

composed of direct triangles covering a plaquette p (see Figure 4.4(b)), obeying the labelling convention

$$T^h = \begin{cases} T^h_+ & \text{if the oriented edge is clockwise w.r.t the plaquette,} \\ T^h_- & \text{if the oriented edge is anti-clockwise w.r.t the plaquette.} \end{cases} \tag{3.11}$$

The above operators generate an algebra $\mathcal{D} = \mathbf{D}(\mathbf{G})$, which is the Drinfeld's quantum double of the group algebra $\mathbb{C}[\mathbf{G}]$ [120]. In order to illustrate how these loop operators relate to the measurement of charge and flux within the quantum double model we start by considering the action of $B^h(p)$ as shown in Fig. 4.4(c). When acting on a plaquette p, the operator $B^h(p)$ projects onto the subspace of states satisfying the constraint $g_1 g_2^{-1} g_3^{-1} g_4 = h$, where the group elements g_i label the edges surrounding the plaquette. In the language of lattice gauge theory, the product $h_p = g_1 g_2^{-1} g_3^{-1} g_4$ represents the holonomy, or equivalently the gauge-field 'twist', through the plaquette p. When $h_p = e$, with e denoting the identity element of $\mathbf{G}$, the gauge field is said to be flat across the plaquette and no magnetic flux is present. In this way, we define the projector onto the trivial flux sub-space for a plaquette p as

$$B(p) \equiv B^e(p) = \sum_{h_3 h_4 h_5 h_6 = e} T^{h_3}_\pm \otimes T^{h_4}_\pm \otimes T^{h_5}_\pm \otimes T^{h_6}_\pm. \tag{3.12}$$

A complementary construction arises from the vertex operators $A^g(v)$, which act on the four qudits adjacent to a vertex v as shown in Fig. 4.4(c). Each operator $A^g(v)$ implements a local gauge transformation by multiplying the surrounding edge variables by the group element g (or its inverse g^{-1}, depending on edge orientation). Taking the uniform average over all group elements,

$$A(v) = \frac{1}{|\mathbf{G}|} \sum_{g \in \mathbf{G}} A^g(v), \tag{3.13}$$

thus yields a projector onto the gauge-invariant subspace at vertex v. States in this

subspace carry no net electric charge, ensuring the absence of vertex excitations.

Consider now the construction of a Hamiltonian which energetically enforces these local gauge and flatness constraints encoded by the vertex and plaquette operators. For a lattice with vertices $v \in V$ and plaquettes $p \in P$, the Kitaev Hamiltonian of the quantum double model $\mathbf{D}(\mathbf{G})$ is given by

$$\mathcal{H} = -\sum_{v \in V} A(v) - \sum_{p \in P} B(p), \tag{3.14}$$

where $A(v)$ and $B(p)$ are the projectors defined in Eqs. (3.13) and (3.12), respectively. Notably, the orientation conventions (3.9) and (3.11) ensure that all such vertex and plaquette operators commute with one another

$$\big[A(v), A(v')\big] = 0, \quad \big[B(p), B(p')\big] = 0, \quad [A(v), B(p)] = 0, \tag{3.15}$$

for all vertices v, v' and plaquettes p, p' (see Appendix B.2). This mutual commutativity implies that the Hamiltonian is exactly solvable with eigenstates that can be chosen to be simultaneous eigenstates of all $A(v)$ and $B(p)$. Defined on a lattice with open boundaries, one thus obtains a unique ground state $|\zeta\rangle$, corresponding to the anyonic vacuum, in which

$$A(v)\,|\zeta\rangle = |\zeta\rangle\,, \;\; B(p)\,|\zeta\rangle = |\zeta\rangle\,, \tag{3.16}$$

for all vertices, v, and plaquettes, p. Excitations of this model are particle-like and are indicated by violations of the conditions (3.16). A vertex, v, for which $A(v)\,|\zeta\rangle \neq |\zeta\rangle$ indicates the presence of an electric charge excitation or 'chargeon', while $B(p)\,|\zeta\rangle \neq |\zeta\rangle$ signals the presence of a magnetic flux excitation or 'fluxon' on the plaquette p. This model also admits the description of dyons− composite particles with both non-trivial flux and charge defined on a neighbouring vertex and plaquette.

Before introducing the ribbon operators that may be used to coherently create and manipulate anyons as quasiparticle excitations of this lattice model, we first review the

formalism for the classification of such anyonic excitations in the quantum double model.

3.3.1 Anyons in the Quantum Double Model

In the previous section, the Kitaev Hamiltonian (3.14) was introduced as a sum of mutually commuting projectors that energetically enforce the absence of both electric charge and magnetic flux at every vertex and plaquette of the lattice. We now turn to the formal classification of the resulting anyonic excitations by relating their charge and flux degrees of freedom to the representation theory of the Drinfeld quantum double associated with the chosen group $\mathbf{G}$.

We begin by considering the classification of magnetic flux excitations. The plaquette operators $B^h(p)$ are defined to project onto states for which the plaquette holonomy h_p takes the value $h \in \mathbf{G}$. However, this holonomy is not itself a gauge-invariant quantity. Under a local gauge transformation by an element $g \in \mathbf{G}$ at a chosen basepoint for example, the plaquette holonomy transforms by conjugation according to

$$h_p \mapsto g h_p g^{-1}. \tag{3.17}$$

As a consequence, physically meaningful magnetic flux excitations cannot be labeled by individual group elements, but rather by their conjugacy classes. The gauge-invariant characterization of magnetic flux within the quantum double $\mathbf{D}(\mathbf{G})$ is therefore given by the conjugacy class of the plaquette holonomy,

$$\mathcal{C}_{h_p} = \{g h_p g^{-1} \mid g \in \mathbf{G}\}. \tag{3.18}$$

In contrast, while magnetic flux is associated with violations of the plaquette constraints and is characterized by conjugacy classes of $\mathbf{G}$, electric charge arises from violations of the vertex constraints and is governed by the representation theory of the group. More precisely, for a vertex v, electric charge excitations correspond to states that are not invariant under local gauge transformations generated by the operators $A^g(v)$. As a

result, such excitations transform non-trivially under the action of $\mathbf{G}$. Specifically, in the presence of a magnetic flux labelled by a conjugacy class $\mathcal{C}$, the local gauge symmetry at a vertex is reduced to the subgroup of $\mathbf{G}$ that leaves a representative $h \in \mathcal{C}$ invariant under conjugation. This subgroup, known as the normalizer of h, is defined as

$$\mathcal{N}(h) = \{gh = hg \mid g \in \mathbf{G}\}. \tag{3.19}$$

Electric charge degrees of freedom associated with a flux $\mathcal{C}$ are therefore classified by the irreducible representations (irreps) of the corresponding normalizer subgroup $\mathcal{N}_g$. Different choices of representatives $h \in \mathcal{C}$ yield isomorphic normalizers, ensuring that this classification is well defined.

In this way, the elementary anyonic excitations of the quantum double model $\mathcal{D}(\mathcal{G})$ are labelled by pairs $(\mathcal{C}, \Gamma)$, where $\mathcal{C}$ is a conjugacy class of $\mathbf{G}$ specifying the magnetic flux, and Γ is an irreducible representation of the normalizer $\mathcal{N}_g$ specifying the electric charge. These pairs label the irreducible representations of the Drinfeld quantum double $\mathbf{D}(\mathbf{G})$, providing a complete classification of the model's anyonic particle types. Excitations for which $\mathcal{C}_e = \{e\}$ correspond to pure electric charges, while non-trivial conjugacy classes give rise to dyonic excitations carrying both charge and flux. An explicit example of this construction is provided in Section 4.3. The full fusion and braiding data of an anyonic model is encoded in the category $\mathrm{Rep}(\mathbf{D}(\mathbf{G}))$, a modular tensor category, whose simple objects define the superselection sectors labelling distinct anyons [121].

Finally, for any anyon labelled $X : (\mathcal{C}, \Gamma)$ we may define a quantum dimension

$$d_X = |\mathcal{C}||\Gamma|, \tag{3.20}$$

a real positive number quantifying the asymptotic growth of the fusion space dimensionality associated with a single d_X anyon, discussed further in Appendix B.1. The unique fusion channels of Abelian anyons necessarily correspond to $d_X = 1$ while $d_X > 1$ indicates a non-Abelian anyon.

The total quantum dimension, $\mathcal{D}$, of the model can be found from the sum of the quantum dimensions over all anyon types

$$\mathcal{D}^2 = \sum_{\text{anyons X}} d_X^2, \tag{3.21}$$

and is related to the cardinality of the chosen group

$$\mathcal{D}^2 = |\mathbf{G}|^2. \tag{3.22}$$

For the ground state of a two-dimensional lattice model $\mathbf{D}(\mathbf{G})$, one may define a topological entanglement entropy, γ, a universal additive constant to the total entanglement entropy that does not depend on the choice of bipartition [122]. It may be shown that this term may be expressed in terms of the total quantum dimension as $\gamma = -\log \mathcal{D}$. For all non-trivial anyon models with $\mathcal{D} > 1$, this therefore characterises some global structure of the entanglement independent of the chosen boundary required to host such a model.

3.3.2 Ribbon Operators

Having classified the elementary anyonic excitations of the quantum double model in terms of conjugacy classes and irreducible representations of normalizer subgroups, we now introduce the operators that create, transport, and braid these excitations on the lattice. These operators, known as ribbon operators, provide a concrete realization of the abstract charge-flux labels $(\mathcal{C}, \Gamma)$ and play a central role in the description of the model's topological properties.

In Section 3.3, we introduced the single-qudit operators $L_{\pm}^{g}$ and $T_{\pm}^{h}$ that may be represented as dual and direct triangles respectively as shown in Fig. 3.5(a). From these triangles, longer strips known as 'ribbons' may be constructed as illustrated in Fig. 3.5(b). This composition of dual and direct triangles notably allows operations acting along these ribbons to act simultaneously on the group degrees of freedom associated with edges and

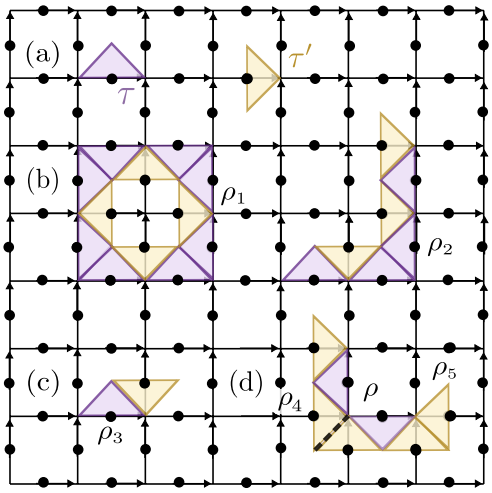

Figure 3.5: The square lattice of the quantum double model with various triangle and ribbon operators. (a) Single direct τ and dual τ' triangles (b) Closed loop, ρ_1, and open-ended, ρ_2, ribbon operators formed from combinations of triangle operators. (c) A ribbon operator with one dual and one direct triangle. (d) Two ribbons ρ_4 and ρ_5 that have been 'glued' together at the dashed line to form a single extended ribbon ρ.

plaquettes, reflecting the fact that generic excitations in the quantum double model carry both magnetic flux and electric charge. For each ribbon ρ we introduce a set of operators $\{F_\rho^{h,g}\}$ with $h, g \in \mathbf{G}$, called ribbon operators. These operators act on all qudits contained in ρ, however their action is only non-trivial on the start and end sites (i.e. the ribbon operators commute with $A(v)$ and $B(p)$ for all sites other than the end sites). In this way, stabiliser violations corresponding to excitations of the system only arise at the endpoints of the ribbon. The interior of the ribbon remains in the ground-state sector, ensuring that excitations are strictly localized.

In the simplest case, a ribbon may be constructed from a single triangle. If τ is a dual triangle and τ' a direct triangle, we set

$$F_\tau^{h,g} := \delta_{1,g} L_\tau^h, \qquad F_{\tau'}^{h,g} := T_{\tau'}^g. \tag{3.23}$$

These ribbons have minimal length $l = 1$.

A ribbon is described as 'proper' if it is composed of at least one dual and one direct

triangle. The smallest proper ribbon is thus composed of exactly one direct and one dual triangle as shown in Fig. 3.5(c). The associated ribbon operator is defined as the product of the ribbon operators on each triangle,

$$F_{\rho}^{h,g} = L_{\tau_{\text{dual}}}^{h} T_{\tau_{\text{dir}}}^{g}. \tag{3.24}$$

For all general ribbons with $l > 1$, we may let $\rho = \rho_1 \rho_2$ and recursively define a 'gluing' procedure with the following

$$F_{\rho}^{h,g} := \sum_{k \in \mathbf{G}} F_{\rho_1}^{h,k} F_{\rho_2}^{k^{-1}hk,k^{-1}g}, \tag{3.25}$$

where the first site of ρ_2 is always the same as the last site of ρ_1 (see Fig. 3.5(d)).

To obtain operators that create excitations of definite anyon type, one may further project the ribbon operators onto irreducible representations of the quantum double. This is achieved by summing over group elements with representation matrices,

$$F_{\rho}^{(\mathcal{C},\Gamma)} = \sum_{h \in \mathcal{C}} \sum_{g \in \mathcal{N}(h)} \chi^{\Gamma}(g) F_{\rho}^{h,g}, \tag{3.26}$$

where $\mathcal{C}$ is a conjugacy class of $\mathbf{G}$, $\mathcal{N}(h)$ is the stabilizer subgroup of a representative $h \in \mathcal{C}$, and χ^{Γ} denotes the character of the irrep Γ. These projected ribbon operators create excitations labelled by $(\mathcal{C}, \Gamma)$, providing a direct lattice realization of the irreducible representations of $\mathbf{D}(\mathbf{G})$. Explicit examples of this construction for the quantum double based on the permutation group of three objects, $\mathbf{D}(\mathbf{S}_3)$, are given in Appendix C.1.

3.4 Conclusion

In this chapter we have introduced the relevant background material required for chapters 4 and 5. We began with a brief overview of the defining features of anyonic models including fusion rules and braiding statistics. In particular, we highlighted the importance of the R and F matrices in uniquely specifying the braid group representation on a given

fusion basis. We then introduced Kitaev's Quantum Double model, an exactly solvable two-dimensional lattice model based on the quantum double of some finite group $\mathbf{G}$, $\mathbf{D}(\mathbf{G})$. The dynamics of this model are provided by the Kitaev Hamiltonian; a summation over commuting flux and charge projectors on each vertex and plaquette of the lattice. From the vacuum ground state of this model distinct anyon species in one-to-one correspondence with the irreducible representations of $\mathbf{D}(\mathbf{G})$, may be created and transported using so-called ribbon operators. This methodology provides the mathematical framework for the following two chapters, in which we will consider the $\mathbf{D}(\mathbf{S}_3)$ quantum double model, the simplest quantum double model capable of realising both Abelian and non-Abelian anyons. Our ultimate aim is to present a simple model, compatible with current quantum technologies, that can generate and braid non-Abelian anyons enabling an experimental demonstration of the power of such braiding operations for universal quantum computation.

Chapter 4

Lattice Realisation of R and F for the non-Abelian $D(S_3)$ Quantum Double Model

4.1 Introduction

Quantum computing offers the potential to harness the power of quantum mechanics to achieve efficient solutions to problems intractable on classical computers [123, 124, 125]. One of the main obstacles to building a practical quantum computer however, is the effect of environmental decoherence on fragile superpositions of quantum bits [126, 127, 128, 129]. Topological quantum computation provides a natural solution to this problem, in which quantum information encoded in non-local observables displays an inherent robustness to environmental perturbative errors [22, 114]. Within this framework, computation is performed via the braiding of non-Abelian anyons, enacting unitary operations on a topologically protected fusion space. The description of such braiding properties thus underpins the computational power of a given anyonic model [130, 131].

While such anyons are predicted to occur as quasiparticle excitations in certain strongly correlated quantum systems including fractional quantum Hall liquids [132, 133,

134, 135] and topological superconductors [136, 137, 138, 139], these systems have so far avoided conclusive experimental detection [26, 27, 28, 29]. As such, coherent computation via braiding in such physical systems remains beyond the scope of current experimental capability. Current efforts towards the realisation of topological quantum computation thus centre the use of physical simulations that capture key features of anyonic physics [109, 110, 111, 112, 113] without the complexities of the underlying condensed matter systems. Amongst these, Kitaev's quantum double model $\mathbf{D}(\mathbf{G})$ has emerged as a powerful candidate, providing an exactly solvable framework for the precise creation and manipulation of anyons [22, 24]. In this formalism, the braiding properties and thus computational power of the quantum double $\mathbf{D}(\mathbf{G})$ are dictated by the choice of underlying group $\mathbf{G}$. Abelian groups, such as the toric code $\mathbf{D}(\mathbf{Z}_2)$ for example, give rise to Abelian anyons only, whose braiding at most induces phase factors on the global wavefunction. When combined with logical encodings and projective measurements, these processes act to map Pauli operators to Pauli operators, thereby realising the Clifford group [140, 141]. By the Gottesman–Knill theorem [142, 143], all such Clifford operations can be efficiently simulated on a classical computer, rendering such Abelian models insufficient for the implementation of a universal quantum computer.

For the purposes of this thesis, we thus consider the quantum double model based on the smallest non-Abelian group, $\mathbf{S}_3$. This group is isomorphic to the symmetry transformations of an equilateral triangle with group elements that may be indexed as

$$\mathbf{S}_3 = \{e, c, c^2, t, tc, tc^2\}, \tag{4.1}$$

where c is the generator for rotations following $c^3 = e$, and t is the generator for reflections following $t^2 = e$ with e as the identity element. The non-Abelian nature of this group is defined by the relation $ct = tc^2$. As remarked by Lo et al. in their review [144], the quantum double model $\mathbf{D}(\mathbf{S}_3)$ lies at the 'sweet spot' for the realisation of non-Abelian topological order, being both solvable and non-nilpotent [145]. Indeed it has been shown that the non-Abelian anyons of this model can perform universal

quantum computation through braiding and fusion alone [146, 147]. Furthermore, as $\mathbf{S}_3$ is the smallest non-Abelian group, the lattice needed to realise such a model has a relatively small local Hilbert space, rendering it more readily accessible to current small-scale quantum platforms [148].

In this chapter, we present an explicit demonstration of the non-Clifford operations arising from the pairwise braiding of non-Abelian anyons in the framework of the $\mathbf{D}(\mathbf{S}_3)$ quantum double model. By employing controlled sequences of localized ribbon and projection operators to a lattice of $d = 6$ qudits, we simulate the action of the fundamental exchange and fusion recombination matrices, R and F, on the topologically protected fusion space of non-Abelian G anyons. These matrices fully characterize the braiding statistics, enabling the reconstruction of the complete braiding operators acting on the fusion space of two anyon pairs. Analysis of these operators reveals that the braiding of G anyons enacts non-Clifford operations on a logical qubit encoded within this fusion space. Crucially, we conclusively show that the resulting braiding matrices enable the generation of magic states [149, 150], establishing a direct link between the non-Abelian braiding dynamics of $\mathbf{D}(\mathbf{S}_3)$ and one of the key resources required for universal quantum computation [151].

Notably, the protocol presented here provides a static method for the reconstruction of non-Abelian braiding statistics. In principle, the simulation of such evolutions requires the physical transport of anyons [109, 152, 153]. Within a quantum simulation, however, such dynamical processes demand complex controlled evolutions capable of transporting anyons without performing unwanted measurement on their encoded information [154]. To bypass this complexity, we adopt an algebraic approach in which braiding is simulated using only localized operators that create and measure anyons. In this sense, our method offers a natural translation of Bonderson et al.'s 'measurement-only' paradigm for topological quantum computation [155, 156] into the well-defined framework of Kitaev's quantum double model. Concretely, by performing projective charge measurements, we coherently select states from the multi-dimensional fusion space of non-Abelian anyons

generated by overlapping ribbon operators on a single vertex. By varying the order of these ribbon operators, we simulate both the braiding transformations encoded by the R matrix, and the basis changes associated with the fusion order, captured by the F matrix. In this way, the ordered application of static lattice operations reproduces the effect of anyonic braiding in time rather than in space. Importantly, this minimal, operator-based approach within the smallest non-Abelian quantum double model provides a clear and experimentally accessible route to realisation on current quantum hardware, which will be the focus of Chapter 5.

The rest of this chapter is organised as follows. In Section 4.2 we begin by providing a brief overview of the importance and role of magic state generation in schemes for universal quantum computation. In Section 4.3 we then introduce the main elements of the $\mathbf{D}(\mathbf{S}_3)$ quantum double model and the eight distinct anyons it supports. Of particular interest for our purposes is the non-Abelian anyon G of the subgroup $\{A, B, G\}$, the braiding evolutions of which are encoded in the braiding and fusion recombination matrices R^{GG} and F^G_{GGG} respectively. In Section 4.4 we present a simple method for the simulation of R^{GG} on a lattice of $d = 6$ qudits, while a minimal construction for the fusion basis transformation F^G_{GGG} is given in Section 4.5. In Section 4.6, these extracted matrices are shown to explicitly demonstrate the non-Clifford action of the braiding of G anyons, highlighting their importance as a resource for universal quantum computation. Finally, Section 4.7 provides concluding remarks and outlook.

4.2 A brief introduction to magic

In recent years, 'magic' or 'non-stabilizer' states have emerged as a powerful resource in quantum computation, bridging the gap between efficiently simulable Clifford circuits and full universal quantum computation [149, 151]. Here we provide a brief overview of the key properties of these states, motivating the significance of their controlled generation through topologically protected braiding operations.

We begin by introducing the Clifford group. Formally, the n-qubit Clifford group is

defined as

$$\mathcal{C}_n = \{U | UPU^{-1} \in \mathcal{P}_n \quad \forall P \in \mathcal{P}_n\}, \tag{4.2}$$

that is, the set of unitary operations that map the n-qubit Pauli group

$$\mathcal{P}_n = \{\pm 1, \pm i\} \times \{\mathbf{1}_2, \sigma^x, \sigma^y, \sigma^z\}^{\otimes n}, \tag{4.3}$$

onto itself under conjugation [157]. The Clifford group plays a notable role in quantum information theory due to its close connection with classical simulability. In particular, the Gottesman-Knill theorem establishes that any quantum circuit composed solely of Clifford operations, together with preparation of computational basis states and measurements in the Pauli basis, can be efficiently simulated on a classical computer [142]. As a consequence, circuits restricted to Clifford gates alone do not provide a quantum computational advantage.

Although the Clifford group is not universal for quantum computation, it is a well-established result that augmenting the Clifford group with any non-Clifford gate yields a universal gate set [158, 159]. A commonly employed choice is the single-qubit T-gate

$$T = \begin{pmatrix} 1 & 0 \\ 0 & e^{\frac{i\pi}{4}} \end{pmatrix}, \tag{4.4}$$

which, when combined with Clifford operations, suffices to approximate arbitrary unitary transformations [160]. Despite this theoretical universality however, the physical implementation of such non-Clifford gates presents significant practical challenges [161]. In many fault-tolerant architectures for example, Clifford operations can be implemented transversally and are therefore naturally protected against errors [162, 163], whereas non-Clifford gates generally lack such protection and incur substantial overheads [164, 165].

In the seminal work [149], Bravyi and Kitaev proposed an alternative scheme for universal quantum computation, whereby the non-Clifford action of gates such as the T-gate, could be 'encoded' in a special set of ancillary input states, circumventing the need

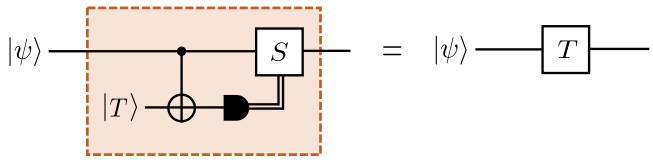

Figure 4.1: Magic state injection protocol for the non-Clifford T gate. By preparing the ancillary qubit in the magic state $|T\rangle$ in Eq. (4.5), the left circuit composed of Clifford operations, measurements and classical feed-forward reproduces the action of the non-Clifford gate T on the input state $|\psi\rangle$ as shown on the right. Note that the $S = T^2$ gate (left) is conditioned to only act on the computational qubit if '1' is measured on the ancillary qubit.

for direct implementation of any non-Clifford gates within the quantum circuit. Defining the set of stabilizer states as the finite set of n-qubit states that can be generated by applying Clifford operations to the product state $|0, 0, \ldots, 0\rangle$, *non*-stabilizer or 'magic' states thus represent a departure from the realm of classically simulable states. By 'injecting' these magic states into the circuit, the rest of the computation may then be performed using only the efficiently simulable gates from the Clifford group.

To illustrate the procedure of this magic state injection protocol, we consider the use of the magic state

$$|T\rangle = \frac{1}{\sqrt{2}}\left(|0\rangle + e^{\frac{i\pi}{4}}|1\rangle\right), \tag{4.5}$$

in replicating the action of the non-Clifford T gate as shown in Figure 4.1. Here the S-gate is a Clifford gate $S = T^2$ that is conditionally applied depending on the outcome of a measurement performed on an ancilla qubit. Taking some arbitrary input state $|\psi\rangle = \alpha|0\rangle + \beta|1\rangle$, the total input including the ancillary state $|T\rangle$ is given by

$$|\Psi_{\text{in}}\rangle = |\psi\rangle \otimes |T\rangle = (\alpha|0\rangle + \beta|1\rangle) \otimes \frac{1}{\sqrt{2}}\left(|0\rangle + e^{\frac{i\pi}{4}}|1\rangle\right), \tag{4.6}$$

such that after the action of the CNOT gate, one obtains

$$\left(\alpha|0\rangle + \beta e^{\frac{i\pi}{4}}|1\rangle\right) \otimes |0\rangle + \left(\alpha e^{\frac{i\pi}{4}}|0\rangle + \beta|1\rangle\right) \otimes |1\rangle. \tag{4.7}$$

A projective measurement is then performed on the ancilla qubit. If the outcome is $|0\rangle$, the input register is projected onto

$$\left(\alpha\,|0\rangle + \beta e^{\frac{i\pi}{4}}\,|1\rangle\right) = T\,|\psi\rangle \tag{4.8}$$

and the desired operation is obtained directly. If instead the outcome is $|1\rangle$, a corrective S-gate is applied to the input qubit, yielding

$$S\left(\alpha e^{\frac{i\pi}{4}}\,|0\rangle + \beta\,|1\rangle\right) = \left(\alpha e^{\frac{i\pi}{4}}\,|0\rangle + e^{\frac{i\pi}{2}}\beta\,|1\rangle\right) = e^{\frac{i\pi}{4}}\left(\alpha\,|0\rangle + \beta e^{\frac{i\pi}{4}}\,|1\rangle\right) = e^{\frac{i\pi}{4}}T\,|\psi\rangle\,, \tag{4.9}$$

which reproduces the action of the T-gate up to a global phase. In this way, the injection of a single magic T-state ancilla enables the implementation of a non-Clifford gate using only Clifford operations, measurements, and classical feed-forward.

In order to formalise the role of magic as a resource, we finally introduce the stabilizer Rényi entropy, M_α [151, 166]. This provides a quantitative measure of the magic content of a quantum state, capturing the extent to which it deviates from a stabilizer state. For an n-qubit state $|\psi\rangle$, $M_\alpha(|\psi\rangle)$ is defined in terms of the squared overlaps with elements of the n-qubit Pauli group $\mathcal{P}_n$ as

$$M_\alpha(|\psi\rangle) = \frac{1}{1-\alpha}\log\left(\sum_{p\in\mathcal{P}_n}\frac{|\,\langle\psi|\,p\,|\psi\rangle\,|^{2\alpha}}{2^n}\right), \tag{4.10}$$

where $\alpha > 0$ is the Renyi index. $M_\alpha = 0$ indicates a classically simulable state, while larger values of M_α indicate greater deviation from the Clifford-stabilizer set, and hence higher magic. Typically we refer to the second-order stabilizer Renyi entropy, which for a single qubit state, is bounded as $0 \leq M_2 \leq \log(2)$. The state $|T\rangle$ as in Eq. (4.5) for example, takes value $M_2(|T\rangle) = \log(\frac{4}{3})$.

With the increasing recognition of magic states as a key resource for universal quantum computation, growing attention has been directed towards identifying physical platforms capable of generating such states in a controlled and fault-tolerant manner. Substantial

progress has been made in the theory and practice of a process known as magic-state distillation for example, whereby high-fidelity magic states may be 'distilled' from multiple lower fidelity inputs [149, 167, 150, 168]. While such protocols are provably effective, they typically incur significant overheads in terms of qubit count, circuit depth, and error-correction resources [169], motivating the search for alternative approaches that can generate magic states more directly.

Topological quantum computing architectures offer a particularly appealing route to addressing the challenge of implementing non-Clifford resources, as their intrinsic error protection can be leveraged to stabilise highly non-classical quantum states [141, 170, 171]. In the following section, we introduce the $\mathbf{D}(\mathbf{S}3)$ quantum double model, which supports non-Abelian anyonic excitations whose braiding statistics enable the generation of magic states encoded in the logical fusion space of four G anyons. The computational relevance of such states has been recently highlighted in the hybrid scheme proposed by Laubscher, Loss, and Wootton [172], in which small islands of the non-Abelian $\mathbf{D}(\mathbf{S}3)$ quantum double embedded within a toric-code architecture act as 'magic-state factories' to promote an otherwise Clifford-restricted surface code to universal quantum computation. In that work, magic states prepared through non-Abelian braiding are subsequently injected into the surrounding stabilizer code, providing a concrete pathway to fault-tolerant universality. The explicit demonstration of such magic-state generation within the exactly solvable framework of the quantum double model presented in this chapter thus serves to bridge abstract theoretical constructions with concrete, implementable schemes for universal topological quantum computation.

4.3 The $\mathbf{D}(\mathbf{S}_3)$ Quantum Double Model

Here, we provide a brief overview of the key properties of $\mathbf{D}(\mathbf{S}_3)$, the simplest quantum double model that can support non-Abelian anyons [22]. The group $\mathbf{S}_3$ has three con-

Anyon	$\mathcal{C}_g$	$\mathcal{N}_g$	Irrep.	d_X	Type
A	$\mathcal{C}_e$	S_3	$\Gamma_1^{S_3}$	1	Vacuum
B	$\mathcal{C}_e$	S_3	$\Gamma_{-1}^{S_3}$	1	Chargeon
C	$\mathcal{C}_e$	S_3	$\Gamma_2^{S_3}$	2	Chargeon
D	$\mathcal{C}_t$	$\mathbb{Z}_2$	$\Gamma_1^{\mathbb{Z}_2}$	3	Fluxon
E	$\mathcal{C}_t$	$\mathbb{Z}_2$	$\Gamma_{-1}^{\mathbb{Z}_2}$	3	Dyon
F	$\mathcal{C}_c$	$\mathbb{Z}_3$	$\Gamma_1^{\mathbb{Z}_3}$	2	Fluxon
G	$\mathcal{C}_c$	$\mathbb{Z}_3$	$\Gamma_\omega^{\mathbb{Z}_3}$	2	Dyon
H	$\mathcal{C}_c$	$\mathbb{Z}_3$	$\Gamma_{\bar{\omega}}^{\mathbb{Z}_3}$	2	Dyon

Table 4.1: Anyons of $\mathbf{D}(S_3)$ with their charge and flux labels, quantum dimensions and type.

jugacy classes

$$\begin{aligned} \{\mathcal{C}_e\} &= \{e\}, \\ \{\mathcal{C}_c\} &= \{c, c^2\}, \\ \{\mathcal{C}_t\} &= \{t, tc, tc^2\}, \end{aligned} \tag{4.11}$$

with corresponding normalizers,

$$\begin{aligned} \mathcal{N}_e &= S_3, \\ \mathcal{N}_c = \mathcal{N}_{c^2} &= \{e, c, c^2\} \cong \mathbb{Z}_3, \\ \mathcal{N}_t = \{e, t\} &\cong \mathcal{N}_{tc} \cong \mathcal{N}_{tc^2} \cong \mathbb{Z}_2, \end{aligned} \tag{4.12}$$

where '$\cong$' denotes an isomorphism, generating a total of eight irreducible representations [173]. Each irrep is identified with a distinct anyon type, labelled $\{A, B, C, D, E, F, G, H\}$, as listed in Table 4.1. A denotes the vacuum particle with both trivial flux and charge, such that $A \times X = X$ for $X \in \{A, B, \ldots, H\}$. Both A and B are Abelian, while $C, \ldots, H$ are non-Abelian.

Instead of considering the complete set of eight anyons however, it is instructive to restrict to a smaller sub-group of this model that is closed under fusion. In this way, the non-Abelian properties may be retained, while reducing the complexity of theoretical and experimental treatment [148]. Here we will consider the sub-group $\{A, B, G\}$ where

A is the vacuum, B is an Abelian chargeon and G is a non-Abelian dyon. Their fusion relations found using the S matrix and Verlinde formula [174] are given by

$$A \times A = B \times B = A, \quad G \times B = G, \quad G \times G = A + B + G. \tag{4.13}$$

The fusion multiplicity of the G anyon signals its non-Abelian nature such that the fusion space of a pair of G anyons forms a three-dimensional Hilbert space spanned by a set of anyonic basis states $|G, G \to i\rangle$ where $G, G \to i$ indicates the fusion of two G anyons to outcome $i = A, B, G$. The R and F matrices of the G anyons may be found analytically using the pentagon and hexagon relations [175] and take the forms

$$R^{GG} = \begin{pmatrix} \omega & 0 & 0 \\ 0 & -\omega & 0 \\ 0 & 0 & \bar{\omega} \end{pmatrix}, \quad F^{G}_{GGG} = \frac{1}{2} \begin{pmatrix} 1 & 1 & \sqrt{2} \\ 1 & 1 & -\sqrt{2} \\ \sqrt{2} & -\sqrt{2} & 0 \end{pmatrix}, \tag{4.14}$$

with $\omega = e^{\frac{2\pi i}{3}}$ and $\bar{\omega} = \omega^*$. Such matrices completely encode the description of all unitary braiding evolutions associated with a given anyonic model [117, 176]. In the following we provide an explicit derivation for the braid group $\mathcal{B}_3$ on the fusion space of four G anyons. In this way, we see that the R and F matrices of Equation (4.14) yield a braiding operation with non-Clifford action on the logical Hilbert space, emphasising the role of these G anyons as a resource for universal quantum computation.

4.3.1 Magic state generation through non-Abelian braiding

Consider the creation of two pairs of G anyons from the vacuum as shown in Figure 4.2(a). The subsequent fusion of the pair (G_1, G_2) has three possible outcomes $i = A, B, G$. As each of these anyons is its own antiparticle, the pair (G_3, G_4) must fuse to the same composite anyon i such that the total system stays within the vacuum superselection sector. One therefore obtains a three-dimensional fusion basis with states specified by the intermediate anyon i. Alternatively, with the omission of the paths of trivial vacuum

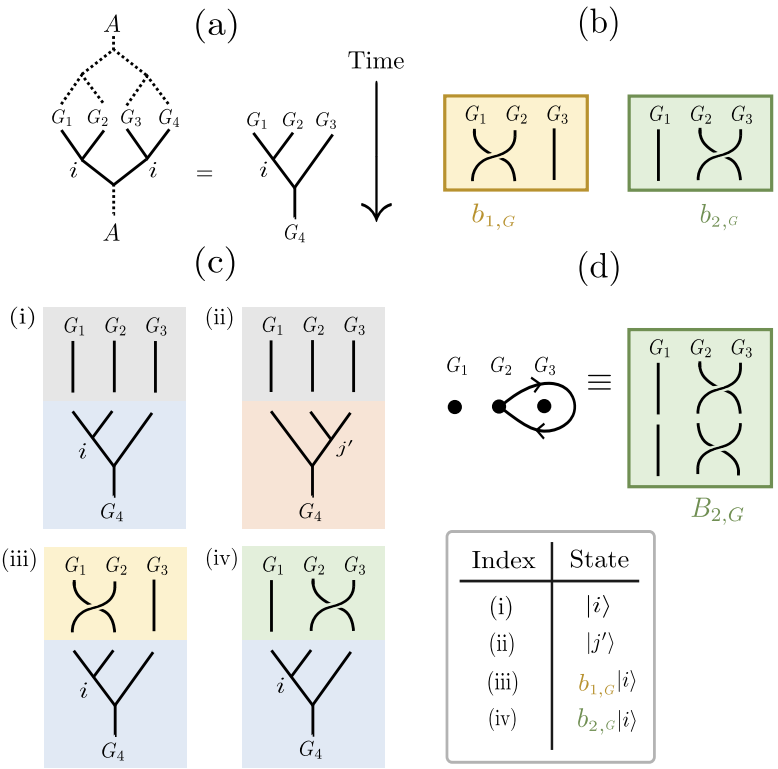

Figure 4.2: (a) Two equivalent anyonic fusion states. (b) The braid generators $b_{1,G}$ and $b_{2,G}$ on the worldlines of three G anyons. (c) Representation of the basis states $|i\rangle$ and $|j'\rangle$ and their action under the briad group operations. (d) Repeated application of $b_{2,G}$ yields the full braiding operator $B_{2,G}$

anyons, this system may be viewed as the fusion of three G anyons to fixed outcome G as shown in Figure 4.2(a). With this fixed order of fusion the three-dimensional basis may be explicitly spanned by the states $\{|i\rangle\} \equiv \{|(G_1, G_2), G_3 \to i, G_3 \to G_4\rangle\}$ for $i = A, B, G$. As introduced in the previous chapter, anyonic associativity means that this fusion of three G anyons to a fixed outcome may equivalently correspond to the basis $|j'\rangle = |G_1, (G_2, G_3) \to G_1, j' \to G_4\rangle$, with the two bases related by the matrix F^G_{GGG} through $|i\rangle = \sum_{j'} (F^G_{GGG})^i_{j'} |j'\rangle$, and $|j'\rangle = \sum_i (F^{G\ -1}_{GGG})^{j'}_i |i\rangle$.

The topologically distinct paths of G_1, G_2 and G_3 prior to fusion form the 3-strand braid group $\mathcal{B}_3$. This group has two generators $b_{1,G}$ and $b_{2,G}$ braiding pairs (G_1, G_2) and (G_2, G_3) respectively as shown. When acting on a defined fusion space, the action of these braiding operations may be expressed as a product of R and F matrices. Consider

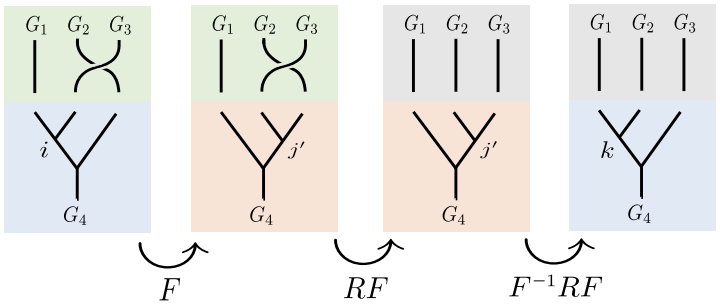

Figure 4.3: The action of the braiding operator $b_{2,G}$ on the basis state $|i\rangle$ may be understood through a series of R and F moves as shown.

for example $b_{1,G}\,|i\rangle$ as shown in Figure 4.2(c)(iii). The anyons G_1 and G_2 share a direct fusion channel such that we have simply

$$b_{1,G}\,|i\rangle = R^{GG}\,|i\rangle\,. \tag{4.15}$$

In contrast, in the basis $\{|i\rangle\}$ the anyons G_2 and G_3 do not fuse directly and thus the matrix F^G_{GGG} must be used to form a description of the operation $b_{2,G}$ [176]. Through the series of transformations illustrated in Figure 4.3 one obtains

$$\begin{aligned} b_{23}\,|x\rangle &= b_{23}\left(\sum_{x'}(F^G_{GGG})^x_{x'}\,|x'\rangle\right), \\ &= \sum_{x'} R^{GG}_{x'}(F^G_{GGG})^x_{x'}\,|x'\rangle\,, \\ &= \sum_{x'} R^{GG}_{x'}(F^G_{GGG})^x_{x'}\left(\sum_{y}(F^G_{GGG})^{x'}_{y}\,|y\rangle\right), \\ &= \sum_{y}\left(\sum_{x'}(F^{G\,-1}_{GGG})^{x'}_{y}\,R^{GG}_{x'}(F^G_{GGG})^x_{x'}\right)|y\rangle\,. \end{aligned} \tag{4.16}$$

Thus, through the symmetry of F^G_{GGG},

$$b_{2,G}\,|x\rangle = F^{G\,-1}_{GGG}R^{GG}F^G_{GGG}\,|x\rangle\,. \tag{4.17}$$

Direct substitution of R^{GG} and F^G_{GGG} thus yields exact expressions for the generators

$b_{1,G}$ and $b_{2,G}$. As we will discuss further in Section 4.4 however, the single exchange R is not directly represented as a physical operation within the formalism of the quantum double model. Instead, the observable that naturally appears from commutation relations of ribbon operators is the monodromy (full braiding) operator R^2 [177, 178]. In this protocol we therefore consider the full braiding operators

$$\begin{aligned} B_{1,G} &\equiv (b_{1,G})^2 = (R^{GG})^2, \\ B_{2,G} &\equiv (b_{2,G})^2 = F^{G\,-1}_{GGG}(R^{GG})^2 F^{G}_{GGG}, \end{aligned} \tag{4.18}$$

describing complete evolutions of G_1 around G_2 and G_2 around G_3 respectively (see Figure 4.2). Explicitly, $B_{2,G}$ has the following action on the anyonic basis $\{|A\rangle, |B\rangle, |G\rangle\}$

$$B_{2,G} = \begin{pmatrix} \cos\left(\frac{2\pi}{3}\right) & -i\sin\left(\frac{2\pi}{3}\right) & 0 \\ -i\sin\left(\frac{2\pi}{3}\right) & \cos\left(\frac{2\pi}{3}\right) & 0 \\ 0 & 0 & \bar{\omega} \end{pmatrix}. \tag{4.19}$$

Revealing a splitting in the qutrit subspace as this operation preserves the two-dimensional subspace $\mathrm{span}(|A\rangle, |B\rangle)$ and its orthogonal complement $\mathrm{span}(|G\rangle)$. The monodromy $B_{2,G}$ is thus a well-defined operation on a qubit encoded in terms of the reduced basis $\{|A\rangle, |B\rangle\}$. Notably, inspection of this logical operation reveals that it does not belong to the single-qubit Clifford group $\mathcal{C}_1$. Furthermore, creating two pairs of G anyons from the vacuum and performing the braiding operation $B_{2,G}$ enables the preparation of the state

$$|\psi\rangle = B_{2,G}|A\rangle = \cos\left(\frac{2\pi}{3}\right)|A\rangle - i\sin\left(\frac{2\pi}{3}\right)|B\rangle, \tag{4.20}$$

a magic state with $M_2(|\psi\rangle) = \log\left(\frac{16}{13}\right)$. This non-stabilizer state constitutes a crucial resource for quantum computation, whereby the encoded non-Clifford action enables the preparation of arbitrary quantum states using circuits composed solely of classically simulable Clifford operations [172].

To illustrate the relative computational power of these G anyons, we provide a brief

comparison with an alternative non-Abelian subgroup of $\mathbf{D}(\mathbf{S}_3)$, the charge subgroup $\{A, B, C\}$ [179]. The non-Abelian chargeon C has identical fusion rules to that of the G anyon

$$A \times A = B \times B = A, \quad C \times B = G, \quad C \times C = A + B + C, \tag{4.21}$$

such that a set of four C anyons similarly encodes a logical qutrit. The form of the braiding matrix

$$R^{CC} = \begin{pmatrix} 1 & 0 & 0 \\ 0 & -1 & 0 \\ 0 & 0 & 1 \end{pmatrix}, \tag{4.22}$$

acting on the basis $\{|A\rangle, |B\rangle, |C\rangle\}$ however, yields $(R^{CC})^2 = \mathbf{1}_3$. As a result the braiding operators $B_{1,C} = (R^{CC})^2 = \mathbf{1}_3$ and $B_{2,C} = F^{C\,-1}_{CCC}(R^{CC})^2 F^{C}_{CCC} = \mathbf{1}_3$ act trivially on this fusion space, rendering this alternative subgroup unable to manifest non-trivial braiding statistics within the quantum double model.

This discussion thus serves to illustrate the potential computational power arising from the pairwise braiding of non-Abelian G anyons. With the basic components of the $D(S_3)$ quantum double model introduced in the next section, we thus seek to explicitly demonstrate the non-Clifford action of these braiding operations through simple operations on a lattice of $d = 6$ qudits.

4.3.2 Anyonic manipulation on a lattice

We now present the lattice model that gives rise to the quantum double $\mathbf{D}(\mathbf{S}_3)$ presented above. Consider a two-dimensional square lattice with orientation as shown in Figure 4.4. On each link of the lattice a Hilbert space, $\mathbf{H}$, described by $d = 6$ qudits ($\dim(\mathbf{H}) = 6$) is placed with orthonormal basis indexed by the group elements of $\mathbf{S}_3$, $\{|g\rangle : g \in \mathbf{S}_3\}$

The dynamics of our model are given by the Kitaev Hamiltonian [22]

$$\mathcal{H} = -\sum_{v} A(v) - \sum_{p} B(p), \tag{4.23}$$

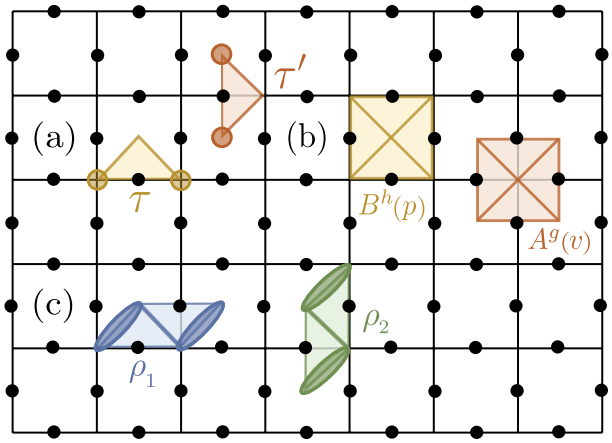

Figure 4.4: The lattice construction of the quantum double model $\mathbf{D}(\mathbf{S}_3)$. A $d = 6$-dimensional qudit is positioned on each link of the direct lattice, which adopts the orientation convention of Fig. 3.4. (a) Direct and dual triangles τ and τ' respectively act on single $d = 6$ qudits. Ribbon operators acting on these triangles create pure charge or flux anyons as shown. (b) Closed loops of direct (dual) triangles form the basis for mutually commuting flux (charge) projection components $B^h(p)$ ($A^g(v)$). (c) The two G anyonic ribbons ρ_1 and ρ_2 that will be used throughout this chapter. The dyons created by the associated ribbon operators $F^G_{\rho_1}$ and $F^G_{\rho_2}$ are situated at the endpoints of each ribbon as highlighted.

for vertex and plaquette operators $A(v)$ and $B(p)$ respectively as defined in Equations (3.13) and (3.12). We consider a lattice with open direct lattice boundaries such that Hamiltonian terms outside of these boundary lines are set to zero [180]. This model produces a unique ground state $|\zeta\rangle$, corresponding to the anyonic vacuum, in which

$$A(v)\,|\zeta\rangle = |\zeta\rangle\,, \quad B(p)\,|\zeta\rangle = |\zeta\rangle\,, \tag{4.24}$$

for all vertices, v, and plaquettes, p.

The anyonic excitations of this model are in one-to-one correspondence with the irreps of the Drinfeld double $D(S_3)$. The anyons in our reduced model $\{A, B, G\}$ may be coherently created and manipulated with the application of so-called ribbon operators to this anyonic ground state. The A and B anyons are both Abelian with trivial flux, and can therefore be created and moved with string operators corresponding to paths on the direct lattice. As A is the vacuum particle, the operator F^A acts trivially as the identity

matrix. Both A and B anyons may be transported around the lattice by applying these single-qudit ribbon operators to strings of qudits (see Appendix C.1). In contrast, the G anyons are dyons that have both non-trivial flux and charge. They therefore require the implementation of ribbon operators composed of dual and direct triangles for their manipulation [178]. A simple ribbon operator capable of producing a pair of G anyons can be composed of one direct and one dual triangle, $\rho = \tau_{\text{direct}}\tau_{\text{dual}}$. In the following we will consider two distinct two-qudit ribbon operators,

$$f^G_{\rho_1} = (T^e_- + \omega T^c_- + \bar{\omega} T^{c^2}_-) \otimes L^c_- + (T^e_- + \bar{\omega} T^c_- + \omega T^{c^2}_-) \otimes L^{c^2}_-, \tag{4.25}$$

and

$$f^G_{\rho_2} = L^c_+ \otimes (T^e_- + \omega T^c_- + \bar{\omega} T^{c^2}_-) + L^{c^2}_+ \otimes (T^e_- + \bar{\omega} T^c_- + \omega T^{c^2}_-), \tag{4.26}$$

as illustrated in Figure 4.4(c). Here, $f^G_{\rho_i}$ refers specifically to the non-trivial two-qudit action of these operators, the action of these operators on the full Hilbert space of a lattice of arbitrary dimensionality is represented by $F^G_{\rho_i}$ where

$$F^G_{\rho_i} = \mathbf{1}_6 \otimes \ldots \mathbf{1}_6 \otimes f^G_{\rho_i} \otimes \mathbf{1}_6 \cdots \otimes \mathbf{1}_6, \tag{4.27}$$

as appropriate. We note that both of these operators are Hermitian but not unitary. Nevertheless, when restricted to act on the eigenstates of (4.23), they return normalised states [153]. These ribbons are sufficient to demonstrate the fusion and braiding properties of the G anyons of $\mathbf{D}(\mathbf{S}_3)$, given in Equation (4.14), as we shall see in the next sections.

Finally, we will introduce a set of local measurement operators that distinguish between each anyon type. This is particularly useful when we want to determine the fusion outcome of two anyons while constructing anyonic basis states such as $|G, G \to i\rangle$, with $i = A, B, G$. Locality dictates that when two anyons fuse together to produce some overall particle type then both fusing particles must be measured jointly [176]. The initial

anyons may be spatially separated, in which case the fusion outcome measurement must be performed around a loop that surrounds both anyons under fusion. For the operations considered here we ensure that the pair of particles undergoing fusion share a common vertex. In this way each outcome A, B, G can be measured by the respective four-body vertex projection operators

$$\begin{aligned} a^A(v) &= \frac{1}{6}\Big(a^e(v) + a^c(v) + a^{c^2}(v) + a^t(v) + a^{tc}(v) + a^{tc^2}(v)\Big), \\ a^B(v) &= \frac{1}{6}\Big(a^e(v) + a^c(v) + a^{c^2}(v) - a^t(v) - a^{tc}(v) - a^{tc^2}(v)\Big), \\ a^G(v) &= \frac{1}{3}\Big(2a^e(v) - a^c(v) - a^{c^2}(v)\Big), \end{aligned} \tag{4.28}$$

as in [173], which project onto the chosen anyon by measuring the charge. The action of these four-qudit operations on a lattice of arbitrary dimensionality is labelled by

$$A^i(v) = \mathbf{1}_6 \otimes \ldots \mathbf{1}_6 \otimes a^i(v) \otimes \mathbf{1}_6 \cdots \otimes \mathbf{1}_6. \tag{4.29}$$

These vertex projection operators form a set of orthogonal projective measurements as indicated by the identities

$$A^i(v)A^j(v) = \delta_{i,j}A^i(v), \qquad \sum_{i\in\{A,B,G\}} A^i(v) = \mathbf{1}, \tag{4.30}$$

and are thus sufficient in uniquely distinguishing between the possible anyonic charges that lay on a chosen vertex v. For example, for the ground state anyonic vacuum, $|\zeta\rangle$, $A^A(v)\,|\zeta\rangle = |\zeta\rangle$ and $A^B(v)\,|\zeta\rangle = A^G(v)\,|\zeta\rangle = 0$, for all vertices.

In order to further illustrate the action of these vertex operators consider Figure 4.5. The ribbon $F^G_{\rho_1}$ creates a pair of G dyons with sites lying on vertices v_1 and v_2. As the charge of the G anyons is unique in the subgroup {A, B, G}, it is sufficient to project G anyonic states with the vertex projector $A^G(v)$ as opposed to the full charge and flux projector P^G, which requires extra operators on the plaquette to project the flux of the G anyons (see [173]). Application of A^G to either vertex will therefore preserve the

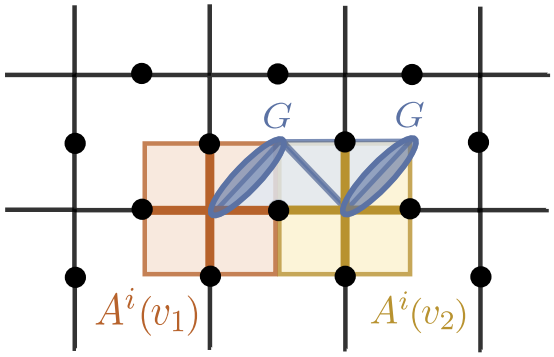

Figure 4.5: The anyonic ribbon operator $F^G_{\rho_1}$ creates a pair of G dyons at the endpoints of the ribbon ρ_1 as verified by the charge projection operators $A^i(v_1)$ and $A^i(v_2)$.

state, $A^G(v_1)F^G_{\rho_1}|\zeta\rangle = F^G_{\rho_1}|\zeta\rangle$, verifying the creation of a G anyon, while $A^A(v_1)F^G_{\rho_1}|\zeta\rangle = A^B(v_1)F^G_{\rho_1}|\zeta\rangle = 0$ (and similarly for v_2). By employing these projectors on the lattice we can also verify the fusion rules of two G anyons as given in (4.13). The repeated application of $F^G_{\rho_1}$ produces a pair of G dyons at both v_1 and v_2. Applying a vertex projection operator to either vertex therefore measures the fusion of two G anyons at that point. For example, it is found that

$$\begin{aligned} A^A(v_1)(F^G_{\rho_1})^2|\zeta\rangle &= |\zeta\rangle\,, \\ A^B(v_1)(F^G_{\rho_1})^2|\zeta\rangle &= F^B_{\tau_1}|\zeta\rangle\,, \\ A^G(v_1)(F^G_{\rho_1})^2|\zeta\rangle &= F^G_{\rho_1}|\zeta\rangle\,, \end{aligned} \tag{4.31}$$

where $F^B_{\tau_1}$ is the direct triangle ribbon operator producing a pair of B anyons on vertices v_1 and v_2, indicating that the fusion of a pair of G anyons gives rise to a superposition of A, B and G anyons as dictated by the fusion rule $G \times G = A + B + G$.

4.4 R matrix derivation

In Section 4.3 we introduced the matrices R^{GG} and F^G_{GGG}, describing the statistical evolutions of the non-Abelian G anyons of the $D(S_3)$ quantum double model. The implementation of these evolutions within the framework of the quantum double was first

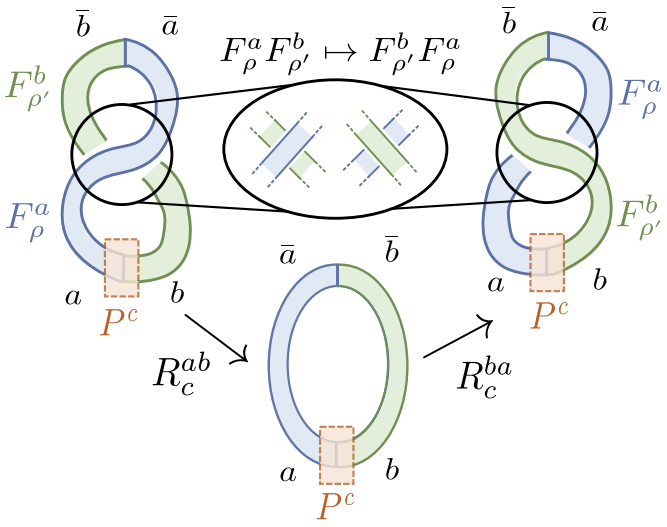

Figure 4.6: Derivation of the phase $R^{ab}_c R^{ba}_c$ from two equivalent processes on the ribbon operators F^a_ρ and $F^b_{\rho'}$, creating pairs of anyons $(a, \bar{a})$ and $(b, \bar{b})$ respectively. The generalized projection operator P^c fixes the fusion channel $a \times b = c$. To highlight the topological equivalence of certain configurations, the ribbons ρ and ρ' are abstracted as smoothly deformable strips with no explicit construction on the lattice. (top) Exchanging the order of operation of these two ribbons is equivalent to exchanging the paths on which they overlap. (bottom) The same final configuration is alternatively obtained by two successive braiding processes, each characterised by an R phase, yielding the relation (4.33).

considered by Kitaev in his foundational work [22]. Here, we begin by presenting such a method by which experimentally accessible ribbon operators may be used to extract the braiding properties of G anyons contained in the matrix elements of $(R^{GG})^2$.

4.4.1 R matrix from ribbon operators

Consider the ribbon operators F^a_ρ and $F^b_{\rho'}$, creating pairs of anyons $(a, \bar{a})$ and $(b, \bar{b})$ respectively as shown in Figure 4.6. By considering two equivalent sets of operations connecting the products $F^a_\rho F^b_{\rho'}$ and $F^b_{\rho'} F^a_\rho$ we will show how the elements of the braiding matrix R^{ab} may be extracted from the commutativity of reduced ribbon operators. First, consider exchanging the order of F^a_ρ and $F^b_{\rho'}$, as shown in the top line of Figure 4.6. For all points where the two ribbons do not overlap (indicating action on different qudits on the lattice), such an exchange is trivial. Alternatively, the exchange of these ribbon operators

may be interpreted in terms of the projection of the braiding of anyonic worldlines. Both ribbons share common start and end points such that the fusion outcome $a \times b \to c$ may be fixed with the application of a localised projection operator P^c to the point of overlap of a and b (superselection rules then dictate that $\bar{a} \times \bar{b} \to \bar{c}$ such that the total system will still fuse to the vacuum). By analogy with Figure 3.1(a), 'undoing' the braiding of the ribbons on the LHS with a clockwise rotation therefore produces any topologically equivalent configuration to that in the centre of Figure 4.6 with an additional factor R_c^{ab}. A second clockwise braiding operation brings about another factor of R_c^{ab} giving eventually the final configuration on the right. In the anyonic basis such a set of transformations may be represented as

$$R_{\circlearrowleft}^2 \left|a, b \to c\right\rangle = R_c^{ab} R_c^{ba} \left|a, b \to c\right\rangle, \tag{4.32}$$

where $R_{\circlearrowleft} \left|a, b \to c\right\rangle$ describes the anti-clockwise exchange of anyons a and b with fixed fusion channel c.

By comparison of these two equivalent processes, we therefore observe that the values $R_c^{ab} R_c^{ba}$ are encoded in the exchange of overlapping ribbon operators as

$$P^c F_\rho^a F_{\rho'}^b = R_c^{ab} R_c^{ba} P^c F_{\rho'}^b F_\rho^a. \tag{4.33}$$

In the following we show how to explicitly reconstruct the matrix $(R^{GG})^2$ with operations on the qudit lattice that encodes the $\mathbf{D}(\mathbf{S}_3)$ quantum double model.

4.4.2 Deriving the R matrix on the $\mathbf{D}(\mathbf{S}_3)$ lattice

Having demonstrated how the braiding of a pair of anyons may be implemented with ribbon operators we now want to show how the abstract diagrams of ribbons in Figure 4.6 may be explicitly realised on a lattice. Consider the ribbons F_ρ^G and $F_{\rho'}^G$ shown in Figure 4.7. In the previous section we have shown how topological invariance allows these ribbons to take any arbitrary homotopically equivalent shape as long as the structure

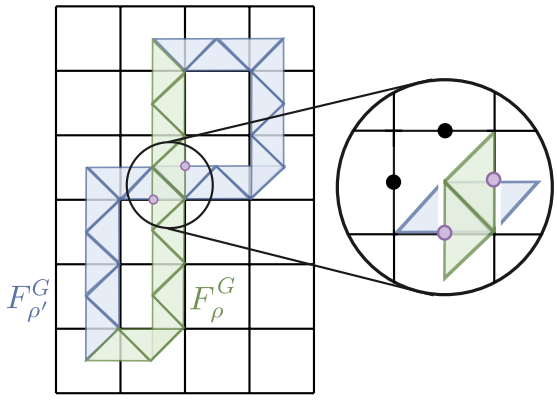

Figure 4.7: Realising the R^{GG} matrix on the quantum double lattice. Following Fig. 4.6 we illustrate a pair of braided G anyon ribbons, F^G_ρ and $F^G_{\rho'}$, with the same start and end points, highlighting the qudits where the ribbons cross. As the two ribbons, F^G_ρ and $F^G_{\rho'}$, cross at two qudits, denoted with purple dots, the effect of the braiding only depends on the action on these qudits. Hence, the elements $(R^{GG}_i)^2$ may be reproduced by the reduced system on just two qudits.

of this overlap, which encodes their braiding information, is preserved. Hence, the commutativity of two arbitrary ribbons reduces down to the commutativity of the operators acting on these two points of overlap. These minimal operators are $F^G_{\rho_1}$ and $F^G_{\rho_2}$ described by (4.25) and (4.26) respectively and forming a crossed joint on the two qudits as shown in Figure 4.8. For this system, Equation (4.33) thus becomes

$$A^i(v)F^G_{\rho_2}F^G_{\rho_1} = (R^{GG}_i)^2 A^i(v)F^G_{\rho_1}F^G_{\rho_2}, \tag{4.34}$$

where $A^i(v), i = A, B, G$, is the vertex projector as defined in (5.7), projecting onto the desired fusion outcome of anyons G_1 and G_2 as in Figure 4.8.

In order to extract the braiding information from these operators we thus introduce two sets of states

$$\begin{aligned} |\phi_{21}(i)\rangle &= N_i A^i(v)F^G_{\rho_2}F^G_{\rho_1}|\zeta\rangle\,, \\ |\phi_{12}(j)\rangle &= N_j A^j(v)F^G_{\rho_1}F^G_{\rho_2}|\zeta\rangle\,, \end{aligned} \tag{4.35}$$

for $i, j = A, B, G$, with normalisation factors $N_A = N_B = 2$ and $N_G = \sqrt{2}$ required due

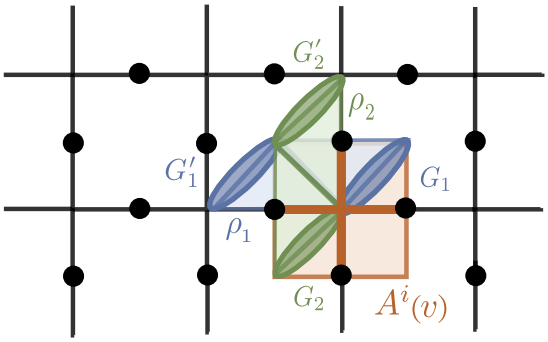

Figure 4.8: The positions of the four G dyons as created by the operators $F^G_{\rho_1}$ and $F^G_{\rho_2}$. Anyons G_1' and G_2' overlap on a plaquette, while G_1 and G_2 overlap on the vertex labelled v. By applying a vertex projector $A^i(v)$, $i = A, B$ or G, the outcome of the fusion $G_1 \times G_2$ can be directly measured.

to the action of the projectors such that $\langle\phi_{21}(i)|\phi_{21}(i')\rangle = \langle\phi_{12}(i)|\phi_{12}(i')\rangle = \delta_{ii'}$. By analogy with Equation (4.34), we thus have

$$|\phi_{21}(i)\rangle = (R_i^{GG})^2\,|\phi_{12}(i)\rangle\,, \tag{4.36}$$

such that the algebraic form of each element $(R^{GG})^i_i \equiv R_i^{GG}$ corresponds to the result of the calculation of the overlap

$$(R_i^{GG})^2 = \langle\phi_{12}(i)|\phi_{21}(i)\rangle. \tag{4.37}$$

By explicit computation of these amplitudes we obtain

$$(R_A^{GG})^2 = (R_B^{GG})^2 = \bar{\omega}, \qquad (R_G^{GG})^2 = \omega, \tag{4.38}$$

demonstrating the exact reconstruction of $(R^{GG})^2$ in the anyonic basis. Hence, by considering only the two segments ρ_1 and ρ_2 of the braiding ribbons ρ and ρ' we are able to determine the braiding matrix of the G anyons squared. In Appendix C.2 we provide an alternative derivation of this result with the evaluation of the operator products $F^G_{\rho_1}F^G_{\rho_2}$ and $F^G_{\rho_2}F^G_{\rho_1}$ in the basis of group elements. With comparison of the elements of the res-

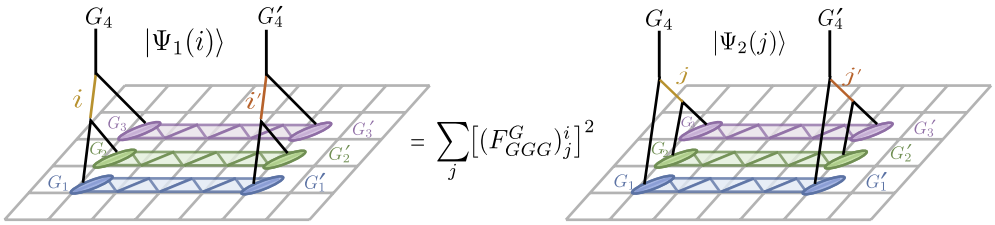

Figure 4.9: Recombination in the fusion order of G anyons, implemented on the $\mathbf{D}(\mathbf{S}_3)$ lattice. We consider three ribbons F^G_k, $k = 1, 2, 3$ that produce pairs of anyons G_k and G'_k at their endpoints. At one side of the ribbons we measure pairs of anyons in order to impose a certain fusion outcome. Each such measurement necessarily projects the anyons at the other endpoint to the same fusion outcome due to superselection rules. As a result the total state of the system produces squared amplitudes $[(F^G_{GGG})^i_j]^2$ during fusion recombination, as seen in Equation (4.43).

ulting matrices, $(R^{GG})^2$ may be derived in the anyonic basis in a method lending itself to the quantum tomographic verification of [148].

4.5 F matrix derivation

We will now determine the fusion recombination matrix, F, illustrated in Figure 3.1(b). Together with the R matrix determined in the previous section, the evaluation of the F matrix will enable us to show their non-commutativity and thus demonstrate the non-Abelian character of the G anyons of $\mathbf{D}(\mathbf{S}_3)$. Here we provide a minimal set of ribbon operators and local projections of the planar code model that can determine each of the matrix elements $(F^G_{GGG})^i_j$.

Surprisingly, the evaluated quantum amplitudes provide the F matrix elements *squared*. This 'doubling' of fusion processes is obtained when considering the action of ribbon operators on a closed system of anyons, where total charge must be conserved. However, we will show that the obtained information is sufficient to explicitly verify that the braiding operator $b_{2,G}$ enables magic state generation in the logical fusion basis.

4.5.1 The doubling of fusion recombination

The matrix F^G_{GGG} describes the change of basis in the Hilbert space of four G anyons corresponding to exchanging the order of fusion of three distinct G anyons, G_1, G_2, G_3 to a fourth composite G_4 anyon. In the notation of Equation (3.2) we have

$$|(G_1, G_2), G_3 \to i, G_3 \to G_4\rangle = \sum_j (F^G_{GGG})^i_j \, |G_1, (G_2, G_3) \to G_1, j \to G_4\rangle \, . \tag{4.39}$$

Equivalently, the orthogonality of distinct fusion channels means that each matrix element $(F^G_{GGG})^i_j$ may be expressed as the overlap

$$(F^G_{GGG})^i_j = \langle G_1, (G_2, G_3) \to G_1, j \to G_4 | (G_1, G_2), G_3 \to i, G_3 \to G_4\rangle. \tag{4.40}$$

To successfully simulate this process on the lattice, we therefore want to develop a methodology that allows for the controlled re-ordering of the fusion of three G anyons and the intermediary composite i or j. Akin to the methodology for the R matrix, the fusion of G anyons is enacted with the application of combinations of ribbons producing pairs of these anyons $(G_n, G'_n), n = 1, 2, 3, 4$ as shown in Figure 4.9. The ordering of fusion is controlled by the application of projective measurements to a chosen pair of anyons. For example, in Fig. 4.9(a) the first measurement is of G_1 and G_2 to fusion outcome i, whereas in Fig. 4.9(b), the creation of j is ensured by the projection onto the fusion of G_2 and G_3. We note that each of our states is constructed from the application of ribbon operators to the vacuum. Superselection therefore dictates that at each stage it must always be possible to fuse the created anyons back to the vacuum. As each of the ribbon operators in the quantum double necessarily create anyons in pairs, we will see that anyonic conservation therefore results in two identical fusion processes occurring simultaneously between two sets of anyons, (G_1, G_2, G_3, G_4) and (G'_1, G'_2, G'_3, G'_4) as shown in Figure 4.9.

To make this analysis explicit, we denote the two sets of identical fusion processes

with the tensor product such that in the anyonic basis we obtain

$$|\Psi_1(i)\rangle = |(G_1, G_2), G_3 \to i, G_3 \to G\rangle \otimes |(G_1', G_2'), G_3' \to i, G_3' \to G\rangle\,, \tag{4.41}$$

and

$$|\Psi_2(j)\rangle = |G_1, (G_2, G_3) \to G_1, j \to G\rangle \otimes |G_1', (G_2', G_3') \to G_1', j \to G\rangle\,. \tag{4.42}$$

It is important to note here, that although the matrix F^G_{GGG} relates two sets of orthonormal basis states as in Equation (3.2), this doubling of fusion processes produced by projection operators is described by the non-unitary matrix with elements $F^i_j = [\big(F^G_{GGG}\big)^i_j]^2$. In order to extract these elements it is therefore necessary to choose one set of states as an orthonormal basis. The set of states created by re-ordering the fusion processes as detailed may then not be orthonormal, but can be expressed as a linear combination of the other set of states. For example, if $|\Psi_2(j)\rangle$ is constructed as the orthonormal basis, then

$$|\Psi_1(i)\rangle = \sum_j [\big(F^G_{GGG}\big)^i_j]^2\, |\Psi_2(j)\rangle\,. \tag{4.43}$$

In this way we obtain

$$\langle\Psi_2(j)|\Psi_1(i)\rangle = \big[(F^G_{GGG})^i_j\big]^2\,, \tag{4.44}$$

where one $(F^G_{GGG})^i_j$ comes from the recombination of the unprimed G anyons and the other from the primed ones. Such a method for reproducing the F matrix using a closed system will therefore necessarily produce the squared value of each element. Below, we will introduce a set of states that explicitly demonstrate these anyonic processes with the quantum double lattice model.

4.5.2 Deriving the F matrix on the $\mathbf{D}(\mathbf{S}_3)$ lattice

Here we introduce a method to explicitly determine the elements

$$F^i_j = \left[\left(F^G_{GGG}\right)^i_j\right]^2, \tag{4.45}$$

of the 'squared' matrix F, by considering operations on the lattice of the $\mathbf{D}(\mathbf{S}_3)$ quantum double model. Our main aim is to determine these matrix elements with the minimal amount of resources. In particular, we use the two qudit ribbons $F^G_{\rho_1}$ and $F^G_{\rho_2}$ defined in (4.25) and (4.26). As these ribbons overlap extra care must be taken to account for possible braiding phase factors, as we shall see in the following. We start by introducing two states

$$\begin{aligned} |\psi_1(i)\rangle &= A^{G_4}(v)F^{G_3}_{\rho_2}A^i(v)F^{G_2}_{\rho_2}F^{G_1}_{\rho_1}|\zeta\rangle\,, \\ |\psi_2(j)\rangle &= A^{G_4}(v)F^{G_1}_{\rho_1}A^j(v)F^{G_3}_{\rho_2}F^{G_2}_{\rho_2}|\zeta\rangle\,, \end{aligned} \tag{4.46}$$

for $i,j = A,B,G$. The subscripts in G_n are provided here to elucidate the link to the process shown in Figure 4.9, but will be dropped in the following when the distinction is not needed. Both states $|\psi_1(i)\rangle$ and $|\psi_2(j)\rangle$ are not normalised due to the application of the projectors $A^i(v)$. Nevertheless, states $|\psi_2(j)\rangle$ are orthogonal so in the following we account explicitly for their normalisation, $\langle\psi_2(j)|\psi_2(j)\rangle$. The states $|\psi_1(i)\rangle$ are not orthogonal to each other, but similar to (4.43) they can be represented as superpositions of $|\psi_2(j)\rangle$ states as

$$|\psi_1(i)\rangle = f_{iA}|\psi_2(A)\rangle + f_{iB}|\psi_2(B)\rangle + f_{iG}|\psi_2(G)\rangle\,. \tag{4.47}$$

As the $|\psi_2(j)\rangle$ are orthogonal we thus have

$$f_{ij} = \frac{\langle\psi_2(j)|\psi_1(i)\rangle}{\langle\psi_2(j)|\psi_2(j)\rangle}. \tag{4.48}$$

Similar to (4.44), the coefficients f_{ij} are related to the elements of the matrix F up to overall phase factors generated due to the crossing of the ρ_1 and ρ_2 ribbons.

In the states $|\psi_1(i)\rangle$ and $|\psi_2(j)\rangle$, the order of fusion is explicitly enforced with the order of application of each of the ribbon operators, $F^G_{\rho_1}$ and $F^G_{\rho_2}$ to the ground state $|\zeta\rangle$. Consider $|\psi_1(i)\rangle$, the initial action of $F^G_{\rho_2}F^G_{\rho_1}$ on the anyonic vacuum $|\zeta\rangle$ produces two pairs of G anyons as illustrated in Figure 4.8. By applying the projector $A^i(v)$ to the vertex v on which two of these anyons from different ribbons overlap, we may ensure the fusion outcome $G_1 \times G_2 \to i$. Superselection also ensures the simultaneous complementary fusion process $G'_1 \times G'_2 \to i$. The second application of $F^G_{\rho_2}$ to this state produces a subsequent pair of fusion processes in which the anyons G_3 and G'_3 fuse with the composite i anyons. The application of the final projector $A^G(v)$ to this vertex ensures that both $G_3 \times i \to G_4$ and $G'_3 \times i \to G'_4$, thus completing the construction of the fusion trees as shown in Figure 4.9. Note that as we require the use of a small system to realise the fusion properties, the ribbon operators used in $|\psi_1(i)\rangle$ and $|\psi_2(j)\rangle$ are crossing each other, giving rise to additional braiding phase factors.

With analytic consideration of the overlaps $\langle\psi_2(j)|\psi_1(i)\rangle$ as shown in Appendix C.3, we find that it is always possible to extract a phase factor $(R^{Gj}_G)^2$ due to the braiding of the worldlines of the j and G_3 anyons in $|\psi_2(j)\rangle$. In particular, we have

$$\langle\psi_2(j)|\psi_1(i)\rangle = (R^{Gj}_G)^2 \langle\zeta| F^G_{\rho_1}F^j_{\rho_2}A^G(v)F^G_{\rho_2}A^i(v)F^G_{\rho_2}F^G_{\rho_1}|\zeta\rangle . \tag{4.49}$$

We therefore find that, by using (4.46) and (4.47), the fusion matrix elements squared may be calculated from

$$F^i_j = \overline{(R^{Gj}_G)^2} f_{ij}, \tag{4.50}$$

where the phases

$$(R^{GA}_G)^2 = (R^{GB}_G)^2 = 1, \quad (R^{GG}_G)^2 = \omega. \tag{4.51}$$

Calculation of these overlaps thus yields the 'squared' F matrix

$$\mathcal{F} = \frac{1}{4}\begin{pmatrix} 1 & 1 & 2 \\ 1 & 1 & 2 \\ 2 & 2 & 0 \end{pmatrix}. \tag{4.52}$$

This result is in agreement with the F-matrix of the G anyons of $\mathbf{D}(\mathbf{S}_3)$ given in (4.14), as determined from the pentagon equations. As this matrix is real and positive the values of the F matrix elements can be derived up to a sign ambiguity, due to the doubling of the fusion processes when ribbons are employed in the fusion recombination, as described in Fig. 4.9. In the following we show that the non-Clifford action of the braiding matrix $B_{2,G}$ can be demonstrated without the need to determine the value of these signs.

4.6 Non-Clifford action of $B_{2,G}$

In the previous we employed manipulations on the lattice of the $\mathbf{D}(\mathbf{S}_3)$ quantum double model to determine the elements of the fusion matrix, F. As the method we employed gives rise to squares of the elements, $\mathcal{F}^i_j = \left[\left(F^G_{GGG}\right)^i_j\right]^2$, a sign ambiguity arises in determining the elements of F^G_{GGG} when extracted from $\mathcal{F}$. It is possible however, to unequivocally show that for any valid combination of signs, the corresponding braiding matrix always encodes a logical non-Clifford gate capable of producing magic states, which is the goal of this investigation.

To proceed we consider all matrices $\widetilde{F}^G_{GGG}$ that satisfy

$$\mathcal{F}^i_j = \left[\left(\widetilde{F}^G_{GGG}\right)^i_j\right]^2. \tag{4.53}$$

Accounting for sign ambiguity, this set of matrices may be parametrised as

$$\left\{\widetilde{F}^{G}_{GGG}\right\} = \left\{ \frac{1}{2} \begin{pmatrix} \alpha & \beta & \gamma\sqrt{2} \\ \delta & \epsilon & \zeta\sqrt{2} \\ \eta\sqrt{2} & \kappa\sqrt{2} & 0 \end{pmatrix}, \alpha, \beta, \ldots, \eta, \kappa = \pm 1 \right\}, \tag{4.54}$$

where the additional restraint of unitarity reduces the number of valid solutions to sixty-four matrices. Utilising the extracted form of $(R^{GG})^2$ and Eq. (4.18), a braiding matrix $\widetilde{B}_{2,G} = \widetilde{F}^{G\,-1}_{GGG}(R^{GG})^2\widetilde{F}^{G}_{GGG}$ may be computed for each such solution. Even with this sign ambiguity, all resulting braiding operations can be expressed as

$$\widetilde{B}_{2,G} = \begin{pmatrix} \cos\left(\frac{2\pi}{3}\right) & \pm i\sin\left(\frac{2\pi}{3}\right) & 0 \\ \pm i\sin\left(\frac{2\pi}{3}\right) & \cos\left(\frac{2\pi}{3}\right) & 0 \\ 0 & 0 & \bar{\omega} \end{pmatrix}, \tag{4.55}$$

explicitly verifying the non-Clifford action of this braiding on the reduced fusion subspace $\mathrm{span}(|A\rangle, |B\rangle)$. Additionally, the action of this operator on the intermediate vacuum fusion state yields two possible states,

$$|\psi_{\pm}\rangle = \widetilde{B}_{2,G}\,|A\rangle = \cos\left(\frac{2\pi}{3}\right)|A\rangle \pm i\sin\left(\frac{2\pi}{3}\right)|B\rangle\,, \tag{4.56}$$

each with stabilizer Renyi entropy $M_2(\psi_{\pm}) = \log\left(\frac{16}{13}\right)$. In this way, the simple lattice protocol presented in this chapter, provides an explicit demonstration of the realisation of valuable magic states through the braiding of non-Abelian G anyons.

4.7 Conclusions

This work represents an important step towards the realisation of robust universal quantum computation within the framework of topological systems. In particular, through the controlled application of operations on a lattice of $d = 6$ qudits, we have provided a direct demonstration of the non-Clifford action arising from the braiding of non-Abelian

anyons within the $\mathbf{D}(\mathbf{S}_3)$ quantum double model. In contrast to Abelian anyons, whose braiding operations are restricted to the Clifford group, these braiding operators are thus shown to enable the preparation of magic states, a key resource in schemes for universal quantum computation. Demonstrating this capability within the exactly solvable setting of the quantum double thus represents an important advance in bridging the gap between the abstract algebraic description of non-Abelian braiding statistics and the concrete protocols required to harness them in potential physical implementations.

For this task, we considered the $\mathbf{D}(\mathbf{S}_3)$ quantum double model, which supports the closed anyonic subgroup $\{A, B, G\}$, with G being the non-Abelian anyon. This model can be encoded on a square lattice of $d = 6$ qudits. While generating and manipulating G anyons in this model typically requires a lattice of several qudits and controlled operations between them [147, 154], we have shown that by carefully investigating the braiding and fusion properties of the G anyons, this information can be decoded from static combinations of the ribbons that generate them using simple projective measurements.

It is an important, but often overlooked feature of the quantum double model, that the structure of the underlying topological order is encoded in the commutation relations of overlapping ribbon operators. This result has been well-studied in the Abelian case, whereby the non-trivial exchange factor for the e and m anyons of the toric code may be extracted from the commutation properties of the Pauli algebra on a single qubit [176]. The generalization of this result is however less obvious for non-Abelian anyons, the braiding of which induces different phases dependent on the total fusion channel. Building on foundational work by Goel et al. [148], we present a resolution to this issue through the use of charge projection operators $A^i(v)$, adapted from [173]. For the reduced anyon subgroup $\{A, B, G\}$ these projectors form an orthogonal set, capable of uniquely distinguishing between each anyon without the need for additional flux measurements. With these operators, we may not only reproduce $(R^{GG})^2$, using $A^i(v)$ to explicitly project onto each total fusion channel from pairs of overlapping ribbon operators, but also create states on the lattice mirroring the anyonic basis states $|(G, G), G \to i, G \to G\rangle$,

where $A^i(v)$ specifies the intermediate fusion outcome. By taking the overlap of such states we may therefore also simulate the action of the matrix F^G_{GGG}, required to generate the forms of braiding operators between anyons not sharing a direct fusion channel. Interestingly, it is found that this construction necessarily produces the elements of the F matrix squared, an apparent fundamental restriction on such a closed system of anyons where charge must be conserved.

Furthermore, by carefully selecting ribbon operators such that the charge component of one of the pair of G anyons created lies on the vertex v, our protocol only requires a projection operator on a single site $A^i(v)$. This reduction is especially important when considering the experimental implementation of such approaches, where the probabilistic nature of measurements naturally requires a post-selection process repeated over a large number of trials. In the next chapter, the experimental realisation of this scheme will be explored further. By introducing a dense encoding strategy based on the minimal physical system of a single plaquette, we show that the generation of magic states can be demonstrated using operations on only two qutrits, making the protocol directly compatible with linear optical architectures. The work presented here thus provides a blueprint for the explicit demonstration of non-Clifford braiding statistics on near-term quantum devices.

Chapter 5

Fault-tolerant photonic operations via $D(S_3)$ anyonic encoding

5.1 Introduction

In Chapter 4, we presented a protocol for the realisation of non-Abelian braiding statistics for the G anyons of the $\mathbf{D}(\mathbf{S}_3)$ quantum double model. Practically, the physical realisation of the quantum double model $\mathbf{D}(\mathbf{G})$ requires the manipulation of a lattice of $d = |\mathbf{G}|$ qudits. Even for the smallest non-Abelian group $\mathbf{S}_3$, implementation of the $\mathbf{D}(\mathbf{S}_3)$ quantum double model thus still, in principle, requires the realisation of a lattice composed of 6-dimensional qudits, a structure which is unlikely to occur naturally in a physical system. A more accessible approach, explored in the work of Chen et al. [154] among others [172, 146] arises from the following decomposition of the group elements of $\mathbf{S}_3$

$$\mathbf{S}_3 = \{c^i t^j, \;\; i = 1, 2, 3, j = 1, 2\}. \tag{5.1}$$

This semi-direct product structure $\mathbf{S}_3 \cong \mathbf{Z}_3 \rtimes \mathbf{Z}_2$ allows each 6-dimensional qudit in the $\mathbf{D}(\mathbf{S}_3)$ quantum double model to be encoded as the tensor product of an entangled qutrit-qubit pair. Such an approach has enabled proposals for the efficient preparation of the ground state of the $\mathbf{D}(\mathbf{S}_3)$ quantum double on near-term quantum devices [181, 182, 183].

In this chapter we expand on these established encoding schemes to further reduce the complexity of the minimal system required to implement the protocol introduced in the previous chapter. Analysis of the operator structure in fact reveals that all non-trivial action of the ribbon and projection operators for the $\{A, B, G\}$ sub-model is encoded in their action on the effective qutrit basis $\mathbf{Z}_3 \cong \{e, c, c^2\}$. In this way, we demonstrate that the elements of the squared R and F matrices may be exactly reconstructed through the expectation values of operations on just two qutrits, an invaluable simplification for not only the experimental verification of non-Abelian braiding statistics, but also enabling scaleability in the realisation of multiple logical anyonic states within a larger lattice. In particular, the encoding of the logical qutrit states corresponding to the fusion space of four non-Abelian G anyons in this minimal physical realisation, provides an important blueprint for the implementation of logical entangling gates and prototype topological quantum algorithms [184, 185, 186].

The success of quantum double models in simulating anyonic behavior has naturally motivated efforts towards their physical realisation. Among the proposed platforms, photonic systems have emerged as a particularly promising candidate, offering high coherence, low noise, and flexible access to high-dimensional Hilbert spaces through spatial, temporal, or polarization degrees of freedom [187]. Indeed, recent advances in photonic quantum technologies have established linear optics as a powerful testbed for simulating quantum many-body dynamics and implementing small-scale quantum processors [188, 189, 190]. By combining linear optical elements with ancillary modes and post-selection, a broad class of unitaries and effective non-linear operations can be implemented [191, 192], making photonic architectures especially suitable for simulating models with non-Abelian excitations. Proof-of-principle experiments have already demonstrated the simulation of both Abelian and small-scale non-Abelian anyons using photonic systems [193, 148, 109], reproducing key features such as topological entanglement [194] and braiding-induced phase shifts [195, 196, 197, 110]. Notably, recent work by Goel et al. [148] employed a single qutrit, encoded in the transverse spatial mode of light, to

experimentally demonstrate the non-Abelian fusion rules of the $\mathbf{D}(\mathbf{S}_3)$ quantum double model.

In this work, we provide explicit forms of the minimal components required to faithfully encode the $\mathbf{D}(\mathbf{S}_3)$ quantum double within a photonic quantum computing architecture. Leveraging the natural suitability of photonic systems for qudit representations, we develop a protocol for the realisation of the densely encoded scheme on two qutrits, each encoded by a single photon in three spatial modes. Importantly, this multi-photon realisation preserves the tensor product structure of the lattice model, enabling a more direct physical mapping between theory and experiment. We implement key non-Abelian operations such as ribbon operators, braiding transformations, and projection measurements, using a combination of unitary dilation, post-selection, and measurement-induced nonlinearities. Notably, the photonic platform facilitates the direct realisation of the inherently non-unitary $\mathbf{D}(\mathbf{S}_3)$ ribbon operations [153, 109, 198].

With analysis of the performance of this encoded anyonic system with the introduction of decoherent errors, we observe an intrinsic robustness of these anyonic manipulations against physically relevant noise processes, including dephasing and mode mismatch. This fascinating result, which has no direct analogue in conventional topological protection, highlights the specialist suitability of our anyonic encoding for implementation across a range of physical platforms. We quantify this resilience and identify an error threshold below which anyonic encoding offers a clear advantage over conventional gate-based photonic operations, with relatively small overhead. Beyond the photonic realisation, our investigation provides a blueprint for implementing non-Abelian anyonic manipulations across other quantum platforms with readily available quantum devices.

The rest of this chapter is organised as follows. In Section 5.2 we begin with an overview of our protocol for reproducing the R and F matrices on a single plaquette of four $d = 6$ qudits, the smallest physical system on which the Kitaev Hamiltonian may be defined to obtain a unique vacuum ground state and coherent anyonic excitations. In Section 5.3 we further analyse the structure of this ground state and all relevant ribbon

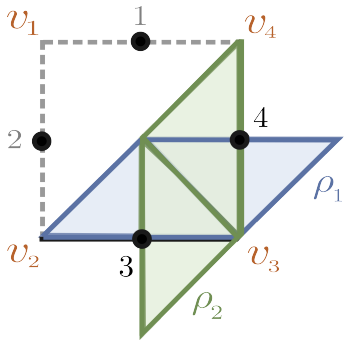

Figure 5.1: The Kitaev Hamiltonian (5.2) defined on a single plaquette with open boundary conditions. In this system, both the ribbon operators $F^G_{\rho_1}$ and $F^G_{\rho_2}$ and projector $A^i(v_3)$ have non-trivial action on only qudits 3 and 4, facilitating a dense encoding of the lattice reconstruction of the R and F matrices.

and projection operators, demonstrating how the non-Abelian braiding statistics they manifest, are in fact encoded in their reduced action on just two qutrits. The significant reduction in complexity facilitated by this dense encoding scheme enables the proposed implementation of our protocol on operational and near-term experimental platforms. In particular, in Section 5.4 we present an experimentally accessible realisation on a linear interferometer optical quantum computer developed in collaboration with Matthew Horner. In Section 5.5, we consider the performance of our encoded model with the introduction of physical noise processes relevant to this photonics architecture. Notably, we observe an apparent robustness (and in certain cases *immunity*) against different forms of decoherent error, that lies outside of the typical paradigm of the topological protection inherent to such anyons. Finally, in Section 5.6, we provide concluding remarks and outlook.

5.2 Minimal $\mathbf{D(S_3)}$ Quantum Double Model

The results derived in the previous chapter considered the application of ribbon and projection operators to a square lattice of arbitrary size. Without loss of generality, we therefore consider the minimal physical system of a single plaquette, p, composed of four $d = 6$ qudits, as shown in Figure 5.1. For open boundary conditions, the Hamiltonian of

this system is given by

$$\mathcal{H}_4 = -B(p) - \sum_{i=1}^{4} A(v_i), \tag{5.2}$$

where the vertex operators, $A(v_i)$, each act non-trivially on two qudits only. These reduced vertex projection operators act as boundary terms in the Hamiltonian (5.2). For this system, the choice of boundary conditions ensure that $\mathcal{H}_4$ has a unique ground state, $|\eta\rangle$, that has support on all four qudits.

As previously, pairs of G anyons may be coherently created as excitations of the lattice using the ribbon operators $F^G_{\rho_1}$ and $F^G_{\rho_2}$. For the reduced system, these ribbon operators have the following representations: $F^G_{\rho_1} = \mathbf{1}_6 \otimes \mathbf{1}_6 \otimes f^G_{\rho_1}$ with the two-qudit component

$$f^G_{\rho_1} = (T^e_- + \omega T^c_- + \bar{\omega} T^{c^2}_-) \otimes L^c_- + (T^e_- + \bar{\omega} T^c_- + \omega T^{c^2}_-) \otimes L^{c^2}_-, \tag{5.3}$$

and $F^G_{\rho_2} = \mathbf{1}_6 \otimes \mathbf{1}_6 \otimes f^G_{\rho_2}$ with

$$f^G_{\rho_2} = L^c_+ \otimes (T^e_- + \omega T^c_- + \bar{\omega} T^{c^2}_-) + L^{c^2}_+ \otimes (T^e_- + \bar{\omega} T^c_- + \omega T^{c^2}_-), \tag{5.4}$$

where we have ordered the qudits $1, 2, 3$ and 4 as shown in Fig. 5.1. For each ribbon operator, the charge component of one of the pair of anyonic excitations lies on the vertex v_3. These overlapping anyons form the basis for the static braiding protocol as introduced in Chapter 4. In order to distinguish between the anyonic excitations created at this vertex, we therefore provide an explicit representation of the relevant local charge projection operator. The local gauge transformations on this vertex become

$$A^g(v_3) = \mathbf{1}_6 \otimes \mathbf{1}_6 \otimes L^g_+ \otimes L^g_-, \tag{5.5}$$

and form the basis of the anyonic vertex projectors. For the Abelian anyons A and B we

have

$$A^A(v_3) = \frac{1}{6}\Big(A^e(v_3) + A^c(v_3) + A^{c^2}(v_3) + A^t(v_3) + A^{tc}(v_3) + A^{tc^2}(v_3)\Big), \tag{5.6}$$

$$A^B(v_3) = \frac{1}{6}\Big(A^e(v_3) + A^c(v_3) + A^{c^2}(v_3) - A^t(v_3) - A^{tc}(v_3) - A^{tc^2}(v_3)\Big), \tag{5.7}$$

while the G charge projector has the form

$$A^G(v_3) = \frac{1}{3}\Big(2A^e(v_3) - A^c(v_3) - A^{c^2}(v_3)\Big), \tag{5.8}$$

$$= \mathbf{1}_6 \otimes \mathbf{1}_6 \otimes a^G(v_3), \tag{5.9}$$

with two qudit action

$$a^G(v_3) = \frac{1}{3}(2 \cdot \mathbf{1}_{36} - L^c_+ \otimes L^c_- - L^{c^2}_+ \otimes L^{c^2}_-). \tag{5.10}$$

In Equations (4.37) and (4.50) we have shown that the derivation of the forms of both the R and F matrices can be expressed in terms of the overlap between the generalised states $|\phi_{12}(i)\rangle$ & $|\phi_{21}(j)\rangle$ and $|\psi_1(i)\rangle$ & $|\psi_2(j)\rangle$, respectively. For the case of a single plaquette system the states $|\phi_{12}(i)\rangle$ and $|\phi_{21}(j)\rangle$ are given by

$$\begin{aligned} |\phi_{12}(i)\rangle &= N_i A^i(v_3) F^G_{\rho_1} F^G_{\rho_2} |\eta\rangle\,, \\ |\phi_{21}(j)\rangle &= N_j A^j(v_3) F^G_{\rho_2} F^G_{\rho_1} |\eta\rangle\,, \end{aligned} \tag{5.11}$$

such that

$$(R^{GG}_i)^2 = \langle \phi_{12}(i) | \phi_{21}(i) \rangle. \tag{5.12}$$

Similarly, $|\psi_1(i)\rangle$ and $|\psi_2(j)\rangle$ become

$$\begin{aligned} |\psi_1(i)\rangle &= A^G(v_3) F^G_{\rho_2} A^i(v_3) F^G_{\rho_2} F^G_{\rho_1} |\eta\rangle\,, \\ |\psi_2(j)\rangle &= A^G(v_3) F^G_{\rho_1} A^j(v_3) F^G_{\rho_2} F^G_{\rho_2} |\eta\rangle\,. \end{aligned} \tag{5.13}$$

yielding

$$\left[(F^G_{GGG})^i_j\right]^2 = \overline{(R^{Gj}_G)}^2 \frac{\langle\psi_2(j)|\psi_1(i)\rangle}{\langle\psi_2(j)|\psi_2(j)\rangle}. \tag{5.14}$$

By consideration of the operators $A^i(v_3), F^G_{\rho_1}$ and $F^G_{\rho_2}$, as defined explicitly for a single plaquette, we observe that all such operations only have non-trivial action on qudits 3 and 4 of p. In the next section, we will demonstrate how this property, alongside careful analysis of the structure of the entangled ground state $|\eta\rangle$, allows for the values of the amplitudes in (5.12) and (5.14) to be computed from the overlaps of states on just two qutrits. This significant reduction in the resources required to physically implement our protocol will enable the photonic realisation proposed in Section 5.4.

5.3 Dense Encoding

The elements of the braiding and fusion matrices of the G non-Abelian anyons, as given by (5.12) and (5.14), can be extracted from a single plaquette with four $d = 6$ qudits, as shown in Fig. 5.1. For this minimal system the quantum double Hamiltonian has a unique ground state corresponding to the anyonic vacuum on which anyons can be coherently created and manipulated. In this Section we show that with careful analysis of both the ground state and operator structure a series of simplifications can be obtained. First, we show that we can obtain the information of (5.12) and (5.14) from considering only two qudits on which the relevant operators act non-trivially. Second, taking advantage of the structure of the $\mathbf{S}_3$ group it is possible to employ two $d = 3$ qutrits instead of two $d = 6$ qudits. Finally, we show that the desired information from the expectation values of operations on two qutrits can be obtained from product states, in a process equivalent to performing a full operator tomography.

In Section 4.5 of the previous chapter, it was shown that the controlled application of ribbon and projection operators may be used to create tensor products of the anyonic basis states $\{|i = A, B, G\rangle\} \equiv \{|(G_1, G_2), G_3 \to i, G_3 \to G_4\rangle\}$ between two sets of four G anyons. The resulting topologically protected fusion space realises a logical qutrit

on which one may theoretically perform computation through braiding and fusion. The encoding of these logical qutrits within the smallest physical instance presented in this section therefore not only renders this protocol more accessible to current and near-term experimental platforms, but also facilitates scaleability for the implementation of logical entangling gates and prototype quantum algorithms between multiple such qutrits.

For clarity, the convention for the labelling of operations on different Hilbert space dimensionalities are listed in Table 5.1.

Hilbert space	Operator notation	Examples
$(\mathbb{C}^6)^{\otimes 4}$	O	$F^G_{\rho_1}, A^A(v_3), \ldots$
$(\mathbb{C}^6)^{\otimes 2}$	o	$f^G_{\rho_1}, a^A(v_3), \ldots$
$(\mathbb{C}^3)^{\otimes 2}$	$\mathcal{O}$	$\mathcal{F}^G_{\rho_1}, \mathcal{A}^+(v_3), \ldots$

Table 5.1: Notation conventions for operators with support on different Hilbert spaces.

5.3.1 From 4 qudits to 2 qudits

We start by noting that all ribbon and projector operators in (5.11) and (5.13) only act non-trivially on qudits 3 and 4 of the single plaquette, i.e. they are of the form

$$O = \mathbf{1}_{36} \otimes o, \tag{5.15}$$

where $\mathbf{1}_{36}$ is the identity acting on qudits 1 and 2 and o acts on qudits 3 and 4. The calculation of all overlaps used to derive the elements of R^{GG} and F^G_{GGG} can therefore be written as

$$\langle\eta| O |\eta\rangle = \langle\eta| (\mathbf{1}_{36} \otimes o) |\eta\rangle = \langle\eta| \begin{pmatrix} o & 0 & \ldots & 0 \\ 0 & o & \ldots & 0 \\ \vdots & \vdots & \ddots & \vdots \\ 0 & 0 & \ldots & o \end{pmatrix} |\eta\rangle . \tag{5.16}$$

Each element 'o' is itself a 36×36 matrix, such that this expression may be further simplified by decomposing $|\eta\rangle$ into a set of 36-dimensional vectors. It is found that $|\eta\rangle$

may be written in the following form

$$|\eta\rangle = \begin{pmatrix} |\psi_1\rangle \\ |\psi_2\rangle \\ |\psi_3\rangle \\ |\psi_4\rangle \\ |\psi_5\rangle \\ |\psi_6\rangle \end{pmatrix} = \begin{pmatrix} |\psi_1\rangle \\ (L_-^c \otimes \mathbf{1}_{36}) |\psi_1\rangle \\ (L_-^{c^2} \otimes \mathbf{1}_{36}) |\psi_1\rangle \\ (L_-^t \otimes \mathbf{1}_{36}) |\psi_1\rangle \\ (L_-^{tc} \otimes \mathbf{1}_{36}) |\psi_1\rangle \\ (L_-^{tc^2} \otimes \mathbf{1}_{36}) |\psi_1\rangle \end{pmatrix}, \tag{5.17}$$

where $|\psi_1\rangle$ is a 6^3-dimensional vector of the form

$$|\psi_1\rangle = \begin{pmatrix} |\psi_e\rangle \\ |\psi_c\rangle \\ |\psi_{c^2}\rangle \\ |\psi_t\rangle \\ |\psi_{tc}\rangle \\ |\psi_{tc^2}\rangle \end{pmatrix}, \quad |\psi_g\rangle = \frac{1}{\sqrt{216}} \sum_{\substack{g_1 g_2 = g \\ g_1, g_2 \in \mathbf{S}_3}} |g_1, g_2\rangle \,. \tag{5.18}$$

These $|\psi_g\rangle$ are the 36-dimensional vectors on which each operator o will act. The single-qudit right multiplication operators L_-^g are essentially permutation operators such that, for example

$$|\psi_2\rangle = (L_-^c \otimes \mathbf{1}_{36}) |\psi_1\rangle = \begin{pmatrix} |\psi_c\rangle \\ |\psi_{c^2}\rangle \\ |\psi_e\rangle \\ |\psi_{tc}\rangle \\ |\psi_{tc^2}\rangle \\ |\psi_t\rangle \end{pmatrix}. \tag{5.19}$$

We therefore see that each 36-dimensional vector $|\psi_g\rangle$ will appear in each of $|\psi_1\rangle, |\psi_2\rangle, \ldots, |\psi_6\rangle$ once and therefore in total in $|\eta\rangle$ six times. Hence, all ground state expectation values of operators acting only non-trivially on qudits 3 and 4 may be decomposed as the sum

of six inner products within this reduced system

$$\langle\eta|\left(\mathbf{1}_{36}\otimes o\right)|\eta\rangle = 6\sum_{g\in\mathbf{S}_3}\langle\psi_g|\, o\,|\psi_g\rangle\,. \tag{5.20}$$

In this way, all ground state expectation values of the form $\langle\eta|\left(\mathbf{1}_{36}\otimes o\right)|\eta\rangle$ may be exactly computed from their non-trivial action on the set of entangled two qudit states $\{|\psi_g\rangle\,, g\in\mathbf{S}_3\}$.

5.3.2 From 2 qudits to 2 qutrits

The group $\mathbf{S}_3$ has the semi-direct product structure $\mathbf{S}_3\cong\mathbf{Z}_3\rtimes\mathbf{Z}_2$ [145]. This feature is employed in existing proposals for the physical realisation of the quantum double $\mathbf{D}(\mathbf{S}_3)$, whereby each $d=6$ qudit may be embedded into an entangled qubit-qutrit pair on each site. Here, this structure informs an approach in which an effective basis transformation yields a natural splitting between basis states $\{e,c,c^2\}$ and $\{t,tc,tc^2\}$, allowing us to consider only the action of our operators on the reduced qutrit subspace $\mathbf{Z}_3\cong\{e,c,c^2\}$, thus significantly reducing the required resources.

Consider the state construction for the determination of the elements of the matrix $(R^{GG})^2$,

$$\begin{aligned}|\phi_{12}(i)\rangle &= N_i A^i(v_3) F^G_{\rho_1} F^G_{\rho_2}\,|\eta\rangle\,,\\ |\phi_{21}(j)\rangle &= N_j A^j(v_3) F^G_{\rho_2} F^G_{\rho_1}\,|\eta\rangle\,.\end{aligned} \tag{5.21}$$

The sets of states $\{|\phi_{12}(i)\rangle\}$, $\{|\phi_{21}(j)\rangle\}$ each form orthonormal bases related by the braiding relation

$$\left([R^{GG}]^i_j\right)^2 = \langle\phi_{12}(j)|\phi_{21}(i)\rangle,\qquad i,j=A,B,G. \tag{5.22}$$

We now introduce the state $|\phi_{12}(+)\rangle\equiv\frac{1}{\sqrt{2}}(|\phi_{12}(A)\rangle+|\phi_{12}(B)\rangle)$ which may equival-

ently be written as

$$|\phi_{12}(+)\rangle = N_+ A^+(v_3) F^G_{\rho_1} F^G_{\rho_2} |\eta\rangle \tag{5.23}$$

where the positive 'combined' vertex projection operator $A^+(v_3)$ is given by

$$A^+(v_3) = \frac{1}{\sqrt{2}}(A^A(v_3) + A^B(v_3)), \tag{5.24}$$

and $N_+ = N_A = N_B$. We may similarly define $|\phi_{12}(-)\rangle, |\phi_{21}(-)\rangle$ with the negative combined projection operator $A^-(v_3) = \frac{1}{\sqrt{2}}(A^A(v_3) - A^B(v_3))$. This new set of projection operators with $i \in \{+, -, G\}$ form an orthogonal projective set as in (4.30) and by definition both sets $\{|\phi_{12}(i)\rangle\}$ and $\{|\phi_{21}(j)\rangle\}$ with $i, j = +, -, G$ form alternative orthonormal bases. Importantly, replacing $A^A(v_3)$ and $A^B(v_3)$ with the combined vertex operator $A^+(v_3)$ allows all operators to be written as summations of terms of the form $(A \oplus B) \otimes (C \oplus D)$. Here '$\oplus$' is the matrix direct sum such that for matrices A and B, $A \oplus B = \text{diag}\{A, B\}$. Explicitly, using the qutrit generalisation of the Pauli operators [199]

$$X = \begin{pmatrix} 0 & 0 & 1 \\ 1 & 0 & 0 \\ 0 & 1 & 0 \end{pmatrix}, \quad Z = \begin{pmatrix} 1 & 0 & 0 \\ 0 & \omega & 0 \\ 0 & 0 & \bar{\omega} \end{pmatrix}, \tag{5.25}$$

we have

$$\begin{aligned} f^G_{\rho_1} &= (Z \oplus \mathbf{0}_3) \otimes (X \oplus X) + (Z^2 \oplus \mathbf{0}_3) \otimes (X^2 \oplus X^2), \\ f^G_{\rho_2} &= (X \oplus X^2) \otimes (Z^2 \oplus \mathbf{0}_3) + (X^2 \oplus X) \otimes (Z \oplus \mathbf{0}_3), \\ a^+(v_3) &= \frac{1}{3}[(\mathbf{1}_3 \oplus \mathbf{1}_3) \otimes (\mathbf{1}_3 \oplus \mathbf{1}_3) + (X \oplus X^2) \otimes (X^2 \oplus X^2) + (X^2 \oplus X) \otimes (X \oplus X)], \\ a^G(v_3) &= \frac{1}{3}[2(\mathbf{1}_3 \oplus \mathbf{1}_3) \otimes (\mathbf{1}_3 \oplus \mathbf{1}_3) - (X \oplus X^2) \otimes (X^2 \oplus X^2) - (X^2 \oplus X) \otimes (X \oplus X)]. \end{aligned} \tag{5.26}$$

In each such product $A \oplus B$, the qutrit operator A acts on the subspace $\{e, c, c^2\}$ while

B acts on the $\{t, tc, tc^2\}$ subspace. This acts as a natural parallel to quantum optics in which the Hilbert space is built up as a direct sum of optical modes. Considering the identity

$$[(A \oplus B) \otimes (C \oplus D)][(E \oplus F) \otimes (G \oplus H)] = (AE \oplus BF) \otimes (CG \oplus DH),$$

we observe that any operations containing products of $f^G_{\rho_1}$ and $f^G_{\rho_2}$ become linear combinations of terms of the form $(A \oplus \mathbf{0}) \otimes (C \oplus \mathbf{0})$. Taking the overlaps of the form (5.20) for such terms results in a natural cancellation of the $\{t, tc, tc^2\}$ subspace

$$\begin{aligned} &\sum_{g\in\mathbf{S}_3}\Big(\sum_{\substack{g_1g_2=g\\ g_1,g_2\in\mathbf{S}_3}}\langle g_1,g_2|\Big)(A\oplus\mathbf{0})\otimes(C\oplus\mathbf{0})\Big(\sum_{\substack{g_3g_4=g\\ g_3,g_4\in\mathbf{S}_3}}|g_3,g_4\rangle\Big)\\ &\quad=\sum_{g\in\{e,c,c^2\}}\Big(\sum_{\substack{g_1g_2=g\\ g_1,g_2\in\mathbf{S}_3}}\langle g_1,g_2|\Big)(A\otimes C)\Big(\sum_{\substack{g_3g_4=g\\ g_3,g_4\in\mathbf{S}_3}}|g_3,g_4\rangle\Big), \end{aligned} \tag{5.27}$$

such that

$$\sum_{g\in\mathbf{S}_3}\langle\psi_g|\,(A\oplus\mathbf{0})\otimes(C\oplus\mathbf{0})\,|\psi_g\rangle=\frac{1}{72}\sum_{g\in\{e,c,c^2\}}\langle\widetilde{\psi}_g|\,(A\oplus\mathbf{0})\otimes(C\oplus\mathbf{0})\,|\widetilde{\psi}_g\rangle\,, \tag{5.28}$$

where

$$|\widetilde{\psi}_g\rangle=\frac{1}{\sqrt{3}}\sum_{\substack{g_1g_2=g\\ g_1,g_2\in\{e,c,c^2\}}}|g_1,g_2\rangle\,. \tag{5.29}$$

In this way all expectation values $\langle\phi_{12}(j)|\phi_{21}(i)\rangle$, $\langle\psi_2(j)|\psi_{1/2}(i)\rangle$ with $i,j=+,G$ can be computed from the reduced operations

$$\mathcal{F}^G_{\rho_1}=Z\otimes X+Z^2\otimes X^2, \tag{5.30}$$

$$\mathcal{F}^G_{\rho_2}=X\otimes Z^2+X^2\otimes Z, \tag{5.31}$$

$$\mathcal{A}^+(v_3)=\frac{1}{3\sqrt{2}}[\mathbf{1}_9+X\otimes X^2+X^2\otimes X], \tag{5.32}$$

$$\mathcal{A}^G(v_3)=\frac{1}{3}[2\cdot\mathbf{1}_9-X\otimes X^2-X^2\otimes X], \tag{5.33}$$

extracted from the components of (5.26) on the $\{e, c, c^2\}$ component of each qudit. Although the overlaps with '$-$' states cannot be determined using qutrits, in Appendix D.1 we show how the structure of these states allows their overlaps with other states to be extracted analytically, enabling the determination of all values $([R^{GG}]^i_j)^2$ and $([F^G_{GGG}]^i_j)^2$ with an encoding on two qutrits.

5.3.3 Simplification of expectation values

Finally, we demonstrate that the expectation value of the operators $\mathcal{O}$ involved in the braiding and fusion processes can be determined by using simple product states directly accessible in the laboratory, rather than the more complex entangled states $|\psi_g\rangle$ given in (5.18). To proceed we write the matrix elements of a general two-qutrit operator $\mathcal{O}$ as

$$\mathcal{O} = \sum_{\substack{g_1 g_2 = g_3 g_4 \\ g_1,g_2,g_3,g_4 \in \{e,c,c^2\}}} p_{g_1 g_2 g_3 g_4} \left|g_1, g_2\right\rangle \left\langle g_3, g_4\right| + \sum_{\substack{g_1 g_2 \neq g_3 g_4 \\ g_1,g_2,g_3,g_4 \in \{e,c,c^2\}}} q_{g_1 g_2 g_3 g_4} \left|g_1, g_2\right\rangle \left\langle g_3, g_4\right|. \tag{5.34}$$

In (5.34) we differentiate between the flux conserving and non-conserving elements, $p_{g_1 g_2 g_3 g_4}$ and $q_{g_1 g_2 g_3 g_4}$, respectively. The states $|\psi_g\rangle$ correspond to a certain flux g. The expectation value of any two-qutrit operator $\mathcal{O}$ with respect to this set of states therefore naturally reduces to the summation over flux-conserving terms

$$\sum_{g \in \{e,c,c^2\}} \langle \widetilde{\psi}_g | \, \mathcal{O} \, | \widetilde{\psi}_g \rangle = \frac{1}{3} \sum_{\substack{g_1 g_2 = g_3 g_4 \\ g_1,g_2,g_3,g_4 \in \{e,c,c^2\}}} p_{g_1 g_2 g_3 g_4}. \tag{5.35}$$

Hence, the braiding and fusion elements we want to extract can be obtained in terms of all the flux conserving elements $p_{g_1 g_2 g_3 g_4}$.

Although the expectation value with respect to summation over the two-qutrit state $|\psi_g\rangle$ represents a significant simplification from the full anyonic vacuum ground state $|\eta\rangle$, these states are still highly entangled, rendering them non-trivial to realise within a photonics system [200, 201]. To facilitate the experimental realisation of the braiding and

fusion matrices we will adopt an alternative way to obtain the flux conserving elements of $\mathcal{O}$ using a much more experimentally accessible state. To this end, we introduce the product state

$$|\xi\rangle = \frac{1}{3} \sum_{g_1,g_2 \in \{e,c,c^2\}} |g_1, g_2\rangle \,, \tag{5.36}$$

an equal superposition of every element in the two-qutrit Hilbert space. By definition, the expectation value of any operator with respect to this state is the summation of all co-efficients

$$\langle\xi| \mathcal{O} |\xi\rangle = \frac{1}{9} \left(\sum_{\substack{g_1g_2g_3g_4 \in \{e,c,c^2\} \\ g_1g_2 = g_3g_4}} p_{g_1g_2g_3g_4} + \sum_{\substack{g_1g_2g_3g_4 \in \{e,c,c^2\} \\ g_1g_2 \neq g_3g_4}} q_{g_1g_2g_3g_4} \right). \tag{5.37}$$

We consider now the specific structure of our particular operations of interest. Combining Equations (5.12) and (5.27), the '+' and 'G' elements of $(R^{GG})^2$ are calculated as

$$(R_i^{GG})^2 = \frac{1}{12} \sum_{g \in \{e,c,c^2\}} \langle\widetilde{\psi}_g| \mathcal{O}_{R_i} |\widetilde{\psi}_g\rangle \,, \qquad i = +, G \tag{5.38}$$

where $\mathcal{O}_{R_i}$ is the expanded operator product

$$\mathcal{O}_{R_i} = N_i^2 \mathcal{F}_{\rho_1}^G \mathcal{F}_{\rho_2}^G \mathcal{A}^i(v_3) \mathcal{A}^i(v_3) \mathcal{F}_{\rho_1}^G \mathcal{F}_{\rho_2}^G, \qquad i = +, G. \tag{5.39}$$

Inspection of the operator $\mathcal{O}_{R_i}$ reveals that the summation of its non-conservative flux elements is zero, i.e. $\sum_{\substack{g_1g_2 \neq g_3g_4 \\ g_1,g_2,g_3,g_4 \in \{e,c,c^2\}}} q_{g_1g_2g_3g_4} = 0$ for both cases $i = +$ and $i = G$. As a consequence

$$\langle\xi| \mathcal{O}_{R_j^i} |\xi\rangle = \frac{1}{9} \sum_{\substack{g_1g_2 = g_3g_4 \\ g_1,g_2,g_3,g_4 \in \{e,c,c^2\}}} p_{g_1g_2g_3g_4} = \frac{1}{3} \sum_{g \in \{e,c,c^2\}} \langle\widetilde{\psi}_g| \mathcal{O}_{R_j^i} |\widetilde{\psi}_g\rangle \,. \tag{5.40}$$

Similarly, combining Equations (5.14) and (5.27), the elements $([F^G_{GGG}]^i_j)^2$ correspond to

$$([F^G_{GGG}]^i_j)^2 = (\overline{R^{Gj}_G})^2 \frac{\sum_{g\in\{e,c,c^2\}} \langle\widetilde{\psi}_g| \mathcal{O}_{m_{ji}} |\widetilde{\psi}_g\rangle}{\sum_{g\in\{e,c,c^2\}} \langle\widetilde{\psi}_g| \mathcal{O}_{n_j} |\widetilde{\psi}_g\rangle}, \qquad i,j = +, G, \tag{5.41}$$

where

$$\mathcal{O}_{m_{ji}} = \mathcal{F}^G_{\rho_2}\mathcal{F}^G_{\rho_2}\mathcal{A}^j(v_3)\mathcal{F}^G_{\rho_1}\mathcal{A}^G(v_3)\mathcal{A}^G(v_3)\mathcal{F}^G_{\rho_2}\mathcal{A}^i(v_3)\mathcal{F}^G_{\rho_2}\mathcal{F}^G_{\rho_1}, \qquad i,j = +, G, \tag{5.42}$$

and

$$\mathcal{O}_{n_j} = \mathcal{F}^G_{\rho_2}\mathcal{F}^G_{\rho_2}\mathcal{A}^j(v_3)\mathcal{F}^G_{\rho_1}\mathcal{A}^G(v_3)\mathcal{A}^G(v_3)\mathcal{F}^G_{\rho_1}\mathcal{A}^j(v_3)\mathcal{F}^G_{\rho_2}\mathcal{F}^G_{\rho_2}, \qquad i = +, G. \tag{5.43}$$

Inspection of both $\mathcal{O}_{m_{ji}}$ and $\mathcal{O}_{n_j}$ again reveals that the summation of non-conservative flux elements in both cases is zero for all combinations of $i,j \in \{+, G\}$. In this way we obtain equivalent expressions $\langle\xi| \mathcal{O}_{m_{ji}} |\xi\rangle = \frac{1}{3}\sum_{g\in\{e,c,c^2\}} \langle\widetilde{\psi}_g| \mathcal{O}_{m_{ji}} |\widetilde{\psi}_g\rangle$ and $\langle\xi| \mathcal{O}_{n_j} |\xi\rangle = \frac{1}{3}\sum_{g\in\{e,c,c^2\}} \langle\widetilde{\psi}_g| \mathcal{O}_{n_j} |\widetilde{\psi}_g\rangle$.

In the following subsection we will combine each of the reductions presented here, giving explicit forms for the minimal encoding of the squared elements of the R and F matrices from inner products of two qutrit operations with respect to the product states $|\xi\rangle$.

5.3.4 Summary of dense encoding

In summary, we have shown that all relevant inner products as in Eq. (5.12) and Eq. (5.14), may be exactly reconstructed from the action of reduced operations on just two qutrits. The physically measurable quantities in this system are obtained in terms of the '$+$', 'G' components of the transformed anyonic basis. In Appendix D.1, we have demonstrated how these experimentally accessible quantities directly enable the determination of the R and F matrices in the desired anyonic basis $\{A, B, G\}$. Explicitly, the diagonal elements

of the matrix R^{GG} squared, may be obtained as

$$(R_i^{GG})^2 = \begin{cases} \frac{1}{4} \langle \xi | \mathcal{O}_{R_+} | \xi \rangle & i = A, B, \\ \frac{1}{4} \langle \xi | \mathcal{O}_{R_G} | \xi \rangle & i = G, \end{cases} \tag{5.44}$$

while

$$([F^G_{GGG}]^i_j)^2 = \begin{cases} \frac{\langle \xi | \mathcal{O}_{m_{++}} | \xi \rangle}{2 \langle \xi | \mathcal{O}_{n_+} | \xi \rangle} & i, j = A, B, \\ \frac{\langle \xi | \mathcal{O}_{m_{G+}} | \xi \rangle}{2\omega \langle \xi | \mathcal{O}_{n_G} | \xi \rangle} & i = A, B, \quad j = G, \\ \frac{\langle \xi | \mathcal{O}_{m_{+G}} | \xi \rangle}{\langle \xi | \mathcal{O}_{n_+} | \xi \rangle} & i = G, \quad j = A, B, \\ \frac{\langle \xi | \mathcal{O}_{m_{GG}} | \xi \rangle}{\omega \langle \xi | \mathcal{O}_{n_G} | \xi \rangle} & i, j = G. \end{cases} \tag{5.45}$$

Although this scheme is somewhat abstracted from the physical anyonic model, these reduced ribbon operators still directly encode the important fusion and braiding properties of the non-Abelian G anyons. Indeed, the braiding factors corresponding to the different fusion channels of $G \times G$ may still be extracted from the commutativity of the two-qutrit ribbons $\mathcal{F}^G_{\rho_1}$ and $\mathcal{F}^G_{\rho_2}$ as demonstrated in Appendix D.2.

In recent years, significant progress has been made in the physical simulation and control of single and two-qutrit systems across several experimental platforms [202, 203, 204, 205]. In particular, recent advances in the generation of entangled two-qutrit states within photonics architectures [206, 207], have established this as a powerful candidate for the realisation of our proposed anyonic operations on two qutrits. In the next chapter we present a protocol for the realisation of the non-unitary operators $\mathcal{F}^G_{\rho_1}, \mathcal{F}^G_{\rho_2}, \mathcal{A}^+(v_3)$ and $\mathcal{A}^G(v_3)$ on a pair of qutrits encoded in the spatial modes of two photons, providing a direct path to the physical realisation of non-Abelian braiding statistics.

5.4 Photonic Realisation

Photonic quantum systems are among the most promising platforms for the realization of quantum computers and quantum simulators. Due to their weak coupling to the envir-

onment and ability to propagate at the speed of light, photons serve as naturally robust and efficient carriers of quantum information. In addition, their spatial, temporal, and polarization degrees of freedom provide multiple flexible encodings for high-dimensional qudits. To enable the experimental realisation of the densely encoded $\mathbf{D}(\mathbf{S}_3)$ quantum double model, we propose a quantum simulation with a linear interferometric photonic architecture. This platform offers full configurability of arbitrary linear unitaries and allows effective implementation of non-linear operations through measurement-based post-selection. We begin by providing a brief overview of the key features and capabilities of this photonic platform.

5.4.1 A brief overview of linear optics

An N-mode linear optical interferometer is a device constructed from N optical waveguides coupled to each other with an array of parameterised phase shifters and 50:50 beamsplitters. Suppressing the degrees of freedom associated with frequency and polarisation, this system is described by a set of bosonic creation and annihilation operators, $a_i^\dagger$ and a_i, where $i = 1, \ldots, N$ labels the waveguide. These obey the algebra

$$[a_i, a_j] = [a_i^\dagger, a_j^\dagger] = 0, \quad [a_i, a_j^\dagger] = \delta_{ij}. \tag{5.46}$$

The states of this system are obtained via repeated application of the creation operator on the vacuum state $|\mathbf{0}\rangle$. For a system with m modes, states in this occupation basis have the general form $|n_1, n_2, \ldots, n_m\rangle$, where n_i describes the number of photons in the i^{th} mode. The size of the Hilbert space corresponding to a system of n indistinguishable photons distributed among m modes is given by the binomial coefficient $C(n+m-1, n)$.

Linear optical elements apply particle-conserving and non-interacting unitary transformations U on this Hilbert space. These act linearly on the mode operators as

$$U a_i^\dagger U^\dagger = \sum_{j=1}^{N} u_{ji} a_j^\dagger, \tag{5.47}$$

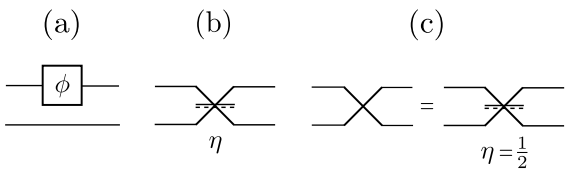

Figure 5.2: (a) A phase shifter and (b) beamsplitter within a two-mode circuit. (c) The simplified crossing (left) represents the $50:50$ beamsplitter with $\eta = \frac{1}{2}$.

where $u \in U(N)$. The unitary U forms a representation of the smaller unitary u, such that U is uniquely specified by the operator u. The two basic 'building blocks' of linear optical circuits are taken to be the phase shifter and beamsplitter as shown in Figure 5.2. The phase shifter, $U_{\rm ps}(\phi)$, acts on a single mode i such that $a_i^\dagger \mapsto e^{i\phi} a_i^\dagger$. For a two-mode system as in Figure 5.2, with the phase shift applied to the upper mode, we obtain the corresponding unitary

$$u_{\rm ps}(\phi) = \begin{pmatrix} e^{i\phi} & 0 \\ 0 & 1 \end{pmatrix}. \tag{5.48}$$

The beamsplitter, $U_{\rm bs}(\eta)$, is a two-mode optical component which may be used to perform controlled transmission and reflection of incident light [208, 209]. There are many distinct but ultimately equivalent conventions for describing the action of a beamsplitter. Here, we consider asymmetric beamsplitters with a single parameter $0 \leq \eta \leq 1$ corresponding to the reflectivity of the chosen element. Notably such an asymmetric beamsplitter applies a differing phase shift dependent on the port that the light is incident on. For the beamsplitter element as shown in Figure 5.2(b), light incident on the solid (dashed) surface acquires a phase $\sqrt{\eta}$ ($-\sqrt{\eta}$), while light transmitted through either surface gains the phase $\sqrt{1-\eta}$. Explicitly for the two-mode system shown, one has $a_1^\dagger \mapsto \sqrt{\eta} a_1^\dagger + \sqrt{1-\eta} a_2^\dagger$, $a_2^\dagger \mapsto \sqrt{1-\eta} a_1^\dagger - \sqrt{\eta} a_2^\dagger$. When $\eta = \frac{1}{2}$, the incident light has equal probability of being reflected or transmitted. In our convention, this $50:50$ beamsplitter has explicit matrix representation

$$u_{\rm bs}\left(\eta = \frac{1}{2}\right) = \frac{1}{\sqrt{2}} \begin{pmatrix} 1 & 1 \\ 1 & -1 \end{pmatrix}, \tag{5.49}$$

equivalent to the Hadamard gate [192], a key component in many schemes for universal quantum computation [21].

In [210], Reck et al. demonstrated that any $N \times N$ unitary u can be factorised into a sequence of these simple phase shift and beamsplitter transformations. The ability to generate any unitary u however, does however does not mean that this is a universal quantum computer, as only linear unitaries that act as Eq. (5.47) can be encoded. Crucially, the lack of photon-photon interactions results in an inability to engineer arbitrary entanglement between multiple qudits [211, 212, 213].

For many years, it was believed that scalable all-optical quantum computing would require the introduction of a non-linear component, such as a Kerr medium. These Kerr non-linearities induce intensity-dependent phase shifts in optical fields, thus effectively mediating interactions between photons to enable the implementation of non-Gaussian entangling operations [214, 215]. Naturally occurring Kerr effects however, are significantly weaker than those required to physically implement such schemes, making such gates practically unfeasible with current or near-term technologies [216]. In 2001, Knill, Laflamme and Milburn revolutionized linear quantum optics by demonstrating that efficient quantum computation was in fact possible using only beamsplitters, phase shifters and single-photon sources with the simple addition of projective measurements [191]. This scheme, known as the KLM protocol, initiated the field of non-deterministic linear optics, in which non-linear operations describing interactions between qudits may be implemented with some finite probability of success p.

Here, we briefly outline the KLM protocol for the realisation of the non-linear sign (NS) gate as presented in [191]. This gate describes the following phase shift on a single mode

$$\alpha \left|0\right\rangle + \beta \left|1\right\rangle + \gamma \left|2\right\rangle \mapsto \alpha \left|0\right\rangle + \beta \left|1\right\rangle - \gamma \left|2\right\rangle , \tag{5.50}$$

equivalent to the non-linear operation $\exp\left(\frac{i\pi}{2}(a_i^\dagger a_i(a_i^\dagger a_i - 1))\right)$. In order to realise this operation we construct the circuit shown in Figure 5.3. The upper mode encodes the input state $\left|\psi\right\rangle$, while the middle and bottom modes are ancillae with inputs of a single

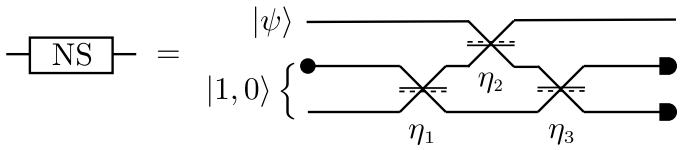

Figure 5.3: The non-linear sign (NS) gate realizes a non-deterministic phase shift on a single mode $|\psi\rangle$ using a combination of beamsplitters, ancillae modes and photodetectors. The beam splitters are characterised by reflectivity parameters η_1, η_2 and η_3 as detailed in Appendix D.3. The input states for the ancillae are a single photon and the vacuum, and the gate succeeds when the detectors measure one and zero photons respectively. For an arbitrary input state $\alpha_0 |0\rangle + \beta_1 |1\rangle + \gamma_2 |2\rangle$, this occurs with probability $p_{NS} = \frac{1}{4}$.

photon and the vacuum respectively. All components of the circuit itself are simple asymmetric beamsplitters, the action of which is described in further detail in Appendix D.3. For the input state $|\psi_{in}\rangle = |\psi\rangle \otimes |1,0\rangle_A$ with $|\psi\rangle = \alpha |0\rangle + \beta |1\rangle + \gamma |2\rangle$, the total output state is given by

$$|\psi_{out}\rangle = \frac{1}{2} (\alpha |0\rangle + \beta |1\rangle - \gamma |2\rangle) \otimes |1,0\rangle_A + \ldots, \tag{5.51}$$

where only terms for which the ancillae are in the state $|1,0\rangle_A$ have been explicitly included. By post-selecting on the ancillae measurements '1' and '0' respectively, we therefore obtain the desired outcome of the NS gate on the upper mode with probability $p_{\text{NS}} = \left|\frac{1}{2}\right|^2 = \frac{1}{4}$. This gate will act as an important building block in our construction of linear optics circuits for the non-unitary ribbon and projection operators.

5.4.2 State initialization

In this subsection and the following, we outline a protocol for the simulation of our two-qutrit model using linear optics only. To this end, we introduce two three-mode interferometers, such that a single qutrit may be encoded by a single photon in three optical modes $|e\rangle \equiv |1,0,0\rangle, |c\rangle \equiv |0,1,0\rangle, |c^2\rangle \equiv |0,0,1\rangle$ as shown in Figure 5.4(a), thus preserving the tensor product structure of states in our system. Throughout the following, states labelled by group elements $|e\rangle, |c\rangle, |c^2\rangle$ refer to the logical states of each qutrit, while states $|0\rangle, |1\rangle, |2\rangle$ refer to the occupation basis of a single mode containing

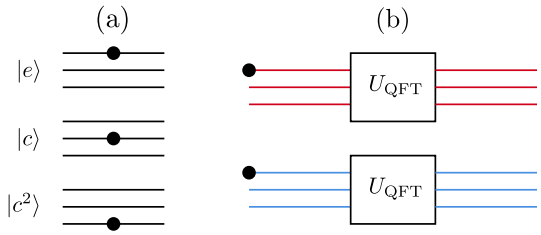

Figure 5.4: (a) On a three-mode interferometer each qutrit state $|e\rangle, |c\rangle, |c^2\rangle$ may be encoded by a single photon in the first second or third mode respectively. (b) The state $|\xi\rangle$ is constructed deterministically from the action of the qutrit unitary U_{QFT} on the initial state with a single photon in the first mode of each qutrit.

$0, 1$ and 2 photons respectively.

In the dense encoding scheme presented in Section 5.3, we showed that the elements $(R_i^{GG})^2$ and $([F_{GGG}^G]_j^i)^2$ are encoded in the inner products of certain two-qutrit operations with respect to the state $|\xi\rangle$, the equal superposition over all two-qutrit basis states. This state may be constructed deterministically from a pair of single-qutrit unitaries as

$$|\xi\rangle = (U_{\mathrm{QFT}} \otimes U_{\mathrm{QFT}})|e, e\rangle = \frac{1}{3} \sum_{g_1, g_2 \in \{e, c, c^2\}} |g_1, g_2\rangle, \tag{5.52}$$

where U_{QFT} is the Fourier transform acting on the basis of a single qutrit as

$$U_{\mathrm{QFT}} = \frac{1}{\sqrt{3}} \begin{pmatrix} 1 & 1 & 1 \\ 1 & \omega & \bar{\omega} \\ 1 & \bar{\omega} & \omega \end{pmatrix}, \tag{5.53}$$

as shown in Figure 5.4(b). Note that in the qutrit Pauli operator basis [204, 217], this gate transforms the X and Z generators as

$$U_{\mathrm{QFT}} X U_{\mathrm{QFT}}^\dagger = Z, \quad U_{\mathrm{QFT}} Z U_{\mathrm{QFT}}^\dagger = X^\dagger, \tag{5.54}$$

a property that will be useful in the following.

5.4.3 Ribbon operators

We now consider the realisation of the two-qutrit ribbon operators as given in Eq. (5.30) and (5.31). These operations may be conveniently diagonalised using the identity in Eq. (5.54), giving

$$\mathcal{F}^G_{\rho_1} = (\mathbf{1} \otimes U_{\mathrm{QFT}})\mathcal{D}_F(\mathbf{1} \otimes U^\dagger_{\mathrm{QFT}}), \tag{5.55}$$

$$\mathcal{F}^G_{\rho_2} = (U^\dagger_{\mathrm{QFT}} \otimes \mathbf{1})\mathcal{D}_F(U_{\mathrm{QFT}} \otimes \mathbf{1}), \tag{5.56}$$

where

$$\mathcal{D}_F = Z \otimes Z^\dagger + Z^\dagger \otimes Z. \tag{5.57}$$

This diagonal component acts on the two-qutrit basis as

$$\mathcal{D}_F|g_1, g_2\rangle = \begin{cases} 2|g_1, g_2\rangle & \text{if } g_1 = g_2, \\ -|g_1, g_2\rangle & \text{if } g_2 \neq g_2, \end{cases} \tag{5.58}$$

clearly identifying the non-unitary action of these operators. The circuits for the full ribbon operators are given by

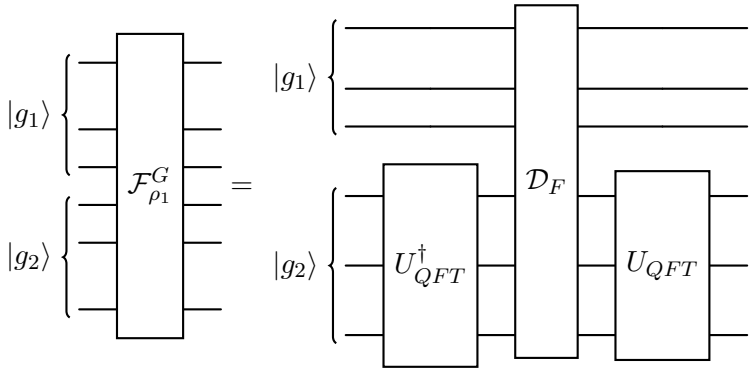

and

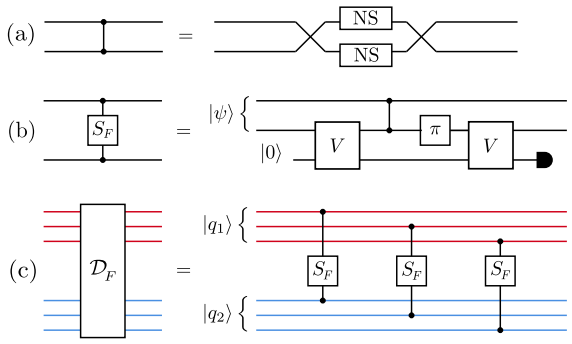

Figure 5.5: (a) The controlled sign (CS) gate is constructed from two 50:50 beamsplitters and pair of non-linear sign (NS) gates acting on two modes as shown. (b) The circuit encoding the non-unitary operation S_F utilises two logical modes and an ancillary mode prepared in the vacuum state $|0\rangle$. (c) The diagonal ribbon operator D_F can be implemented by pairwise coupling the three modes of a pair of qutrits with S_F gates.

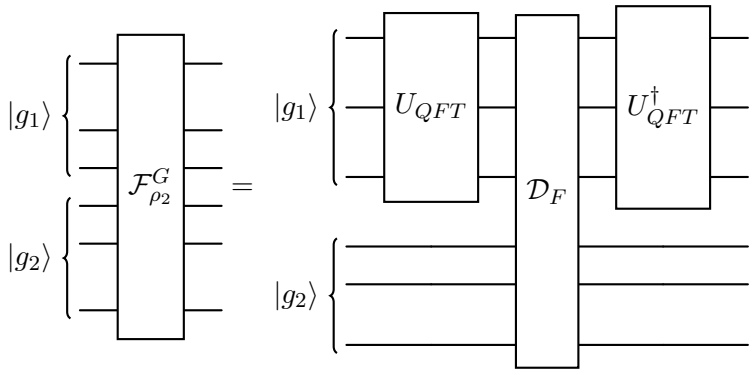

In order to construct this diagonal non-unitary $\mathcal{D}_F$, we start by considering the condition $g_1 = g_2$. Each qutrit is encoded by a single photon in three optical modes such that we may represent these logical states as $|g_1\rangle = |m_1, m_2, m_3\rangle$ and $|g_2\rangle = |n_1, n_2, n_3\rangle$ where $m_i, n_j = 0, 1$ with exactly one $m_i, n_j = 1$ and the others equal to zero. In this occupation basis, it is clear that the condition $g_1 = g_2$ is equivalent to $m_i = n_i$ for all $i = 1, 2, 3$. To enforce this condition, we therefore start by constructing an operator S_F, that acts as a control between pairs of modes (m_i, n_i) across both qutrits.

Figure 5.5(b) shows the circuit diagram for the construction of the two-mode operator S_F. The circuit consists of three modes: two logical and a single ancillary mode prepared in the vacuum state, $|0\rangle$. The crossings between the second and third modes represent

the unitary V, which has the following representation on the space of three modes

$$V = \begin{pmatrix} 1 & 0 & 0 \\ 0 & -\frac{\sqrt{3}}{2} & \frac{1}{2} \\ 0 & \frac{1}{2} & \frac{\sqrt{3}}{2} \end{pmatrix}, \tag{5.59}$$

while the π-phase shifter implements the transformation $a_2^\dagger \mapsto e^{i\pi} a_2^\dagger$. The non-linear element of this circuit is the CS gate, which may be realised from a pair of 50:50 beamsplitters and NS gates as shown in Figure 5.5(a). On the subspace of at most one photon per mode, the CS gate maps the general input state $\alpha\,|0,0\rangle + \beta\,|0,1\rangle + \gamma\,|1,0\rangle + \delta\,|1,1\rangle \mapsto \alpha\,|0,0\rangle + \beta\,|0,1\rangle + \gamma\,|1,0\rangle - \delta\,|1,1\rangle$. Each NS has a success probability $p_{\mathrm{NS}} = \frac{1}{4}$, meaning that the CS gate overall succeeds with probability $p_{\mathrm{CS}} = \frac{1}{16}$.

Suppose we prepare the system in the input state

$$|\Psi_{\mathrm{in}}\rangle = |\psi\rangle \otimes |0\rangle_A = (\alpha|0,0\rangle + \beta|0,1\rangle + \gamma|1,0\rangle + \delta|1,1\rangle) \otimes |0\rangle_A. \tag{5.60}$$

The output state is given by

$$|\Psi_{\mathrm{out}}\rangle = (\alpha|0,0\rangle - \frac{\beta}{2}|0,1\rangle + \gamma|1,0\rangle + \delta|1,1\rangle) \otimes |0\rangle_A + \frac{\sqrt{3}\beta}{2}|0,0\rangle \otimes |1\rangle_A. \tag{5.61}$$

By post-selecting on the ancillary mode being in the vacuum state $|0\rangle_A$, we therefore obtain, up to a normalisation, the logical output $|\psi_{\mathrm{out}}\rangle = \mathcal{N} S_F |\psi_{\mathrm{in}}\rangle$, where S_F is the non-unitary operator that acts on the photonic number basis states as

$$S_F|m,n\rangle = \begin{cases} -\frac{1}{2}|m,n\rangle & \text{if } |m,n\rangle = |0,1\rangle, \\ |m,n\rangle & \text{otherwise,} \end{cases} \tag{5.62}$$

and $\mathcal{N} = 1/\|\psi_{\mathrm{out}}\|$ is a normalisation factor. The probabilistic nature of this circuit means that the desired outcome is achieved with probability $p_{S_F} = \frac{1}{4}$. An important point to note is that because the gate S_F is non-unitary, the normalisation constant

$\mathcal{N}$ must be chosen correctly to retain the non-unitary character. For example, if we send through the state $|0,1\rangle$ and normalise by dividing through by the norm as usual, we would cancel the important factor of $-1/2$. This normalisation factor arises when we run the quantum computer multiple times, post-select on successful outputs, and normalise the resultant probability distribution of our measurements. As we are encoding a non-unitary gate, instead of taking our distribution as the number of measurements after post-selection divided by the total number of successful shots, we normalise with the total number of shots, which includes shots that failed after post-selection. In this way we retain the desired non-unitarity.

This two-mode gate S_F forms an important building block in the construction of the non-unitary two-qutrit ribbons operators $\mathcal{F}^G_{\rho_1}$ and $\mathcal{F}^G_{\rho_1}$. Consider the action of S_F when applied between each of the three pairs of modes (m_i, n_i) as shown in Figure 5.5(c). As in Eq. (5.62) each gate will act trivially apart from the case where the mode m_i contains the vacuum and n_i has a single photon. For the single occupation basis, the action of this circuit is restricted to two outcomes. Either $m_i = n_i$ for all modes i, and S_F acts trivially between each pair, or a single pair of modes will obey $(m_i = 0, n_i = 1)$ such that the total state acquires a single factor of $-\frac{1}{2}$. Up to a normalization, the circuit shown in Figure 5.5(c) therefore implements the transformation $\frac{1}{2}\mathcal{D}_F$ on the basis of two qutrits. This additional factor may be accounted for by scaling our measurements by a factor of 2 for each ribbon operator present. In order to implement the full two-qutrit gates $\mathcal{F}^G_{\rho_1}$ and $\mathcal{F}^G_{\rho_2}$, one simply applies the constructed D_F operator between pairs of simple unitary operations as outlined in Equations (5.55) and (5.56).

5.4.4 Projection operators

We consider now, the two-qutrit projection operators given in Equations (5.32) and (5.33). As with the ribbon operators, it is convenient to diagonalise these operators as

$$\mathcal{A}_i = (U_{QFT} \otimes U_{QFT})\mathcal{D}_i(U^\dagger_{QFT} \otimes U^\dagger_{QFT}), \tag{5.63}$$

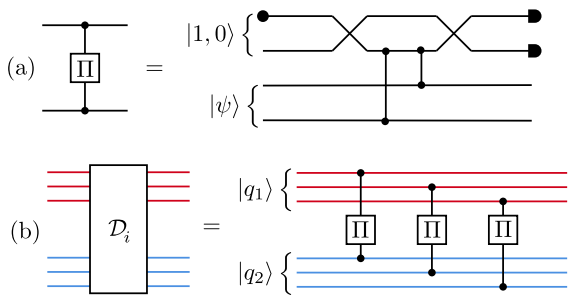

Figure 5.6: (a) The two-mode parity projection Π. Here, the upper pair of modes are ancillary modes and contain a single photon. The ancillary and logical modes are pairwise coupled with a controlled π-phase shifter as in Fig. 5.5(a). Post-selection on the measurement of the ancillary qubit applies an even or odd parity projection to the logical modes. (b) The two-qutrit gate $\mathcal{D}_i$. By pairwise coupling the modes of a pair of qutrits $|g_1\rangle$ and $|g_2\rangle$ we can project onto the even or odd parity qutrit subspace by post-selecting on the outputs of each Π.

where $i = +, G$. The circuit for this decomposition is given by

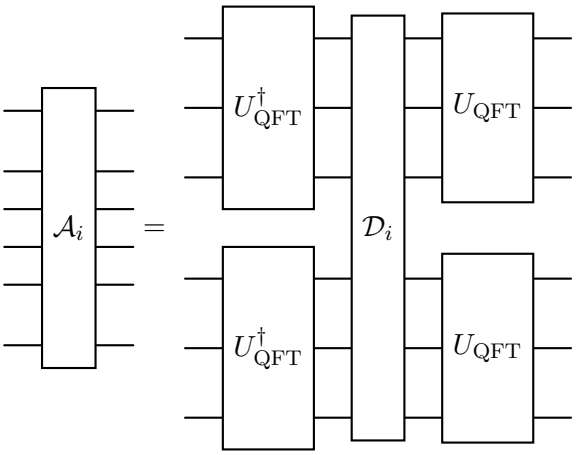

where $\mathcal{D}_i$ acts on the basis of qutrit states as

$$\mathcal{D}_+|g_1, g_2\rangle = \begin{cases} \frac{1}{\sqrt{2}}|g_1, g_2\rangle & \text{if } g_1 = g_2, \\ 0 & \text{if } g_1 \neq g_2, \end{cases} \tag{5.64}$$

$$\mathcal{D}_G|g_1, g_2\rangle = \begin{cases} 0 & \text{if } g_1 = g_2, \\ |g_1, g_2\rangle & \text{if } g_1 \neq g_2. \end{cases} \tag{5.65}$$

The factor $\frac{1}{\sqrt{2}}$ in the $\mathcal{D}_+$ term arises due to the normalization of the linear superposition

$A^+(v_3) = \frac{1}{\sqrt{2}}(A^A(v_3) + A^B(v_3))$. We note that $\mathcal{D}_+$ and $\mathcal{D}_G$ may be interpreted in terms of projections onto even and odd parity subspaces respectively. As with the ribbon operators, we will implement this parity check between two-qutrit states, by first constructing a circuit that projects onto the parity subspaces of a pair of modes.

Consider the circuit shown in Figure 5.6(a). The top two modes now are ancillae, containing a single photon which plays the role of an ancillary qubit. This qubit entangles with the even and odd parity subspaces of the two modes of interest, allowing for a projection to be made non-destructively. Explicitly, given the most general two-mode photonic input state $|\psi\rangle = \alpha|0,0\rangle + \beta|0,1\rangle + \gamma|1,0\rangle + \delta|1,1\rangle$, the circuit implements the transformation Π such that

$$\Pi|1,0\rangle_A \otimes |\psi\rangle = |1,0\rangle_A \otimes (\alpha|0,0\rangle + \delta|1,1\rangle) + |0,1\rangle_A \otimes (\beta|0,1\rangle + \gamma|1,0\rangle), \tag{5.66}$$

$$= |1,0\rangle_A \otimes |\psi_{\text{even}}\rangle + |0,1\rangle_A \otimes |\psi_{\text{odd}}\rangle. \tag{5.67}$$

By post-selecting on the state of the ancillary qubit, one can project onto the odd or even parity subspace. With this two-mode parity projection at hand, one can therefore perform the qutrit parity projection by pairwise coupling the nth mode of each qutrit with a Π gate as shown in Fig. 5.6(b). The additional factor of $\frac{1}{\sqrt{2}}$ for the $\mathcal{D}_+$ operator may once again be accounted for by scaling our measurements by a factor of $\frac{1}{\sqrt{2}}$ for each $\mathcal{A}^+(v_3)$ operator present. The implementation of the full projection operator $\mathcal{A}^i(v_3)$, is thus achieved with the application of the constructed operator $\mathcal{D}_i$ between pairs of additional simple unitary gates as outlined in Equation (5.63).

This circuit construction enables the realization of the two-qutrit operators $\mathcal{F}^G_{\rho_i}$ and $\mathcal{A}^j(v_3)$, encoding fundamental anyonic operations, in a form directly implementable using linear-optics techniques. While a photonic implementation is attractive due to the inherently low decoherence of photons, linear optical elements remain susceptible to physical noise processes [192]. In the following section, we evaluate the performance of our topological encoding against such errors, comparing it directly to the implementation of

the R and F gates on a single logical qutrit. The results obtained reveal a novel form of error resilience that lies outside the conventional paradigm of topological protection, highlighting the potential of this approach for robust quantum information processing.

5.5 Error resilience

In Section 5.3, we presented a scheme in which the action of the R and F matrices on the anyonic basis $\{A, B, G\}$ is topologically encoded via ribbon and projection operations on two physical qutrits. In practice, however, operations on physical systems are inevitably imperfect and subject to various sources of error. In large topological systems, coherent errors that act as local perturbations to the Hamiltonian do not affect the topologically encoded information, providing passive protection without the need for active quantum error correction [218, 219]. However, noise in the form of decoherence, such as coupling to an external environment, can be detrimental to the logical encoding, as topological models offer no intrinsic protection against such non-unitary errors [220].

In this section, we perform an analysis comparing the resilience of the encoding of the R and F matrices on two physical qutrits with their conventional action on a single logical qutrit against these more physically relevant errors. Remarkably, we find that the topologically encoded R gate is completely immune to errors in the form of decoherence. The F gate also exhibits an enhanced resilience against these errors, provided the probability of error remains below a well-define threshold. This effect, which has no direct analogue in conventional topological protection, highlights the suitability of our implementation for realistic experimental conditions.

The protocol for this comparison is introduced explicitly in the next section with direct analysis of the robustness of the encoded and unencoded circuits for the R matrix against errors in the form of single-qutrit decoherence. Here and throughout, the 'encoded circuit' refers to the set of operations used to extract the elements of R and F from two physical qutrits, while the 'unencoded circuit' refers to the direct application of these gates on a single logical qutrit representing the anyonic basis $\{A, B, G\}$. In both cases,

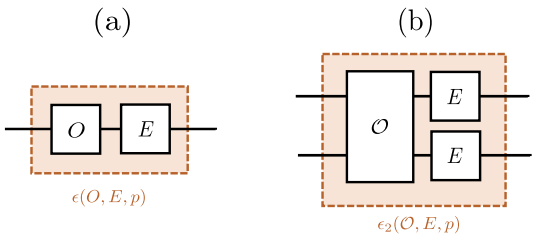

Figure 5.7: In this scheme, error is modelled with the introduction of an independent unitary fault E to each qutrit under the action of a (a) single-qutrit operator O or (b) two-qutrit operator $\mathcal{O}$.

local errors are modelled as independent unitary faults acting on each participating qutrit with probability p as

$$\epsilon(O, U_E, p) = (1-p)O + pU_E O U_E^\dagger, \tag{5.68}$$

where U_E represents an error channel acting on the relevant Hilbert space [221, 222]. In the following, each such unitary will be represented in terms of a single qutrit unitary error gate E, chosen to reflect a relevant physical error process. Action of this same gate independently across each qutrit in both circuits, thus enables a direct comparison of the relative robustness of each model to a given source of error.

5.5.1 Resilience to decoherence

Here, we present a protocol for evaluating the robustness of each circuit against physically relevant types of error. We start by introducing this general scheme, before presenting explicit results for errors in the form of decoherence.

Figure 5.7(b) illustrates the components of the encoded circuit whereby two-qutrit operations are subject to noise on each qutrit. In this circuit, 'noisy' forms of the R and F matrices are computed by passing each operator in the relevant operator products (5.39), (5.42), (5.43) through the error channel (5.68). Consider, for example, the computation of the R matrix elements from

$$(R_i^{GG})^2 = \frac{\langle\phi_{12}(i)|\phi_{21}(i)\rangle}{\langle\phi_{21}(i)|\phi_{21}(i)\rangle} = \frac{Tr(\mathcal{F}^G_{\rho_2}\mathcal{F}^G_{\rho_1}\mathcal{A}^i(v)\mathcal{A}^i(v)\mathcal{F}^G_{\rho_2}\mathcal{F}^G_{\rho_1}\rho)}{Tr(\mathcal{F}^G_{\rho_1}\mathcal{F}^G_{\rho_2}\mathcal{A}^i(v)\mathcal{A}^i(v)\mathcal{F}^G_{\rho_2}\mathcal{F}^G_{\rho_1}\rho)}, \qquad i = +, G,$$

with $\rho = |\xi\rangle\langle\xi|$. When acting on a physical system, each physical qutrit may be subject to some external noise. We model these as independent sources of error, introducing the corresponding error gates $U_{E,1} = E \otimes \mathbf{1}_3$ and $U_{E,2} = \mathbf{1}_3 \otimes E$. The total 'noisy' form of the operator $\mathcal{O}$ is then compounded as

$$\epsilon_2(\mathcal{O}, E, p) = \epsilon(\epsilon(\mathcal{O}, U_{E,1}, p), U_{E,2}, p). \tag{5.69}$$

In this way, the elements $(R_i^{GG})^2$ in this noisy channel become

$$(R_i^{\text{err}}(E,p))^2 = \frac{Tr(\epsilon(\mathcal{F}_{\rho 2}^G, E, p)\epsilon(\mathcal{F}_{\rho 1}^G, E, p)\epsilon(\mathcal{A}^i(v), E, p)\epsilon(\mathcal{A}^i(v), E, p)\epsilon(\mathcal{F}_{\rho 2}^G, E, p)\epsilon(\mathcal{F}_{\rho 1}^G, E, p)\epsilon(\rho, E, p))}{Tr(\epsilon(\mathcal{F}_{\rho 1}^G, E, p)\epsilon(\mathcal{F}_{\rho 2}^G, E, p)\epsilon(\mathcal{A}^i(v), E, p)\epsilon(\mathcal{A}^i(v), E, p)\epsilon(\mathcal{F}_{\rho 2}^G, E, p)\epsilon(\mathcal{F}_{\rho 1}^G, E, p)\epsilon(\rho, E, p))}.$$

For some normalised input state in the logical qutrit Hilbert space, $|\psi_{\text{in}}\rangle = \alpha|A\rangle + \beta|B\rangle + \gamma|G\rangle$, the output state is therefore

$$|\psi_{\text{out}}^{\text{err}}(E,p)\rangle = \mathcal{N}[(R_+^{\text{err}}(E,P))^2(\alpha|A\rangle + \beta|B\rangle) + (R_G^{\text{err}}(E,p))^2\gamma|2\rangle], \tag{5.70}$$

where $\mathcal{N}$ is a normalization constant required to produce the valid output density matrix

$$\rho_{\text{out}}^{\text{enc}}(E,p) = |\psi_{\text{out}}^{\text{err}}(E,p)\rangle\langle\psi_{\text{out}}^{\text{err}}(E,p)|. \tag{5.71}$$

The fidelity relative to the ideal output $\rho_{\text{out}} = (R^{GG})^2|\psi_{\text{in}}\rangle\langle\psi_{\text{in}}|[(R^{GG})^2]^\dagger$ is given by

$$\mathfrak{F}^{\text{enc}}(E,p) = \sqrt{\text{Tr}(\rho_{\text{out}}\rho_{\text{out}}^{\text{enc}}(E,p))}. \tag{5.72}$$

Alternatively, one may consider the direct action of $(R^{GG})^2$ on a single logical qutrit. For a general normalised input state $|\psi_{\text{in}}\rangle = \alpha|A\rangle + \beta|B\rangle + \gamma|G\rangle$, one now obtains the ideal outcome

$$|\psi_{\text{out}}\rangle = \bar{\omega}(\alpha|0\rangle + \beta|1\rangle) + \omega\gamma|2\rangle \tag{5.73}$$

such that

$$\rho_{\text{out}} = |\psi_{\text{out}}\rangle\langle\psi_{\text{out}}|. \tag{5.74}$$

The error in this circuit is then simulated at the state level in terms of this ideal output density matrix ρ_{out} as

$$\rho_{\text{out}}^{\text{un}}(E,p) = \epsilon(\rho_{\text{out}}, E, p). \tag{5.75}$$

The fidelity of the circuit is expressed as

$$\mathfrak{F}^{\text{un}}(E,p) = \sqrt{Tr(\rho_{\text{out}}\rho_{\text{out}}^{\text{un}}(E,p))}. \tag{5.76}$$

The single-qutrit error channel E can be chosen to reflect the dominant noise mechanism in a given physical implementation. In photonic platforms, a primary source of error is dephasing arising from imperfect interference in the interferometric setup [221, 223]. This decoherence is often modeled through a correlated dephasing channel, $U_E = Z \otimes Z$, where the single-qutrit Z operator captures the most severe dephasing effects. In the present analysis, we extend this framework by considering uncorrelated dephasing errors, modeled as in (5.69) with $E = Z$. This generalization enables a more versatile and platform-independent evaluation of the encoding's fault-tolerance.

Naturally, the effect of errors will manifest differently dependent on the chosen input state $|\psi_{in}\rangle$. To obtain a statistically meaningful comparison, we therefore consider the average values obtained over a set of 2000 randomised input states. These states are randomly sampled from the qutrit Hilbert space through the application of Haar random matrices [224, 225] to an arbitrary initial state $|\psi_0\rangle = \frac{1}{\sqrt{3}}(|A\rangle + |B\rangle + |G\rangle)$.

Consider the first set of plots for our analysis of decoherence errors with $E = Z$ shown in Figure 5.8. Plots (a) and (c), compare the average fidelity of both circuits acting on a random logical state for R and F respectively. Interestingly, we see that not only does the encoded R maintain a high fidelity > 0.95 across all error probabilities, it also consistently outperforms the average fidelity of the conventional gate-based unencoded circuit across this range. By comparison, for the average fidelities for the circuits for F, a threshold appears at around $p_{\text{th}} \approx 0.052$. For a system with a noise rate below this threshold, we therefore conclude that one will achieve on average a higher fidelity using

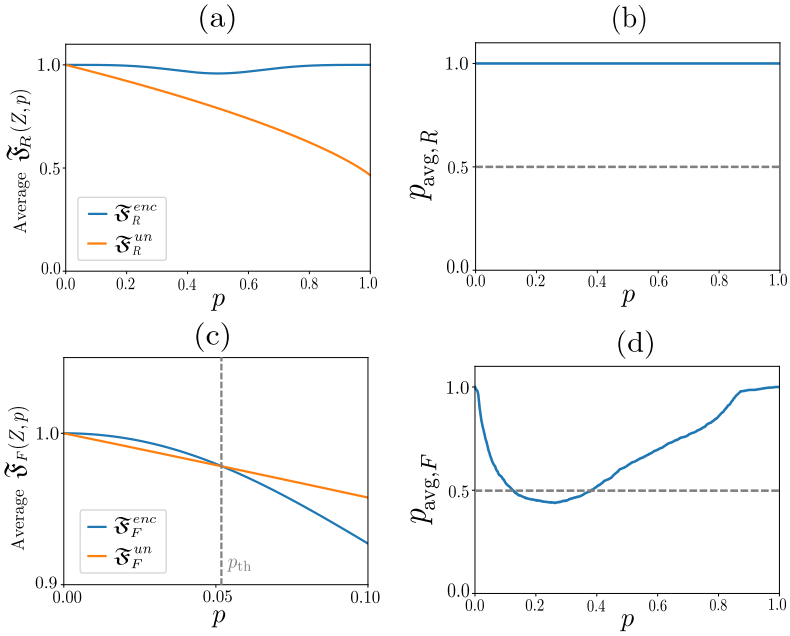

Figure 5.8: (a) The average fidelity for the encoded circuit for R demonstrates advantage over the unencoded case for all probabilities of error p. This is further demonstrated in (b) where the p_{avg} retains near unit value. For the F matrix as considered in (c) and (d) threshold behaviour emerges. By controlling the probability of error below p_{th}, one will achieve on average a higher fidelity using the physical encoding.

the physical encoding of the F matrix on two qutrits.

A further comparison between both approaches is given in Figure 5.8(b) and (d). Here p_{avg} represents the averaged probability that the encoded fidelity exceeds the unencoded fidelity across the ensemble of input states. Fig. 5.8(d) shows that for the encoded F matrix this probability exceeds 50% for $p < 0.124$, indicating a regime where the encoded scheme is more likely to yield higher fidelity on a random input. In keeping with Fig. 5.8(a), the encoded R matrix is shown to outperform the conventional gate-based approach with unit probability across the full range of errors. This clear robustness against decoherence at physically relevant rates, demonstrates that the topological encoding offers a degree of passive protection against decoherence, even in the minimal implementation of two qudits considered here.

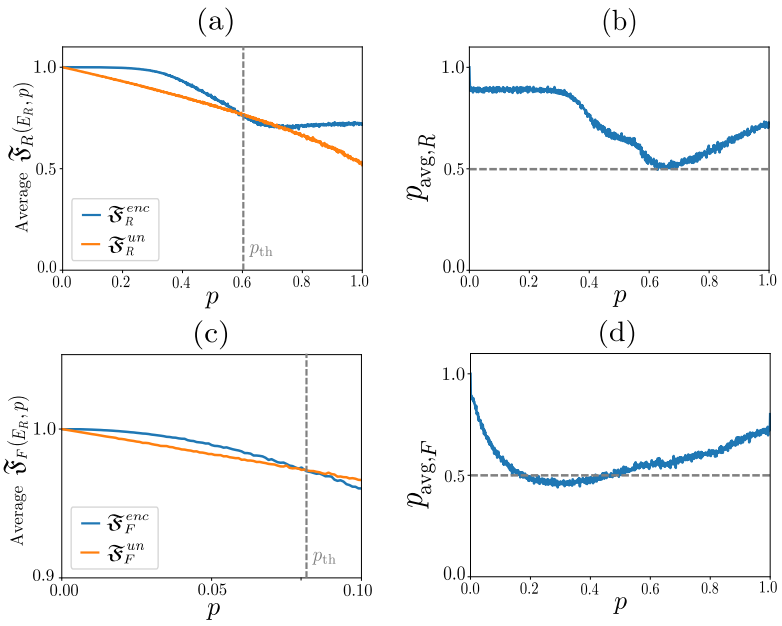

Figure 5.9: Comparisons of the robustness of the encoded and unencoded circuits for the R and F operators under randomised qutrit Pauli errors. In (a) and (c) thresholds now appear for the average fidelity for the encoding of both circuits, while in (b) consistent advantage is still observed on average for the encoding of R. In (d) This advantage is accessed below the threshold value $p < 0.17$.

5.5.2 Resilience to randomised noise

In the previous subsection, we analysed both the encoded and unencoded circuits for the R and F matrices under decoherence errors. While such noise represents the most relevant limitation for an experimental realisation such as that presented in Section 5.4, additional imperfections such as mode mismatch from non-ideal beam splitters can also play a role. Indeed, each chosen platform may be subjected to a range of differing sources of noise processes throughout the computation. To enable a more general and platform-independent analysis, we therefore extend our study to include random errors E_R, randomly sampled at each stage from the single qutrit Pauli group $E_R \in \{X^i Z^j\}$ with $i, j = 0, 1, 2$. The results for this analysis are presented in Figure 5.9(a) and (c). We observe now an advantage threshold for both the R and F encoded circuits occurring at $p_{\text{th}} = 0.61$ and $p_{\text{th}} = 0.08$ respectively. Remarkably, when randomised noise is kept below

these relatively high thresholds, one again gains a clear advantage by using the encoded circuits in both cases. Finally, Figure 5.9(b) and (d) illustrate the average probability that the encoded circuit achieves higher fidelity than the unencoded across a range or probabilities p. For the F matrix, $p_{\text{avg}} \geq \frac{1}{2}$ for $p < 0.17$. Crucially, for the R matrix, this average probability does not drop below 50%, meaning that to implement the R gate with maximum fidelity, it is always better on average to do so using the encoded circuit.

The threshold behaviour revealed by both error analyses demonstrates the inherent passive protection provided by the topological encoding, extending beyond conventional notions of topological fault tolerance. Even in this minimal implementation, the encoding significantly suppresses decoherence and randomized qutrit Pauli errors, with the R matrix encoding exhibiting complete immunity to the dominant dephasing errors in the proposed linear-optics setup. Importantly, the threshold values p_{th} are significantly higher than the error thresholds typically required for fault-tolerant quantum computation [222, 226, 227], underscoring the suitability of this protocol for scalable quantum computing.

5.6 Conclusions

In this chapter, we have investigated the physical realisation of our protocol for demonstrating the non-Abelian braiding statistics of G anyons within the $\mathbf{D}(\mathbf{S}_3)$ quantum double model on a lattice. By adapting the scheme to align with the capabilities of current photonic technologies, this work provides a practical blueprint for the near-term implementation of topological braiding operations. Importantly, the approach offers an alternative to conventional gate-based protocols, exhibiting enhanced resilience to typical sources of error and decoherence.

Building on the scheme presented in the previous chapter, we began by constructing the minimal lattice capable of supporting the full spectrum of anyonic excitations described by Kitaev's Hamiltonian. Despite its simplicity, this minimal system still demands coherent control over a 6^4-dimensional Hilbert space in order to realise the states

that support static braiding operations, a task outside of the scope of current quantum hardware. While other approaches such as that of Goel et al. [148] reduce complexity by performing tomography on the anyonic ribbon operators abstracted from the lattice construction, our approach emphasises the importance of the explicit encoding of the topologically protected fusion space on which logical information may be encoded [refs]. In our approach we therefore sought to retain this coherent state space construction, while introducing a set of simplifications rendering the protocol accessible to current quantum technologies.

In Section 5.3, we introduced a dense encoding scheme based on the structure of the single-plaquette ground state and its associated operators. Locality constraints reduce the non-trivial action of all operators to just two qudits, which can be expressed in terms of qutrit Pauli generators, revealing a tensor-sum structure linked to the semi-group of S_3. The null action on elements $\{t, tc, tc^2\}$ shows that the essential dynamics of the $\{A, B, G\}$ sub-model are fully captured within an effective qutrit basis $\mathbf{Z}_3 \cong \{e, c, c^2\}$. Although abstracted from the full quantum double formalism, a tomographic analysis (Appendix D.2) confirmed that these reduced operators retain the defining features of anyonic operations. Finally, decomposition of the operator products revealed a cancellation of flux non-conserving terms, allowing the elements of $(R^{GG})^2$ and $([F^G_{GGG}]^i_j)^2$ to be computed directly from inner products of the two-qutrit operators with respect to the product state $|\xi\rangle$.

With growing interest in higher-dimensional qudits for quantum computation and communication, significant progress has been made in simulating and controlling such systems across a range of experimental platforms. Photonic architectures are particularly promising, offering long coherence times and a natural means of encoding d-dimensional qudits in multi-port interferometers. Our two-qutrit Hilbert space can thus be realised using two three-mode interferometers, preserving the essential tensor-product structure between states and operators. Each operator can be diagonalised via the qutrit Fourier gate U_{QFT}, confining their non-unitary action to diagonal components $\mathcal{D}_i$ This reduces

the conditional action on the qutrit basis to controlled operations between mode pairs, for which explicit circuits were constructed using linear optical elements and a single non-linear gate built from the NS gates of the KLM protocol. While the probabilistic nature of these gates limits scalability, for our purposes this challenge can be overcome through sufficient repetition of the constructed circuits.

While photonic platforms are, in principle, capable of implementing high-fidelity two-qutrit operations [202, 203, 204, 205], they remain vulnerable to various sources of noise, including decoherence and mode mismatch. Remarkably, the analysis given in Section 5, reveals an inherent robustness of our encoding against these physically relevant sources of error. Specifically, when subject to noise in the form of decoherence, the operation of $(R^{GG})^2$ encoded on two physical qutrits is shown to consistently outperform the conventional logical encoding on a single qutrit across all error probabilities. The F gate similarly exhibits an enhanced average resilience against decoherence, provided that the probability of error remains below a defined threshold. This observed form of robustness is distinct from the topological protection inherently owed to anyonic models, the existence of which has already been demonstrated for encodings of various anyonic models [110, 219]. Whether similar forms of passive error suppression arise in simulations of other non-Abelian quantum double models remains an open question for further investigation.

Chapter 6

Conclusions

In this thesis, we have explored the use of lattice models as powerful tools for simulating and harnessing quantum correlations as resources for computation. By focusing on analytically solvable models in both one and two dimensions, we gained rare insight into the emergent behaviour of complex quantum systems and how such behaviour can be controlled for practical advantage. In one dimension, this enabled exact characterisation and tuning of correlation structures, while in two dimensions, it provided a topologically protected setting in which non-Abelian braiding operations were shown to generate the magic states required for universal quantum computation. Crucially, we further demonstrated that these ideas can be distilled into minimal encodings compatible with current experimental platforms, highlighting a clear pathway from theoretical models to physical realisation.

In Chapter 2, we investigated one of the central quantities at the heart of quantum mechanics: entanglement. The ability to coherently tune entanglement correlations is of crucial importance for near-term quantum technologies, where tasks such as quantum simulation, error correction, and information transfer rely on engineering precise correlation patterns. Among the available diagnostics, the entanglement spectrum plays a particularly important role, as it encodes not only the strength but also the structure of quantum correlations in many-body systems. In this context, we introduced the q-

deformed rainbow model, which acts as a precise universal simulator for free-particle entanglement energies, thereby yielding exact control over the quantum correlations in a one-dimensional spin chain.

In particular, we introduced a local Hamiltonian on $2N$ sites with nearest-neighbour couplings and asymmetric magnetic field terms about the chain centre. Using a Real-Space Renormalization Group approach, we showed that when these terms decay exponentially from the centre, the model admits an exact ground state even in the thermodynamic limit. This q-deformed rainbow state consists of concentric $SU(2)_q$ singlets, each characterised by a deformation parameter q_i set by the Hamiltonian's physical parameters. Analysis of its entanglement structure revealed that these deformation parameters naturally capture the correlations of the tensor-product ground state, directly linking entanglement properties to tunable model parameters. In this way, the derivation of a set of recursive identities allowed us to express the single-particle entanglement energies in terms of the couplings and transverse fields, yielding precise analytical control over the full entanglement spectrum.

To verify the validity of our results we perform a detailed numerical analysis. This analysis revealed that with appropriate choices of the transverse field parameter, and ordering of the degree of entanglement one ensures a high fidelity between the exact ground state and the q-deformed rainbow. To further illustrate the versatility of our method, we examined two special cases. The first is the homogeneous case, $q_1 = q_2 = \cdots = q_N$, where all concentric pairs share the same degree of entanglement, thus generalising the concentric singlet structure of the rainbow chain introduced in [41] to arbitrary entanglement strengths. Secondly, we introduced a prime number spectrum devised by Germán Sierra, where single-particle entanglement energies scale with the logarithm of the primes. Here, the density matrix eigenvalues map directly onto square-free integers, revealing an elegant connection between the decomposition of entanglement spectra and the prime factorization of integers.

The tunable correlation structure of the q-deformed rainbow renders it a versatile

framework both for engineering desired entanglement patterns for quantum information and for probing a range of phenomena in quantum many-body systems. Drawing on the foundation laid by the original rainbow state model of Vitagliano et al. [41], one sees a variety of future research directions in terms of entanglement dynamics under quenches, extensions to higher-dimensional lattices, and connections to symmetry-protected topological phases. An especially intriguing application is motivated by recent efforts to emulate black hole physics in condensed-matter systems. In particular, it has been shown that Hawking radiation and the fast scrambling properties characteristic of black holes can be captured by chiral spin-chain models [228, 229]. Traditionally, scrambling has been studied through the growth of out-of-time-ordered correlators of entangled pairs. The q-deformed rainbow ground state thus provides an analytically tractable platform in which the tunable deformation parameters offer direct control over the degree of entanglement of a number of such pairs, enabling systematic investigation of scrambling behaviour. Such a framework has potential implications for quantum information processing, where controllable scrambling dynamics may serve as a resource for secure communication protocols and as a probe of quantum chaos [230, 231, 232, 233, 234]. A detailed exploration of these possibilities is left as an open problem.

In Chapter 4, we turned to strongly correlated two-dimensional systems, where global entanglement structures in topologically ordered phases give rise to exotic quasiparticles known as anyons. These quasiparticles have attracted significant attention due to the prospect that their controlled manipulation could provide a model for quantum computation that is intrinsically robust against environmental noise. Within this context, we employed Kitaev's quantum double model as a framework to simulate the fundamental operations of non-Abelian anyons on a lattice of $d = 6$ qudits. Through this approach, we reconstructed the unitary braiding evolutions that underpin their computational power and demonstrated conclusively their ability to generate magic states, an essential resource for universal quantum computation.

Specifically, we considered the quantum double model $\mathbf{D}(\mathbf{S}_3)$, the simplest framework

hosting non-Abelian anyons. Within this setting, we developed a protocol that uses projective charge measurements on a $d = 6$ lattice to coherently construct states in the logical fusion basis. By varying the order of overlapping ribbon operators, we simulated both the braiding transformations encoded in the R matrix and the fusion-basis changes described by the F matrix. While charge conservation imposes a restriction leading to squared F-matrix elements, the resulting braiding operators nevertheless conclusively implement a logical non-Clifford gate. Acting on a qubit encoded in $\{|A\rangle, |B\rangle\}$, this unitary braiding was shown to generate states with non-zero stabilizer Rényi entropy, providing a direct demonstration of their role as a universal quantum computational resource.

Such magic states play a pivotal role in extending topological quantum computing schemes to full universality. While braiding operations of Abelian anyons provide fault-tolerant implementations of Clifford gates, these operations remain efficiently simulable on classical hardware and are therefore insufficient for universal quantum computation. Universality is achieved when such braiding is supplemented by the generation of non-Clifford resources in the form of magic states, which can be injected to enable gates such as the T-gate [235, 236, 237]. This principle underlies several proposals, including that of Laubscher et al. [172], where magic states generated from non-Abelian degrees of freedom are used to augment more experimentally accessible Abelian braiding operations within the surface code. By explicitly demonstrating the realisation of non-Clifford braiding operations within a topologically protected framework, our protocol represents an important step towards the practical implementation of universal, fault-tolerant quantum computation. The explicit integration of these non-Abelian braiding operations into a larger computational architecture remains an interesting open questions for future research.

Finally, we emphasise the minimal nature of this protocol, which is crucial for practical implementation. Firstly, the construction relies on anyonic creation operators acting along the shortest proper ribbons required for generating non-Abelian dyons. These rib-

bons are chosen such that each produces a pair of anyons with one located on a common vertex v, ensuring that a single vertex projection operator is sufficient to select a desired fusion outcome. This reduction is particularly valuable in experimental contexts, where the probabilistic character of measurements necessitates extensive post-selection across many trials. Moreover, the static nature of the protocol circumvents the need for complex, controlled dynamical evolutions of anyons, instead realising braiding algebraically through the ordered application of a reduced operator set. As such, this minimal protocol for the simplest non-Abelian model provides a key step in bridging the abstract algebraic description of non-Abelian braiding with the concrete procedures required for their exploitation in physical implementations.

In Chapter 5 of this thesis, we demonstrated that the non-Clifford braiding operations of $\mathbf{D}(\mathbf{S}_3)$ anyons can be realised in a physically implementable, noise-resilient manner using photonic simulators, representing an important bridge between the abstract algebra of non-Abelian anyons and the concrete experimental procedures required to harness them for universal, fault-tolerant quantum computation.

To adapt the scheme in Chapter 4 to the capabilities of current quantum technologies, in Section 5.3, we developed a dense encoding scheme based on the single-plaquette ground state and its associated operators. In particular, for this minimal physical system the non-trivial action of all operators reduces to just two qudits, revealing a tensor-sum structure tied to the the semi-direct product structure $\mathbf{S}_3 \cong \mathbf{Z}_3 \rtimes \mathbf{Z}_2$. The vanishing action on the elements $\{t, tc, tc^2\}$ shows that the essential dynamics of the $\{A, B, G\}$ sub-model are fully captured within an effective qutrit basis $\mathbf{Z}_3 \cong \{e, c, c^2\}$. Although simplified relative to the full quantum double formalism, tomographic analysis (Appendix D.2) confirmed that these reduced operators retain the defining properties of anyonic operations. Furthermore, decomposition of the operator products revealed a cancellation of flux non-conserving terms, enabling the elements of the R and F matrices required to derive the braiding operations, to be computed directly from inner products of the two-qutrit operators with respect to the product state $|\xi\rangle$.

This reduction is important not only for the experimental verification of non-Clifford braiding operations, but also for enabling scalability in the realisation of multiple logical anyonic states within larger lattices. In particular, the schemes of Cui et al. [147] and Mochon [238], explore these logical states as the basis for the construction of a universal gate set for $\mathbf{D}(\mathbf{S}_3)$ anyons. The explicit encoding of logical qutrit states corresponding to the fusion space of four non-Abelian G anyons thus provides a concrete foundation for the minimal construction of such topologically protected states, with direct potential for extension to experimentally feasible implementations of these universal computational schemes.

To demonstrate experimental feasibility, in Section 5.4 we presented a linear optical circuit design, developed by Matthew Horner, for implementing the reduced ribbon and projection operators. In this setting, the required non-unitary operations are realised using linear optical elements together with measurement-induced nonlinearities within the Knill–Laflamme–Milburn framework. Although such non-linear gates are inherently probabilistic, their action can be reliably incorporated through repeated trials and post-selection, providing a concrete route to realising non-Abelian anyonic operations in photonic systems. We emphasise, however, that the versatility of the minimal dense encoding scheme renders it accessible to a range of alternative qudit-based architectures. For example, trapped-ion platforms can naturally encode multi-level systems in internal electronic states with high-fidelity entangling gates [239, 240] while superconducting circuits can access higher transmon levels to realise effective qutrits with fast control [202, 241, 242]. Each of these alternatives offers complementary advantages for scalability and control, underscoring the versatility of our approach.

Finally, detailed error analysis of this protocol revealed an inherent robustness of our encoding to physically relevant noise sources, including decoherence and mode mismatch. We showed that the reconstructed braiding operators, such as $(R^{GG})^2$ exhibit enhanced resilience compared with conventional encodings, with performance consistently surpassing gate-based approaches below a defined noise threshold. This resilience arises not from

active error correction, but from a passive protective mechanism rooted in the structure of the encoding itself. The manifestation of this passive complementary mechanism for error suppression in other simulations of non-Abelian quantum double models remains an interesting open question for further research.

Appendix A

Supplementary material for Chapter 2

A.1 Entanglement spectra for free systems

Consider a spin-$\frac{1}{2}$ Hamiltonian equivalent to a free fermion Hamiltonian of the form (2.13) under a Jordan-Wigner transformation. Such a Hamiltonian is described as 'non-interacting' as the component terms are at most quadratic in terms of mode operators, and thus unable to describe interactions between fermions. The corresponding ground state, $|\psi\rangle$, is a Gaussian state with two-point correlators computed from the overlaps

$$C_{i,j} = \langle\psi| c_i^\dagger c_j |\psi\rangle . \tag{A.1}$$

Wick's theorem [243, 244] dictates that all higher-order correlations are decomposable as products of these two-point-correlators. This in turn implies that the many-body density matrix $\rho = |\psi\rangle \langle\psi|$ is entirely defined by the elements of the correlation matrix C_{ij}.

Consider now the reduced density matrix over sites $1, \ldots, L$, labelled ρ_A. The expectation values of all operators acting completely within this subsystem may be reproduced

with respect to this reduced density matrix. For example, the two-point correlators

$$C_{A,ij} = \mathrm{Tr}(\rho_A c_i^\dagger c_j). \tag{A.2}$$

By definition, these correlators across all sites within subsystem A are identical to those of the full system

$$C_{A,ij} = C_{ij}, \quad 1 \leq i, j \leq L. \tag{A.3}$$

Thus Wick's theorem still holds for the decomposition of all higher-order correlators acting within this subsystem. According to this theorem, this property holding implies that ρ_A is equivalent to the exponential of a free-fermion operator

$$\rho_A = \frac{1}{Z} e^{-\mathcal{H}_{\mathrm{ent}}} = \frac{1}{Z} e^{-\sum_{m=1}^{L} \epsilon_m f_m^\dagger f_m} \tag{A.4}$$

where the f_m's are related to the original c_i operators in the subsystem by canonical transformation, the normalization factor $\frac{1}{Z}$ ensures that $\mathrm{Tr}(\rho_A) = 1$ and the energies ϵ_m are related to the eigenvalues of C_A, $\nu_m \in [0, 1]$ by

$$\nu_m = \frac{1}{e^{\epsilon_m} + 1}. \tag{A.5}$$

A.2 q-deformed algebras

The algebra $SU(2)_q$ describes a q-deformation of the Lie algebra $\mathfrak{su}(2)$, parametrised by the complex deformation parameter $q \in \mathbb{C}\backslash\{0\}$. Here we briefly outline the defining features of these quantum groups, which have seen a wide range of applications within both physics and mathematics.

The undeformed $\mathfrak{su}(2)$ algebra is a three-dimensional simple Lie algebra spanned by the generators j_+, j_-, j_z obeying the commutation relations

$$[j_z, j_\pm] = \pm j_\pm, \quad [j_+, j_-] = 2j_z, \tag{A.6}$$

and providing the algebraic structure underlying the representation theory of angular momentum and spin in quantum mechanics [245]. The q-deformation of this algebra modifies these commutators as [246, 247]

$$[J_z, J_\pm] = \pm J_\pm, \qquad [J_+, J_-] = \frac{q^{2J_z} - q^{-2J_z}}{q - q^{-1}} = [2J_z]_q \tag{A.7}$$

where $[n]_q$ is the quantum dimension defined as

$$[n]_q \equiv \frac{q^n - q^{-n}}{q - q^{-1}}. \tag{A.8}$$

As $q \to 1$, $[n]_q \to n$ and one regains the standard $\mathfrak{su}(2)$ Lie algebra. Note that these quantum groups are distinct from groups in the technical sense, as the generators (A.7) no longer form a valid Lie algebra.

These quantum groups first gained particular attention when it was discovered that solutions to the Yang–Baxter equation (see Equation (3.5)) give rise to algebraic structures interpretable as deformations of classical Lie algebras [248, 249, 250]. These deformed Lie algebras have since found a diverse range of applications across multiple areas of physics, arising naturally in contexts where symmetry is modified by underlying quantum or topological constraints [120, 251, 252]. For example, in integrable models such as the XXZ spin chain, the q-deformed algebra encodes the symmetry underlying exact solvability, with its structure emerging directly from solutions of the Yang–Baxter equation [253, 254, 255].

A.3 q-deformed model four site perturbation theory

In order to illustrate the Real-Space RG approach, we apply perturbation theory to the Hamiltonian (2.27) restricted to a chain of four sites

$$\mathcal{H} = \mathcal{H}_{(1)} + \lambda V, \tag{A.9}$$

where

$$\mathcal{H}_{(1)} = J_1(\sigma^x_{-1}\sigma^x_1 + \sigma^y_{-1}\sigma^y_1) + h_1(\sigma^z_{-1} - \sigma^z_1), \tag{A.10}$$

is our original two-spin model and

$$V = J'_2(\sigma^x_{-2}\sigma^x_{-1} + \sigma^y_{-2}\sigma^y_{-1} + \sigma^x_1\sigma^x_2 + \sigma^y_1\sigma^y_2) + h'_2(\sigma^z_{-2} - \sigma^z_2). \tag{A.11}$$

Here the couplings $J_2 = \lambda J'_2$ and $h_2 = \lambda h'_2$, such that for any $\lambda \ll 1$, the perturbative condition $J_2, h_2 \ll J_1, h_1$ is ensured.

On two sites, $\mathcal{H}_{(1)}$ has the following eigenstates

$$|\psi^-_{q_1}\rangle = \frac{1}{\sqrt{[2]_{q_1}}}\left(q_1^{-\frac{1}{2}}\,|\uparrow\downarrow\rangle - q_1^{\frac{1}{2}}\,|\downarrow\uparrow\rangle\right), \tag{A.12}$$

$$|\psi^0\rangle = |\uparrow\uparrow\rangle\,, \tag{A.13}$$

$$|\psi^1\rangle = |\downarrow\downarrow\rangle\,, \tag{A.14}$$

$$|\psi^+_{q_1}\rangle = \frac{1}{\sqrt{[2]_{q_1}}}\left(q_1^{\frac{1}{2}}\,|\uparrow\downarrow\rangle + q_1^{-\frac{1}{2}}\,|\downarrow\uparrow\rangle\right), \tag{A.15}$$

with eigenenergies $E_1 = -[2]_{q_1}J_1, E_s = 0, E_t = 0$ and $E_k = +[2]_{q_1}J_1$ respectively, and q_1 as previously defined in equation (2.23).

When extended to a chain of four spins, the ground state subspace of $\mathcal{H}_{(1)}$ becomes four-fold degenerate. We represent this subspace with the basis vectors: $\{|m\rangle\} = \{|m_1\rangle\,, |m_2\rangle\,, |m_3\rangle\,, |m_4\rangle\} = \{|\uparrow\rangle_{-2}\,|\psi^-_{q_1}\rangle_{-1,1}\,|\uparrow\rangle_2,\ |\uparrow\rangle_{-2}\,|\psi^-_{q_1}\rangle_{-1,1}\,|\downarrow\rangle_2,\ |\downarrow\rangle_{-2}\,|\psi^-_{q_1}\rangle_{-1,1}\,|\uparrow\rangle_2\,,\ |\downarrow\rangle_{-2}\,|\psi^-_{q_1}\rangle_{-1,1}\,|\downarrow\rangle_2\}$. The first-order corrections arise due to the action of the perturbative term on the ground state subspace. This is quantified via the computation of the matrix elements of the effective Hamiltonian to first order

$$\mathcal{H}^{eff(1)}_{\alpha,\beta} = \langle m_\alpha|\,V\,|m_\beta\rangle\,, \tag{A.16}$$

yielding

$$\mathcal{H}^{eff(1)} = 2h_2' \begin{pmatrix} 0 & 0 & 0 & 0 \\ 0 & 1 & 0 & 0 \\ 0 & 0 & -1 & 0 \\ 0 & 0 & 0 & 0 \end{pmatrix} \tag{A.17}$$

in the basis $\{|m\rangle\}$. By inspection, it can be seen that the first-order effective Hamiltonian term is therefore $\mathcal{H}^{eff(1)} = h_2'(\sigma_{-2}^z - \sigma_2^z)$. The first-order ground state energy correction is found by diagonalizing the above matrix. It is clear that the degeneracy is only partially lifted to first order. It is therefore necessary to consider the second order corrections that arise due to the overlap with states from each of the excited state subspaces. These excited state subspaces are found in the same way as the set $\{|m\rangle\}$ by taking the tensor product of the two-qubit computational basis with the excited eigenstates of $H_{(1)}$: $\{|s\rangle\} = \{|s_1\rangle, |s_2\rangle, |s_3\rangle, |s_4\rangle\} = \{|\uparrow\uparrow\uparrow\uparrow\rangle,\ |\uparrow\uparrow\uparrow\downarrow\rangle,\ |\downarrow\uparrow\uparrow\uparrow\rangle,\ |\downarrow\uparrow\uparrow\downarrow\rangle\}$, $\{|t\rangle\} = \{|t_1\rangle, |t_2\rangle, |t_3\rangle, |t_4\rangle\} = \{|\uparrow\downarrow\downarrow\uparrow\rangle,\ |\uparrow\downarrow\downarrow\downarrow\rangle,\ |\downarrow\downarrow\downarrow\uparrow\rangle,\ |\downarrow\downarrow\downarrow\downarrow\rangle\}$, $\{|k\rangle\} = \{|k_1\rangle, |k_2\rangle, |k_3\rangle, |k_4\rangle\} = \{|\uparrow\rangle_{-2} |\psi_{q_1}^+\rangle_{-1,1} |\uparrow\rangle_2,\ |\uparrow\rangle_{-2} |\psi_{q_1}^+\rangle_{-1,1} |\downarrow\rangle_2,\ |\downarrow\rangle_{-2} |\psi_{q_1}^+\rangle_{-1,1} |\uparrow\rangle_2,\ |\downarrow\rangle_{-2} |\psi_{q_1}^+\rangle_{-1,1} |\downarrow\rangle_2\}\}$. Such that the full set of excited states, $\{|n\rangle\} = \{\{|s\rangle\}, \{|t\rangle\}, \{|k\rangle\}\}$.

The matrix elements of the effective Hamiltonian to second-order are found from

$$\mathcal{H}_{\alpha,\beta}^{eff(2)} = \sum_{i=1} \frac{\langle m_\alpha | V | n_i \rangle \langle n_i | V | m_\beta \rangle}{E_- - E_i}. \tag{A.18}$$

The computation of which yields

$$\mathcal{H}^{eff(2)} = \frac{(2J_2')^2}{(1+q_1^2)E_1} \begin{pmatrix} 1+q_1^2 & 0 & 0 & 0 \\ 0 & 2q_1^2 & -2q_1 & 0 \\ 0 & -2q_1 & 2 & 0 \\ 0 & 0 & 0 & 1+q_1^2 \end{pmatrix}. \tag{A.19}$$

Combining our first and second-order perturbative terms we derive an expression for

the effective Hamiltonian correct to $\mathcal{O}(\lambda^2)$

$$\mathcal{H}^{eff} \approx E_1 \mathbf{1}_4 + \lambda \mathcal{H}^{eff(1)} + \lambda^2 \mathcal{H}^{eff(2)} \tag{A.20}$$

$$= \left(E_1 + \frac{(2\lambda J_2')^2}{E_1} \right) \mathbf{1}_4 \tag{A.21}$$

$$- \frac{q_1 (2\lambda J_2')^2}{(1+q_1^2) E_1} (\sigma_{-2}^x \sigma_2^x + \sigma_{-2}^y \sigma_2^y)$$

$$+ \left(\lambda h_2' - \frac{2(1-q_1^2)(\lambda J_2')^2}{(1+q_1^2) E_1} \right) (\sigma_{-2}^z - \sigma_2^z)$$

$$= \mathcal{C} \mathbf{1}_4 + \tilde{J}_2 (\sigma_{-2}^x \sigma_2^x + \sigma_{-2}^y \sigma_2^y) + \tilde{h}_2 (\sigma_{-2}^z - \sigma_2^z) \tag{A.22}$$

In this way we obtain the following expressions for our renormalized parameters

$$\tilde{J}_2 = \frac{4 J_2^2}{[2]_{q_1}^2 J_1}, \tag{A.23}$$

$$\tilde{h}_2 = h_2 - \frac{2 \left(q_1 - \frac{1}{q_1} \right) J_2^2}{[2]_{q_1}^2 J_1}. \tag{A.24}$$

Note that, in the case $h_1 = h_2 = 0$ such that $q_1 = q_2 = 1$, $\tilde{h}_2$ vanishes and $\tilde{J}_2$ returns to that of the inhomogeneous XX model re-scaling as seen in equation (2.30) as expected.

Diagonalization of the effective Hamiltonian yields the ground state

$$|\psi\rangle = \frac{1}{\sqrt{[2]_{q_2}}} \left(q_2^{-\frac{1}{2}} |m_2\rangle - q_2^{\frac{1}{2}} |m_3\rangle \right) \tag{A.25}$$

$$= \left(\frac{1}{\sqrt{[2]_{q_1}}} (q_1^{-\frac{1}{2}} |\uparrow\downarrow\rangle_{-1,1} - q_1^{\frac{1}{2}} |\downarrow\uparrow\rangle_{-1,1}) \right) \tag{A.26}$$

$$\otimes \left(\frac{1}{\sqrt{[2]_{q_2}}} (q_2^{-\frac{1}{2}} |\uparrow\downarrow\rangle_{-2,2} - q_2^{\frac{1}{2}} |\downarrow\uparrow\rangle_{-2,2}) \right)$$

with corresponding ground state energy

$$E_2 = E_1 - \frac{4 J_2^2}{[2]_{q_1} J_1} + \tilde{E}_2, \tag{A.27}$$

where

$$\tilde{E}_2 = -[2]_{q_2}\tilde{J}_2. \tag{A.28}$$

A.4 Relationship Between Real Model Parameters and Single-Particle Entanglement Energies

In Section 2.4.2 the following relationship was found between the renormalised coupling parameters and single-particle entanglement energies

$$\frac{\tilde{h}_i}{\tilde{J}_i} = -\sinh\left(\frac{\epsilon_i}{2}\right).$$

By combining this relation with equations (2.37) and (2.38), we can obtain expressions that directly relate the desired single-particle entanglement energies to the required ratio of real parameters in our model. The recursive nature of the formulae for the re-scaled parameters means that in order to engineer some single-particle energy, ϵ_i, it is necessary to have previously established some value for all previous $i-1$ energies.

In the strong inhomogeneity case $J_1, h_1 \gg J_{i\neq 1}, h_{i\neq 1}$ that we consider, the central terms J_1 and h_1 do not get re-scaled, therefore simply

$$h_1 = -J_1 \sinh\left(\frac{\epsilon_1}{2}\right), \tag{A.29}$$

for some desired single-particle energy, ϵ_1, and fixed value of the central coupling term. In Appendix A.3 we have found exact expressions for the renormalized parameters $\tilde{J}_2$ and $\tilde{h}_2$. By substituting these into (2.48) and fixing all other parameters, we obtain an expression for the required transverse field

$$h_2 = -\frac{J_2^2}{\cosh^2\left(\frac{\epsilon_1}{2}\right)J_1}\left[\sinh\left(\frac{\epsilon_2}{2}\right) + \sinh\left(\frac{\epsilon_1}{2}\right)\right]. \tag{A.30}$$

Repated iterations of this process yield a general form for the required transverse field

parameter for any pair of sites $-i$ and i, when $i > 2$

$$h_{i>2} = \frac{J_i^2}{\cosh^2\left(\frac{\epsilon_{i-1}}{2}\right) h_{i-1}} \left[\sinh\left(\frac{\epsilon_i}{2}\right) + \sinh\left(\frac{\epsilon_{i-1}}{2}\right)\right] \times \left[\sinh\left(\frac{\epsilon_{i-1}}{2}\right) + \sinh\left(\frac{\epsilon_{i-2}}{2}\right)\right]. \quad \text{(A.31)}$$

Thus, it is made explicit how the real parameters of our model can be selected such as to produce any desired set of single-particle entanglement energies.

A.5 Analytic Fidelity for $N = 2$

Here we present an analytic expression for the fidelity between the ground state of the model (2.27) and our q-deformed rainbow for the case $N = 2$. The Hamiltonian $\mathcal{H}_{(N=2)}$ is a function of four parameters J_1, J_2, h_1 and h_2. With a re-ordering of the basis states the associated 24×24 matrix takes on a block diagonal form with the largest 6×6 sub-matrix yielding the unique ground state of the form,

$$|GS\rangle_{\text{ex}} = \mathcal{N}(a\,|\uparrow\uparrow\downarrow\downarrow\rangle + b\,|\uparrow\downarrow\uparrow\downarrow\rangle + c\,(|\uparrow\downarrow\downarrow\uparrow\rangle + |\downarrow\uparrow\uparrow\downarrow\rangle) + d\,|\downarrow\uparrow\downarrow\uparrow\rangle + e\,|\downarrow\downarrow\uparrow\uparrow\rangle) \quad \text{(A.32)}$$

where $\mathcal{N}$ is the appropriate normalization factor. Choosing $a = 1$ the other co-efficients are related to our variable parameters in the following way

$$b = \frac{1}{J_1}\left(\frac{\lambda}{2} - (h_1 + h_2)\right), \quad \text{(A.33)}$$

$$c = \frac{1}{2J_2}\left[\left(\frac{\lambda}{2} + (h_1 - h_2)\right) b - J_1\right], \quad \text{(A.34)}$$

$$d = \frac{\lambda}{2J_2} c - b, \quad \text{(A.35)}$$

$$e = \frac{J_1 d}{\left(\frac{\lambda}{2} + (h_1 + h_2)\right)}, \quad \text{(A.36)}$$

where $\lambda = -2\sqrt{u + 2\sqrt{v}}$ is the exact ground state energy with $u = h_1^2 + h_2^2 + J_1^2 + 2J_2^2$ and $v = (h_1 h_2 - J_2^2)^2 + h_2^2 J_1^2$.

Using equation (2.34), our q-deformed rainbow ground state on four sites has the form

$$|GS\rangle_q = \frac{1}{\sqrt{[2]_{q_1}}} \left(q_1^{-\frac{1}{2}} |\uparrow\downarrow\rangle_{-1,1} - q_1^{\frac{1}{2}} |\downarrow\uparrow\rangle_{-1,1} \right) \tag{A.37}$$

$$\otimes \frac{1}{\sqrt{[2]_{q_2}}} \left(q_2^{-\frac{1}{2}} |\uparrow\downarrow\rangle_{-2,2} - q_2^{\frac{1}{2}} |\downarrow\uparrow\rangle_{-2,2} \right)$$

$$= \frac{1}{\sqrt{[2]_{q_1}[2]_{q_2}}} \left(q_1^{-\frac{1}{2}} q_2^{-\frac{1}{2}} |\uparrow\uparrow\downarrow\downarrow\rangle - q_1^{\frac{1}{2}} q_2^{-\frac{1}{2}} |\uparrow\downarrow\uparrow\downarrow\rangle \right.$$

$$\left. - q_1^{-\frac{1}{2}} q_2^{\frac{1}{2}} |\downarrow\uparrow\downarrow\uparrow\rangle + q_1^{\frac{1}{2}} q_2^{\frac{1}{2}} |\downarrow\downarrow\uparrow\uparrow\rangle \right). \tag{A.38}$$

The ground state fidelity that we use to quantify the accuracy of our method is defined as the squared overlap between the exact and q-deformed ground state

$$\text{Fidelity} = |\langle GS|_{ex} |GS\rangle_q|^2 \tag{A.39}$$

$$= |\frac{\mathcal{N}}{\sqrt{[2]_{q_1}[2]_{q_2}}} \left(\frac{a}{\sqrt{q_1 q_2}} - b\sqrt{\frac{q_1}{q_2}} - e\sqrt{\frac{q_2}{q_1}} + f\sqrt{q_1 q_2} \right)|^2. \tag{A.40}$$

Thus for some desired pair of single-particle energies $\{\epsilon_1, \epsilon_2\}$, with a choice of coupling profile for J_1 and J_2, q_1, q_2, h_1 and h_2 can be found and substituted into (A.40) to determine an exact value for the fidelity.

Appendix B

Supplementary material for Chapter 3

B.1 Quantum Dimension of Anyons

One may define the n^{th}-order fusion between n a-type anyons as $a^{[\times n]}$, such that $a^{[\times 2]} \equiv a \times a$, $a^{[\times 3]} \equiv a \times a \times a$ and so on. The dimensionality of such a fusion product $\dim(a^{[\times n]})$ corresponds to the total number of distinct fusion channels available. From this the dimensionality of a single a-type anyon may be quantified by the growth of the fusion space with the addition of a singular a anyon in the large n limit. Explicitly

$$d_a = \lim_{n\to\infty} \frac{\dim(a^{[\times n+1]})}{\dim(a^{[\times n]})}. \tag{B.1}$$

Naturally, the singular fusion outcome of Abelian anyons yields $\dim(a^{[\times n]}) = 1$ for all n such that $d_a = 1$. Values $d_a > 1$ therefore correspond to non-Abelian anyons for which the fusion space with $\dim(a^{[\times n]})$ forms a multi-dimensional basis on which unitary braiding operations may act.

Consider for example the fusion relation for two G anyons

$$G^{[\times 2]} \equiv G \times G = A + B + G. \tag{B.2}$$

Increasing the order of the fusion product we obtain

$$G^{[\times 3]} = G \times (A + B + G) = G^{[\times 2]} + 2G \tag{B.3}$$

$$G^{[\times 4]} = G^{[\times 3]} + 2G^{[\times 2]} \tag{B.4}$$

and finally

$$G^{[\times n]} = G^{[\times n-1]} + 2G^{[\times n-2]}. \tag{B.5}$$

The dimensionality of the n^{th}-order fusion space $\dim(G^{[\times n]})$ corresponds to the total number of fusion channels available such that for example, $\dim(G^{[\times 2]}) = 3$, $\dim(G^{[\times 3]}) = 5$, $\dim(G^{[\times 4]}) = 11$ and in general we obtain the second-order recursive relation

$$\dim(G^{[\times n]}) = \dim(G^{[\times n-1]}) + 2 \cdot \dim(G^{[\times n-1]}). \tag{B.6}$$

From this the dimensionality of the G anyon may be quantified as

$$d_G = \lim_{n\to\infty} \frac{\dim(G^{[\times n+1]})}{\dim(G^{[\times n]})} \tag{B.7}$$

$$= \lim_{n\to\infty} \frac{\dim(G^{[\times n]}) + 2 \cdot \dim(G^{[\times n-1]})}{\dim(G^{[\times n]})} \tag{B.8}$$

$$= \lim_{n\to\infty} \left(1 + 2 \cdot \frac{\dim(G^{[\times n-1]})}{\dim(G^{[\times n]})}\right) \tag{B.9}$$

$$= 1 + 2 \cdot \frac{1}{d_G}. \tag{B.10}$$

Solving this quadratic equation and taking the positive solution therefore yields $d_G = 2$ as listed in Table 4.1.

B.2 Commutativity of Vertex and Plaquette Operators

First, consider a plaquette operator $B^e(p)$ and a vertex operator $A(v)$. In calculating the commutation relation between any two such operators, there are two distinct cases as shown in Figure B.1. In the first case, when both $A(v)$ and $B^e(p)$ act on two different

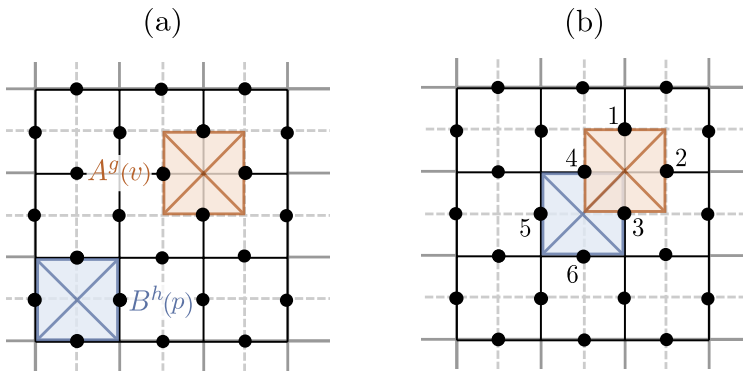

Figure B.1: (a) A four plaquette lattice with a vertex operator $A^g(v)$ and plaquette operator $B^h(p)$ acting on different qudits. (b) The same plaquette but with vertex and plaquette operators overlapping on two qudits 3 and 4.

sets of four qudits as in Fig.B.1(a), it is clear that they will necessarily commute. In the alternative non-trivial case where $A(v)$ and $B^e(p)$ 'overlap' and have non-trivial action on two of the same qudits on the lattice more care must be taken to demonstrate that these operators will commute.

Consider, for example, the operators $A(v)$ and $B^e(p)$ acting on the six qudits shown in Figure B.1. For the labeling as shown these operators have the following forms

$$\begin{aligned} A(v) &= \frac{1}{6}\sum_{g\in\mathbf{G}} \mathbf{1}\otimes\mathbf{1}\otimes L_+^g\otimes L_+^g\otimes L_-^g\otimes L_-^g, \\ B^e(p) &= \sum_{h_1h_2h_3h_4=e} T_+^{h_1}\otimes T_-^{h_2}\otimes T_-^{h_3}\otimes T_+^{h_4}\otimes\mathbf{1}\otimes\mathbf{1}. \end{aligned} \tag{B.11}$$

The action on all unlabelled qudits on this lattice is trivial and can thus be ignored.

In order to show that $[A(v), B^e(p)] \equiv A(v)B^e(p) - B^e(p)A(v) = 0$ we expand out the form of each of the products,

$$A(v)B^e(p) = \frac{1}{6}\sum_{g\in\mathbf{G}}\sum_{h_1h_2h_3h_4=e} T_+^{h_1}\otimes T_-^{h_2}\otimes L_+^gT_-^{h_3}\otimes L_+^gT_+^{h_4}\otimes L_-^g\otimes L_-^g \tag{B.12}$$

and

$$B^e(p)A(v) = \frac{1}{6}\sum_{g\in\mathbf{G}}\sum_{h_1h_2h_3h_4=e} T_+^{h_1}\otimes T_-^{h_2}\otimes T_-^{h_3}L_+^g\otimes T_+^{h_4}L_+^g\otimes L_-^g\otimes L_-^g. \tag{B.13}$$

In order to show that these two operators commute we refer to the commutation relations between the foundational $L_\pm^g$ and $T_\pm^h$ operators

$$L_+^gT_+^h = T_+^{gh}L_+^g, \quad L_-^gT_+^h = T_+^{hg^{-1}}L_-^g, \tag{B.14}$$

$$L_+^gT_-^h = T_+^{hg^{-1}}L_+^g, \quad L_-^gT_-^h = T_-^{gh}L_-^g, \tag{B.15}$$

as can be reproduced from the definitions of the action of $L_\pm^g$ and $T_\pm^h$ in Section 3.3. The commutation identities in (B.14) and (B.15) yield $L_+^gT_-^{h_3} = T_+^{h_3g^{-1}}L_+^g$ and $L_+^gT_+^{h_4} = T_+^{gh_4}L_+^g$ such that (B.12) becomes

$$A(v)B^e(p) = \frac{1}{6}\sum_{g\in\mathbf{G}}\sum_{h_1h_2h_3h_4=e} T_+^{h_1}\otimes T_-^{h_2}\otimes T_+^{h_3g^{-1}}L_+^g\otimes T_+^{gh_4}L_+^g\otimes L_-^g\otimes L_-^g. \tag{B.16}$$

Introducing the relabelling $h_1' = h_1$, $h_2' = h_2$, $h_3' = h_3g^{-1}$ and $h_4' = gh_4$, we note that this set of new variables retains the initial condition $h_1'h_2'h_3'h_4' = h_1h_2h_3g^{-1}gh_4 = h_1h_2h_3h_4 = e$ such that

$$A(v)B^e(p) = \frac{1}{6}\sum_{g\in\mathbf{G}}\sum_{h_1'h_2'h_3'h_4'=e} T_+^{h_1'}\otimes T_-^{h_2'}\otimes T_+^{h_3'}L_+^g\otimes T_+^{h_4'}L_+^g\otimes L_-^g\otimes L_-^g. \tag{B.17}$$

In this way each term in (B.17) exactly matches one in (B.13) and the commutativity condition $[A(v), B^e(p)] = 0$ is fulfilled. Crucially, for this and all other pairs of overlapping vertex and plaquette operators, this commutativity is ensured by choosing an orientation convention for the $L_\pm^g$ and $T_\pm^h$ operators such that one pair of $L_\pm^g$ and $T_\pm^h$ acting on the same qudit have the matching parity and the other have opposite parity. This ensures the condition $h_1'h_2'h_3'h_4' = e$ such that the two operators commute.

Similarly, for overlapping vertex (plaquette) operators, the $L_\pm^g$ ($T_\pm^h$) operators acting

on the single qudit point of overlap necessarily have opposite parity. For example, for the general case of two neighbouring vertex operators $A(v_i)$ and $A(v_j)$

$$[A(v_i), A(v_j)] \propto \sum_g \sum_h [L_{\pm}^g, L_{\mp}^h] = 0. \tag{B.18}$$

Appendix C

Supplementary material for Chapter 4

C.1 The $\{A, B, G\}$ Sub-Model

In this work, we restrict to the non-Abelian sub-group $\{A, B, G\}$ which is closed under fusion as seen in Equation (4.13). The irreps and character representations used in the construction of the ribbon operator creating pairs of these anyons as in (**??**) and (**??**) are detailed in Table C.1 [148].

Anyon	Irrep.	e	c	c^2	t	tc	tc^2
A	$\Gamma_1^{S_3}$	1	1	1	1	1	1
B	$\Gamma_{-1}^{S_3}$	1	1	1	-1	-1	-1
G	$\Gamma_{\omega}^{\mathbf{Z}_3}$	1	ω	$\bar{\omega}$	0	0	0

Table C.1: The irreducible representations of the submodel $\{A, B, G\}$ and the traces of their corresponding character irreducible representations.

Both Abelian anyons in our sub-model, $A : (\mathcal{C}_e = \{e\}, \Gamma_1^{\mathbf{S}_3})$ and $B : (\mathcal{C}_e, \Gamma_{-1}^{\mathbf{S}_3})$ in the $\mathbf{D}(\mathbf{S}_3)$ quantum double model correspond to the trivial conjugacy class $\mathcal{C}_e$ and are therefore chargeons residing on the vertices of the lattice. The simplest ribbon capable of producing a pair of such anyons is a single-qudit direct triangle $\rho = \tau$ as shown in Figure 4.4(a). The forms of the ribbon operators that create these pairs arise from the

substitution of this information into Equation (**??**) with the character representations of Table C.1. For example, for a pair of B anyons

$$F_\tau^B \equiv F_\tau^{\chi(\Gamma_{-1}^{\mathbf{S}_3}),e}, \tag{C.1}$$

$$= F_\tau^{e,e} + F_\tau^{e,c} + F_\tau^{e,c^2} - F_\tau^{e,t} - F_\tau^{e,tc} - F_\tau^{e,tc^2}, \tag{C.2}$$

$$= T_+^e + T_+^c + T_+^{c^2} - T_+^t - T_+^{tc} - T_+^{tc^2}, \tag{C.3}$$

where we have applied the identity $F_\tau^{g,h} := T_\tau^h$ for a direct triangle τ seen in Equation (3.23) and without loss of generality assumed that the triangle is facing along the oriented edge.

Similarly, for the non-Abelian anyons $G : (\mathcal{C}_c, \Gamma_\omega^{\mathbf{Z}_3})$ with irreducible representation as given in Table C.1, Equation (**??**) yields

$$F_\rho^G = F_\rho^{c,e} + \omega F_\rho^{c,c} + \bar{\omega} F_\rho^{c,c^2} + F_\rho^{c^2,e} + \bar{\omega} F_\rho^{c^2,c} + \omega F_\rho^{c^2,c^2}. \tag{C.4}$$

The G anyon is dyonic, such that any ribbon ρ along which this operator may be applied, must be composed of at least one dual and one direct triangle. For ribbons ρ_1 and ρ_2 of the form $\rho = \tau_{\text{direct}}\tau_{\text{dual}}$, Equation (3.24) is used to find the specific ribbon operators $F_{\rho_1}^G$ and $F_{\rho_2}^G$ given in Equations (4.25) and (4.26) respectively.

C.2 R matrix from ribbon operators

In Section 4.4.2 we have shown how the exchange matrix $(R^{GG})^2$, describing the braiding of two G anyons, may be reproduced with projective measurements onto states constructed by exchanging the order of the ribbon operators $F_{\rho_1}^G$ and $F_{\rho_2}^G$, replicating Equation 4.33. This result may also be verified with direct evaluation of the operator products $F_{\rho_1}^G F_{\rho_2}^G$ and $F_{\rho_2}^G F_{\rho_1}^G$ in the basis $\{e, c, c^2, t, tc, tc^2\}$. By comparing the form of each operator, the R matrix can then be determined in the anyonic basis $\{A, B, G\}$. Such an approach can be experimentally relevant when quantum operator tomography is avail-

able.

By representing the ribbons operators $F^G_{\rho_1}$ and $F^G_{\rho_2}$ fully in terms of their elements of the isolated two lattice sites they cross over, we can find all the elements of the crossed terms

$$
\begin{aligned}
F^G_{\rho_1}F^G_{\rho_2} &= \Big((T^e_- + \omega T^c_- + \bar{\omega}T^{c^2}_-) \otimes L^c_- + (T^e_- + \bar{\omega}T^c_- + \omega T^{c^2}_-) \otimes L^{c^2}_-\Big) \\
&\qquad \times \Big(L^c_+ \otimes (T^e_- + \omega T^c_- + \bar{\omega}T^{c^2}_-) + L^{c^2}_+ \otimes (T^e_- + \bar{\omega}T^c_- + \omega T^{c^2}_-)\Big), \\
&= \left(\sum_h \left(|e\rangle\langle e| + \bar{\omega}\,|c\rangle\langle c| + \omega\,|c^2\rangle\langle c^2|\right) \otimes |c^2h\rangle\langle h| + \left(|e\rangle\langle e| + \omega\,|c\rangle\langle c| + \bar{\omega}\,|c^2\rangle\langle c^2|\right) \otimes |ch\rangle\langle h|\right) \\
&\times \left(\sum_g |gc\rangle\langle g| \otimes \left(|e\rangle\langle e| + \bar{\omega}\,|c\rangle\langle c| + \omega\,|c^2\rangle\langle c^2|\right) + |gc^2\rangle\langle g| \otimes \left(|e\rangle\langle e| + \omega\,|c\rangle\langle c| + \bar{\omega}\,|c^2\rangle\langle c^2|\right)\right), \\
&= |e,c^2\rangle\langle c,e| + |e,c^2\rangle\langle c^2,e| + |e,c\rangle\langle c,e| + |e,c\rangle\langle c^2,e| + \omega\,|c^2,c^2\rangle\langle e,e| + \omega\,|c^2,c^2\rangle\langle c,e| \\
&+ \bar{\omega}\,|c^2,c\rangle\langle e,e| + \bar{\omega}\,|c^2,c\rangle\langle c,e| + \bar{\omega}\,|c,c^2\rangle\langle e,e| + \bar{\omega}\,|c,c^2\rangle\langle c^2,e| + \omega\,|c,c\rangle\langle e,e| + \omega\,|c,c\rangle\langle c^2,e| \\
&+ \omega\,|e,e\rangle\langle c,c| + \bar{\omega}\,|e,e\rangle\langle c^2,c| + \omega\,|e,c^2\rangle\langle c,c| + \bar{\omega}\,|e,c^2\rangle\langle c^2,c| + \bar{\omega}\,|c^2,e\rangle\langle e,c| + |c^2,e\rangle\langle c,c| \\
&+ |c^2,c^2\rangle\langle e,c| + \omega\,|c^2,c^2\rangle\langle c,c| + \omega\,|c,e\rangle\langle e,c| + |c,e\rangle\langle c^2,c| + |c,c^2\rangle\langle e,c| + \bar{\omega}\,|c,c^2\rangle\langle c^2,c| \\
&+ \bar{\omega}\,|e,c\rangle\langle c,c^2| + \omega\,|e,c\rangle\langle c^2,c^2| + \bar{\omega}\,|e,e\rangle\langle c,c^2| + \omega\,|e,e\rangle\langle c^2,c^2| + |c^2,c\rangle\langle e,c^2| + \bar{\omega}\,|c^2,c\rangle\langle c,c^2| \\
&+ \omega\,|c^2,e\rangle\langle e,c^2| + |c^2,e\rangle\langle c,c^2| + |c,c\rangle\langle e,c^2| + \omega\,|c,c\rangle\langle c^2,c^2| + \bar{\omega}\,|c,e\rangle\langle e,c^2| + |c,e\rangle\langle c^2,c^2|\,,
\end{aligned}
\tag{C.5}
$$

$$
\begin{aligned}
F^G_{\rho_2}F^G_{\rho_1} &= \omega\,|e,c^2\rangle\langle c,e| + \bar{\omega}\,|e,c^2\rangle\langle c^2,e| + \bar{\omega}\,|e,c\rangle\langle c,e| + \omega\,|e,c\rangle\langle c^2,e| + \bar{\omega}\,|c^2,c^2\rangle\langle e,e| + |c^2,c^2\rangle\langle c,e| \\
&+ \omega\,|c^2,c\rangle\langle e,e| + |c^2,c\rangle\langle c,e| + \omega\,|c,c^2\rangle\langle e,e| + |c,c^2\rangle\langle c^2,e| + \bar{\omega}\,|c,c\rangle\langle e,e| + |c,c\rangle\langle c^2,e| \\
&+ \bar{\omega}\,|e,e\rangle\langle c,c| + \omega\,|e,e\rangle\langle c^2,c| + |e,c^2\rangle\langle c,c| + |e,c^2\rangle\langle c^2,c| + |c^2,e\rangle\langle e,c| + \bar{\omega}\,|c^2,e\rangle\langle c,c| \\
&+ \bar{\omega}\,|c^2,c^2\rangle\langle e,c| + \bar{\omega}\,|c^2,c^2\rangle\langle c,c| + |c,e\rangle\langle e,c| + \omega\,|c,e\rangle\langle c^2,c| + \omega\,|c,c^2\rangle\langle e,c| + \omega\,|c,c^2\rangle\langle c^2,c| \\
&+ |e,c\rangle\langle c,c^2| + |e,c\rangle\langle c^2,c^2| + |e,e\rangle\langle c,c^2| + \bar{\omega}\,|e,e\rangle\langle c^2,c^2| + \omega\,|c^2,c\rangle\langle e,c^2| + \omega\,|c^2,c\rangle\langle c,c^2| \\
&+ |c^2,e\rangle\langle e,c^2| + \omega\,|c^2,e\rangle\langle c,c^2| + \bar{\omega}\,|c,c\rangle\langle e,c^2| + \bar{\omega}\,|c,c\rangle\langle c^2,c^2| + |c,e\rangle\langle e,c^2| + \bar{\omega}\,|c,e\rangle\langle c^2,c^2|\,.
\end{aligned}
\tag{C.6}
$$

Comparing these two expressions, we find that the elements of $F^G_{\rho_2}F^G_{\rho_1}$ gain an additional

phase relative to those of $F^G_{\rho_1}F^G_{\rho_2}$ according to the following prescription

$$|g_1,g_2\rangle\langle h_1,h_2| \to \begin{cases} \bar{\omega}\,|g_1,g_2\rangle\langle h_1,h_2| & \text{if } g_1g_2 = h_1h_2 \\ \omega\,|g_1,g_2\rangle\langle h_1,h_2| & \text{otherwise.} \end{cases} \tag{C.7}$$

To re-interpret this result into the anyonic basis as in (4.14), we consider the flux these ribbon operator products create on the shared plaquette, p. As the vacuum state is stabilised by the projector $B^e(p)$ it has trivial flux. As a result it consists of a superposition over all group elements for which $h_1h_2h_3h_4 = e$ on that plaquette. Under the action of $|g_1,g_2\rangle\langle h_1,h_2|$, if $g_1g_2 = h_1h_2$, then the condition $g_1g_2h_3h_4 = e$ is preserved. This condition corresponds to the fusion outcomes A and B that have trivial flux, that gain a factor $\bar{\omega}$, as seen from (C.7). When $g_1g_2 \neq h_1h_2$, then $g_1g_2h_3h_4 \neq e$ and the two ribbons have fused to produce a pair of G anyons with non-trivial flux. As seen from (C.7), this fusion outcome acquires a phase factor ω as in the final diagonal element of (4.14).

C.3 Analytics for F matrix

We will now present the main calculations for the amplitudes that determine the elements of the F matrix squared. By taking the inner products of our ribbon fusion states as in (4.49), we find that for each combination $i,j = A,B,G$ a phase factor may be extracted,

$$\begin{aligned} \langle\psi_2(j)|\psi_1(i)\rangle &= \langle\zeta|\left(A^G(v)F^G_{\rho_1}A^j(v)F^G_{\rho_2}F^G_{\rho_2}\right)^\dagger A^G(v)F^G_{\rho_2}A^i(v)F^G_{\rho_2}F^G_{\rho_1}|\zeta\rangle\,, && \text{(C.8)}\\ &= \langle\zeta|\,(F^G_{\rho_2})^2A^j(v)F^G_{\rho_1}A^G(v)F^G_{\rho_2}A^i(v)F^G_{\rho_2}F^G_{\rho_1}|\zeta\rangle\,, && \text{(C.9)}\\ &= \langle\zeta|\,F^j_{\rho_2}F^G_{\rho_1}A^G(v)A^G(v)F^G_{\rho_2}A^i(v)F^G_{\rho_2}F^G_{\rho_1}|\zeta\rangle\,, && \text{(C.10)}\\ &= (R^{Gj}_G)^2\,\langle\zeta|\,F^G_{\rho_1}F^j_{\rho_2}A^G(v)F^G_{\rho_2}A^i(v)F^G_{\rho_2}F^G_{\rho_1}|\zeta\rangle\,, && \text{(C.11)} \end{aligned}$$

where we have used the Hermiticity of each of our operators, $A^j(v)(F^G_{\rho_2})^2|\zeta\rangle = A^j(v)(F^A_{\tau_2}+F^B_{\tau_2}+F^G_{\rho_2})|\zeta\rangle = F^j_{\tau/\rho_2}|\zeta\rangle$ and $A^G(v)F^G_{\rho_1}F^j_{\tau/\rho_2}|\zeta\rangle = \overline{(R^{Gj}_G)^2}A^G(v)F^j_{\tau/\rho_2}F^G_{\rho_1}|\zeta\rangle$. The string

operator $F^j_{\tau_2}$ with $j = A$ or B is the direct triangle in the path ρ_2, producing a pair of A or B anyons as in Equations (D.49) and (D.51) respectively.

All these possible inner products can be reduced to phases and inner amplitudes with manipulations of the ribbon operators. We see that if $j = A$ or B and $i = A, B$ or G, we can take

$$\langle\psi_2(j)|\psi_1(i)\rangle = (R^{Gj}_G)^2 \langle\zeta| F^G_{\rho_1} F^j_{\rho_2} A^G(v) F^G_{\rho_2} A^i(v) F^G_{\rho_2} F^G_{\rho_1} |\zeta\rangle , \tag{C.12}$$

$$= (R^{Gj}_G)^2 \langle\zeta| F^G_{\rho_1} F^G_{\rho_2} A^i(v) A^i(v) F^G_{\rho_2} F^G_{\rho_1} |\zeta\rangle , \tag{C.13}$$

$$= (R^{Gj}_G)^2 \frac{1}{N_i^2} \langle\phi_{21}(i)|\phi_{21}(i)\rangle , \tag{C.14}$$

$$= \frac{(R^{Gj}_G)^2}{N_i^2}, \tag{C.15}$$

for the normalised states $|\phi_{21}(i)\rangle$ as defined in (4.35).

When $j = G$ and $i = A$ or B we have

$$\langle\psi_2(G)|\psi_1(i)\rangle = (R^{GG}_G)^2 \langle\zeta| F^G_{\rho_1} F^G_{\rho_2} A^G(v) F^G_{\rho_2} A^i(v) F^G_{\rho_2} F^G_{\rho_1} |\zeta\rangle , \tag{C.16}$$

$$= (R^{GG}_G)^2 \langle\zeta| F^G_{\rho_1} (F^G_{\rho_2})^2 A^i(v) F^G_{\rho_2} F^G_{\rho_1} |\zeta\rangle , \tag{C.17}$$

$$= (R^{GG}_G)^2 \langle\zeta| F^G_{\rho_1} F^G_{\rho_2} A^i(v) A^i(v) F^G_{\rho_2} F^G_{\rho_1} |\zeta\rangle , \tag{C.18}$$

$$= \frac{(R^{GG}_G)^2}{N_i^2}. \tag{C.19}$$

And finally, for the case $i = j = G$

$$\langle\psi_2(G)|\psi_1(G)\rangle = (R^{GG}_G)^2 \langle\zeta| F^G_{\rho_1} F^G_{\rho_2} A^G(v) F^G_{\rho_2} A^G(v) F^G_{\rho_2} F^G_{\rho_1} |\zeta\rangle , \tag{C.20}$$

$$= \frac{(R^{GG}_G)^2}{N_G^2} \langle\phi_{21}(G)| F^G_{\rho_2} |\phi_{21}(G)\rangle . \tag{C.21}$$

The operator $F^G_{\rho_2}$ as defined in Eq. (4.26) is constructed from terms of the form $L^g_+ \otimes T^h_-$. The non-zero matrix elements of the operators T^h_- lie on the main diagonal, whereas L^g_+ act as permutation operators between group elements such that the resultant operator $F^G_{\rho_2}$ is traceless and we obtain the required $\langle\psi_2(G)|\psi_1(G)\rangle = 0$.

These analytical values for each of the overlaps $\langle\psi_2(j)|\psi_1(i)\rangle$ may be substituted into Equation (4.50) in order to determine each of the values of the F matrix squared.

Appendix D

Supplementary material for Chapter 5

D.1 Computation of anyonic fusion and braiding properties using two qutrits

D.1.1 R Matrix from qutrit measurements

In Section 5.3, we have shown that one may obtain the values of all overlaps of the form $\langle\phi_{12}(i)|\phi_{21}(j)\rangle$, $i,j=+,G$, from the computation of expectations values on two qutrits. Here we demonstrate that these values are sufficient to reconstruct the matrix elements $[R_i^{GG}]^2$ in the anyonic basis.

By definition

$$|\phi_{21}(+)\rangle = \frac{1}{\sqrt{2}}\left(|\phi_{21}(A)\rangle + |\phi_{21}(B)\rangle\right), \tag{D.1}$$

$$= \frac{1}{\sqrt{2}}\left([R_A^{GG}]^2\,|\phi_{12}(A)\rangle + [R_B^{GG}]^2\,|\phi_{12}(B)\rangle\right). \tag{D.2}$$

It is also true that

$$|\phi_{21}(+)\rangle = [R_+^{GG}]^2 \, |\phi_{12}(+)\rangle \,, \tag{D.3}$$

$$= \frac{1}{\sqrt{2}} \left([R_+^{GG}]^2 \, |\phi_{12}(A)\rangle + [R_+^{GG}]^2 \, |\phi_{12}(B)\rangle \right). \tag{D.4}$$

Equating these two expressions we therefore have that

$$[R_A^{GG}]^2 = [R_B^{GG}]^2 = [R_+^{GG}]^2, \tag{D.5}$$

where $[R_+^{GG}]^2 \equiv \langle \phi_{12}(+) | \phi_{21}(+) \rangle$ may be calculated from operations on qutrits as

$$[R_+^{GG}]^2 = \langle \xi | \, \mathcal{F}_{\rho_1}^G \mathcal{F}_{\rho_2}^G \mathcal{A}^+(v_3) \mathcal{A}^+(v_3) \mathcal{F}_{\rho_1}^G \mathcal{F}_{\rho_2}^G \, | \xi \rangle \equiv \langle \xi | \, \mathcal{O}_{R_+} \, | \xi \rangle \,. \tag{D.6}$$

Thus, the symmetry of the A and B anyons under braiding enables a straightforward –.

D.1.2 F Matrix from Qutrit Measurements

In this section, we demonstrate how the values obtained for each of these measurable values, alongside the properties of F matrices, allow for the unique determination of the values of the elements $([F_{GGG}^G]_j^i)^2$ in the anyonic basis $\{A, B, G\}$.

We label the elements of the fusion matrix F_{GGG}^G as follows

$$F_{GGG}^G \equiv \begin{pmatrix} f_{AA} & f_{AB} & f_{AG} \\ f_{BA} & f_{BB} & f_{BG} \\ f_{GA} & f_{GB} & f_{GG} \end{pmatrix} = \begin{pmatrix} a & b & c \\ d & e & f \\ g & h & i \end{pmatrix}. \tag{D.7}$$

In Chapter 4, we showed that the overlaps of the states $|\psi_1(i)\rangle$ and $|\psi_2(j)\rangle$ as defined in

Equation (4.46), are related to the elements of the 'squared' matrix

$$F = \begin{pmatrix} f_{AA}^2 & f_{AB}^2 & f_{AG}^2 \\ f_{BA}^2 & f_{BB}^2 & f_{BG}^2 \\ f_{GA}^2 & f_{GB}^2 & f_{GG}^2 \end{pmatrix}, \tag{D.8}$$

by

$$[F]_j^i \equiv (f_{ij})^2 = (R_G^{Gj})^* \frac{\langle \psi_2(j)|\psi_1(i)\rangle}{\langle \psi_2(j)|\psi_2(j)\rangle}, \tag{D.9}$$

where

$$R_G^{Gj} = \begin{cases} 1, & j = A/B, \\ \omega, & j = G. \end{cases} . \tag{D.10}$$

Introducing the notation

$$m_{ji} \equiv \langle \psi_2(j)|\psi_1(i)\rangle, \tag{D.11}$$

$$n_j \equiv \langle \psi_2(j)|\psi_2(j)\rangle, \tag{D.12}$$

allows Equation (D.9) to be written in the condensed form

$$(f_{ij})^2 = (R_G^{Gj})^* \frac{m_{ji}}{n_j}. \tag{D.13}$$

The states $|\psi_1(i)\rangle$ and $|\psi_2(i)\rangle$ for $i = A, B, G$ are composed of operations on the minimal quantum double lattice of four $d = 6$ qudits as in Section 5.2. As shown in Section 5.3, creating the linear superpositions $|\psi_1(\pm)\rangle = \frac{1}{\sqrt{2}}\left(|\psi_1(A)\rangle \pm |\psi_1(B)\rangle\right)$ and $|\psi_2(\pm)\rangle = \frac{1}{\sqrt{2}}\left(|\psi_2(A)\rangle \pm |\psi_2(B)\rangle\right)$ of these states facilitates a dense encoding scheme, allowing certain expectation values to be computed from measurements on just two qutrits. Explicitly, for $i, j = +, G$ we have

$$m_{ji} \equiv \langle \psi_2(j)|\psi_1(i)\rangle = \langle \xi| \mathcal{O}_{m_{ji}} |\xi\rangle , \tag{D.14}$$

$$n_j \equiv \langle \psi_2(j)|\psi_2(j)\rangle = \langle \xi| \mathcal{O}_{n_j} |\xi\rangle , \tag{D.15}$$

such that the six values $m_{++}, m_{+G}, m_{G+}, m_{GG}, n_+$ and n_G are directly measurable on a two-qutrit system. Below we show how the values of such measurements may be related to expressions in terms of the elements of the matrix $([F^G_{GGG}]^i_j)^2$ in the anyonic basis $\{A, B, G\}$, allowing us to re-derive this matrix in terms of these six directly measurable quantities only.

For clarity, the following analysis is broken into distinct subsections. First, we consider the information obtained from the 'G' measurements i.e. those unchanged by the basis transformation $\{A, B, G\} \mapsto \{+, -, G\}$. From these one may immediately derive the value of the element $f^2_{GG} \equiv ([F^G_{GGG}]^G_G)^2$. The unitarity of the matrix F^G_{GGG} in the anyonic basis is then used to set up a series of simultaneous equations for the remaining elements f^2_{ij}. Next, the other directly measurable values $m_{++}, m_{+G}, m_{G+}, n_+$ provide further relationships between the elemnts f^2_{ij}. With an additional analysis of the overlaps of the form $\langle\psi_2(\pm)|\psi_1(\mp)\rangle$ we make a series of 'indirect' measurements. Combining all of this information, we may therefore derive explicit expressions for all elements f^2_{ij} in terms of the six values $m_{++}, m_{+G}, m_{G+}, m_{GG}, n_+$ and n_G directly measurable on a two-qutrit system.

Initial measurements

We start by considering the expectation values of overlaps of 'G' states. These states are unchanged by the basis transformation $\{A, B, G\} \to \{+, -, G\}$ such that the measurements on the qutrit system may be straightforwardly applied to obtain the value of the element f^2_{GG}. Consider first

$$n_G \equiv \langle\psi_2(G)|\psi_2(G)\rangle. \tag{D.16}$$

The value of the normalization factor n_G can be obtained directly from qutrit measurements of this overlap. We expect $n_G \neq 0$. One then has

$$m_{GG} \equiv \langle\psi_2(G)|\psi_1(G)\rangle = \omega n_G f^2_{GG}. \tag{D.17}$$

Measuring this value should yield $m_{GG} = 0$. As ω and n_G are non-zero this will allow us to conclude that $f_{GG}^2 = 0$ which will be substituted into the form of F going forward.

Properties of F^G_{GGG}

We start by considering the information about $\mathcal{F}$ that can be extracted from the general structure of the fusion matrix F^G_{GGG}. We know that F^G_{GGG} is unitary such that $F^G_{GGG}\left[F^G_{GGG}\right]^\dagger = \mathbf{1}$ or

$$\begin{pmatrix} f_{AA} & f_{AB} & f_{AG} \\ f_{BA} & f_{BB} & f_{BG} \\ f_{GA} & f_{GB} & f_{GG} \end{pmatrix} \begin{pmatrix} f^*_{AA} & f^*_{BA} & f^*_{GA} \\ f^*_{AB} & f^*_{BB} & f^*_{GB} \\ f^*_{AG} & f^*_{BG} & f^*_{GG} \end{pmatrix}$$
$$= \begin{pmatrix} |f_{AA}|^2 + |f_{AB}|^2 + |f_{AG}|^2 & f_{AA}f^*_{BA} + f_{AB}f^*_{BB} + f_{AG}f^*_{BG} & f_{AA}f^*_{GA} + f_{AB}f^*_{GB} \\ f^*_{AA}f_{BA} + f^*_{AB}f_{BB} + f^*_{AG}f_{BG} & |f_{AB}|^2 + |f_{BA}|^2 + |f_{BB}|^2 & f_{BA}g^* + f_{BB}f^*_{GB} \\ f^*_{AA}f_{GA} + f^*_{AB}h & f^*_{BA}f_{GA} + f^*_{BB}f_{GB} & |f_{GA}|^2 + |f_{GB}|^2 \end{pmatrix} = \mathbf{1}$$

yielding six simultaneous equations in terms of $f_{AA}, f_{AB}, f_{AG}, f_{BA}, f_{BB}$:

$$\begin{aligned} |f_{AA}|^2 + |f_{AB}|^2 + |f_{AG}|^2 &= 1 \\ |f_{AB}|^2 + |f_{BA}|^2 + |f_{BB}|^2 &= 1 \\ |f_{GA}|^2 + |f_{GB}|^2 &= 1 \\ f_{AA}f^*_{BA} + f_{AB}f^*_{BB} + f_{AG}f^*_{BG} &= 0 \\ f_{AA}f^*_{GA} + f_{AB}f^*_{GB} &= 0 \\ f_{BA}f^*_{GA} + f_{BB}f^*_{GB} &= 0. \end{aligned}$$

By looking at the last two equations we see that $\frac{f_{AA}}{f_{AB}} = \frac{f_{BA}}{f_{BB}} = -\frac{f^*_{GB}}{f^*_{GA}}$ or

$$\frac{f^2_{AA}}{f^2_{AB}} = \frac{f^2_{BA}}{f^2_{BB}} = \left(\frac{f^2_{GB}}{f^2_{GA}}\right)^*. \tag{D.18}$$

Similarly, this unitarity condition may equivalently be given as $\left[F^G_{GGG}\right]^\dagger F^G_{GGG} = \mathbf{1}$ yielding

$$\begin{aligned}
&\begin{pmatrix} f^*_{AA} & f^*_{BA} & f^*_{GA} \\ f^*_{AB} & f^*_{BB} & f^*_{GB} \\ f^*_{AG} & f^*_{BG} & f^*_{GG} \end{pmatrix} \begin{pmatrix} f_{AA} & f_{AB} & f_{AG} \\ f_{BA} & f_{BB} & f_{BG} \\ f_{GA} & f_{GB} & f_{GG} \end{pmatrix} \\
&\qquad = \begin{pmatrix} |f_{AA}|^2 + |f_{BA}|^2 + |f_{GA}|^2 & f^*_{AA}f_{AB} + f^*_{BA}f_{BB} + f^*_{GA}f_{GB} & f^*_{AA}f_{AG} + f^*_{BA}f_{BG} \\ f_{AA}f^*_{AB} + f_{BA}f^*_{BB} + f_{GA}f^*_{GB} & |f_{AB}|^2 + |f_{BB}|^2 + |f_{GB}|^2 & f^*_{AB}f_{AG} + f^*_{BB}f_{BG} \\ f_{AA}f^*_{AG} + f_{BA}f^*_{BG} & f_{AB}f^*_{AG} + f_{BB}f^*_{BG} & |f_{AG}|^2 + |f_{BG}|^2 \end{pmatrix}, \\
&\qquad = \mathbf{1}
\end{aligned}$$

such that

$$\begin{aligned}
|f_{AA}|^2 + |f_{BA}|^2 + |f_{GA}|^2 &= 1 \\
|f_{AB}|^2 + |f_{BB}|^2 + |f_{GB}|^2 &= 1 \\
|f_{AG}|^2 + |f_{BG}|^2 &= 1 \\
f_{AA}f^*_{AB} + f_{BA}f^*_{BB} + f_{GA}f^*_{GB} &= 0 \\
f_{AA}f^*_{AG} + f_{BA}f^*_{BG} &= 0 \\
f_{AB}f^*_{AG} + f_{BB}f^*_{BG} &= 0.
\end{aligned}$$

Like above, the last two equations can be manipulated to gain the following relationship

$$\frac{f^2_{AA}}{f^2_{BA}} = \frac{f^2_{AB}}{f^2_{BB}} = \left(\frac{f^2_{BG}}{f^2_{AG}}\right)^*. \tag{D.19}$$

Direct measurements

In addition to n_G and m_{GG} there are four additional expectation values that may be directly obtained from measurements of the qutrit system: m_{+G}, m_{G+}, m_{++} and n_+. Here we establish four independent simultaneous equations, linking the co-efficients f_{ij}

to these directly measurable quantities.

$$\begin{aligned}
m_{++} &\equiv \langle\psi_2(+)|\psi_1(+)\rangle, \\
&= \frac{1}{2}(\langle\psi_2(A)| + \langle\psi_2(B)|)(|\psi_1(A)\rangle + |\psi_1(B)\rangle), \\
&= \frac{1}{2}(m_{AA} + m_{BA} + m_{AB} + m_{BB}) \\
&= \frac{1}{2}(R_G^{GA} n_A f_{AA}^2 + R_G^{GB} n_B f_{BA}^2 + R_G^{GA} n_A f_{AB}^2 + R_G^{GB} n_B f_{BB}^2), \\
&= \frac{1}{2}(R_G^{GA} n_A f_{AA}^2 + R_G^{GB} n_B f_{AB}^2 + R_G^{GA} n_A f_{BA}^2 + R_G^{GB} n_B f_{BB}^2), \\
&= \frac{1}{2}\left(n_A(f_{AA}^2 + f_{BA}^2) + n_B(f_{AB}^2 + f_{BB}^2)\right). \qquad \text{(D.20)}
\end{aligned}$$

$$\begin{aligned}
n_+ &\equiv \langle\psi_2(+)|\psi_2(+)\rangle, \\
&= \frac{1}{2}(\langle\psi_2(A)| + \langle\psi_2(B)|)(|\psi_2(A)\rangle + |\psi_2(B)\rangle), \\
&= \frac{1}{2}(n_A + n_B). \qquad \text{(D.21)}
\end{aligned}$$

$$\begin{aligned}
m_{+G} &\equiv \langle\psi_2(+)|\psi_1(G)\rangle, \\
&= \frac{1}{\sqrt{2}}(\langle\psi_2(A)| + \langle\psi_2(B)|)\,|\psi_1(G)\rangle\,, \\
&= \frac{1}{\sqrt{2}}(m_{AG} + m_{BG}), \\
&= \frac{1}{\sqrt{2}}(n_A f_{GA}^2 + n_B f_{GB}^2). \qquad \text{(D.22)}
\end{aligned}$$

$$\begin{aligned}
m_{G+} &\equiv \langle\psi_2(G)|\psi_1(+)\rangle, \\
&= \frac{1}{\sqrt{2}}\,\langle\psi_2(G)|\,(|\psi_1(A)\rangle + |\psi_1(B)\rangle), \\
&= \frac{1}{\sqrt{2}}(m_{GA} + m_{GB}), \\
&= \frac{1}{\sqrt{2}}\left(R_G^{GG} n_G(f_{AG}^2 + f_{BG}^2)\right). \qquad \text{(D.23)}
\end{aligned}$$

Indirect Measurements

Although the overlaps with the states $|\psi_{1,2}(-)\rangle$ cannot be obtained from measurements on the two-qutrit basis, the action of the associated operators on different sectors of the Hilbert space, allows us to conclude that the '+' states are orthogonal to the '−' states.

Consider the non-trivial two-qudit components of the operators $F^G_{\rho_1}, F^G_{\rho_2}, A^G(v_3), A^+(v_3)$ and $A^-(v_3)$,

$$
\begin{aligned}
f^G_{\rho_1} &= (Z \oplus \mathbf{0}_3) \otimes (X \oplus X) + (Z^2 \oplus \mathbf{0}_3) \otimes (X^2 \oplus X^2),\\
f^G_{\rho_2} &= (X \oplus X^2) \otimes (Z^2 \oplus \mathbf{0}_3) + (X^2 \oplus X) \otimes (Z \oplus \mathbf{0}_3),\\
a^G(v_3) &= \frac{1}{3}[2(\mathbf{1}_3 \oplus \mathbf{1}_3) \otimes (\mathbf{1}_3 \oplus \mathbf{1}_3) - (X \oplus X^2) \otimes (X^2 \oplus X^2) - (X^2 \oplus X) \otimes (X \oplus X)],\\
a^+(v_3) &= \frac{1}{3\sqrt{2}}[(\mathbf{1}_3 \oplus \mathbf{1}_3) \otimes (\mathbf{1}_3 \oplus \mathbf{1}_3) + (X \oplus X^2) \otimes (X^2 \oplus X^2) + (X^2 \oplus X) \otimes (X \oplus X)],\\
a^-(v_3) &= \frac{1}{3\sqrt{2}}[(\mathbf{1}_3 \overline{\oplus} \mathbf{1}_3) \otimes (\alpha \overline{\oplus} \alpha) + (X^2 \overline{\oplus} X) \otimes (\beta \overline{\oplus} \beta) + (X \overline{\oplus} X^2) \otimes (\gamma \overline{\oplus} \gamma)].
\end{aligned}
$$

where

$$
\begin{aligned}
\alpha &= \mathbf{1}_3 + Z + Z^2 + X(\mathbf{1}_3 + \bar{\omega}Z + \omega Z^2) + X^2(\mathbf{1}_3 + \omega Z + \bar{\omega} Z^2),\\
\beta &= \mathbf{1}_3 + \omega Z + \bar{\omega} Z^2 + X(\mathbf{1}_3 + Z + Z^2) + X^2(\mathbf{1}_3 + \bar{\omega}Z + \omega Z^2),\\
\gamma &= \mathbf{1}_3 + \bar{\omega} Z + \omega Z^2 + X(\mathbf{1}_3 + \omega Z + \bar{\omega} Z^2) + X^2(\mathbf{1}_3 + Z + Z^2),
\end{aligned}
$$

and '$\oplus$' and '$\overline{\oplus}$' denote the matrix direct sums along the main and secondary diagonals respectively, such that for matrices A and B,

$$
A \oplus B = \begin{pmatrix} A & 0 \\ 0 & B \end{pmatrix}, \qquad A \overline{\oplus} B = \begin{pmatrix} 0 & A \\ B & 0 \end{pmatrix}. \tag{D.24}
$$

Referring to Equation (5.20), we may write

$$
m_{ji} = 6 \sum_{g \in \mathbf{S}_3} \langle \psi_g | \, o_2(j)^\dagger o_1(i) \, | \psi_g \rangle \tag{D.25}
$$

where

$$o_1(i) = a^G(v_3) f^G_{\rho_2} a^i(v_3) f^G_{\rho_2} f^G_{\rho_1}, \tag{D.26}$$

$$o_2(j) = a^G(v_3) f^G_{\rho_1} a^j(v_3) f^G_{\rho_2} f^G_{\rho_2}. \tag{D.27}$$

By expanding out each product of terms we find that depending on the choice of $i = +, -, G$, the product $o_1(i)$ is a summation of terms of the form

$$o_1(i) = \begin{cases} \begin{pmatrix} A & \mathbf{0}_3 \\ \mathbf{0}_3 & \mathbf{0}_3 \end{pmatrix} \otimes \begin{pmatrix} B & \mathbf{0}_3 \\ \mathbf{0}_3 & C \end{pmatrix} + \ldots, & i = +, G, \\ \begin{pmatrix} \mathbf{0}_3 & \mathbf{0}_3 \\ D & \mathbf{0}_3 \end{pmatrix} \otimes \begin{pmatrix} \mathbf{0}_3 & \mathbf{0}_3 \\ \mathbf{0}_3 & \mathbf{0}_3 \end{pmatrix} + \ldots, & i = -, \end{cases}$$

where A, B, C, D are single-qutrit operators. Similarly,

$$o_2(j) = \begin{cases} \begin{pmatrix} E & \mathbf{0}_3 \\ \mathbf{0}_3 & \mathbf{0}_3 \end{pmatrix} \otimes \begin{pmatrix} F & \mathbf{0}_3 \\ \mathbf{0}_3 & \mathbf{0}_3 \end{pmatrix} + \ldots, & i = +, G, \\ \begin{pmatrix} \mathbf{0}_3 & G \\ \mathbf{0}_3 & \mathbf{0}_3 \end{pmatrix} \otimes \begin{pmatrix} \mathbf{0}_3 & \mathbf{0}_3 \\ H & \mathbf{0}_3 \end{pmatrix} + \ldots, & i = -. \end{cases}$$

Consider the term m_{+-}. For some general two-qudit state $|\psi\rangle = \begin{pmatrix} J \\ K \end{pmatrix} \otimes \begin{pmatrix} L \\ M \end{pmatrix}$, $o_1(-)|\psi\rangle = \begin{pmatrix} 0 \\ AJ \end{pmatrix} \otimes \begin{pmatrix} 0 \\ 0 \end{pmatrix} + \ldots$ while $o_2(+)|\psi\rangle = \begin{pmatrix} EJ \\ 0 \end{pmatrix} \otimes \begin{pmatrix} FL \\ 0 \end{pmatrix} + \ldots$, where we have differentiated between the co-efficients of group elements $\{e, c, c^2\}$ and $\{t, tc, tc^2\}$ in each state. It should be clear that as $o_1(-)$ and $o_2(+)$ only have non-trivial action of different sectors of the Hilbert space, their overlap as in Eq. (D.25) necessarily results in $m_{+-} = 0$. One can show that $m_{-+} = 0$ in the same way. The only truly inaccessible

state we consider is the overlap of two '−' states given by

$$\begin{aligned} m_{--} &\equiv \langle\psi_2(-)|\psi_1(-)\rangle, \\ &= \frac{1}{2}(\langle\psi_2(A)| - \langle\psi_2(B)|)(|\psi_1(A)\rangle - |\psi_1(B)\rangle), \\ &= \frac{1}{2}(m_{AA} - m_{BA} - m_{AB} + m_{BB}), \\ &= \frac{1}{2}\left(n_A(f_{AA}^2 - f_{BA}^2) - n_B(f_{AB}^2 - f_{BB}^2)\right). \end{aligned} \tag{D.28}$$

Returning to m_{+-}, we have

$$\begin{aligned} m_{+-} &\equiv \langle\psi_2(+)|\psi_1(-)\rangle, \\ &= \frac{1}{2}(\langle\psi_2(A)| + \langle\psi_2(B)|)(|\psi_1(A)\rangle - |\psi_1(B)\rangle), \\ &= \frac{1}{2}(m_{AA} + m_{BA} - m_{AB} - m_{BB}), \\ &= \frac{1}{2}\left(n_A(f_{AA}^2 - f_{BA}^2) + n_B(f_{AB}^2 - f_{BB}^2)\right) = 0. \end{aligned} \tag{D.29}$$

Taking (D.28) + (D.29)

$$f_{AA}^2 - f_{BA}^2 = \frac{m_{--}}{n_A} \tag{D.30}$$

and (D.29) - (D.28)

$$f_{AB}^2 - f_{BB}^2 = -\frac{m_{--}}{n_B}. \tag{D.31}$$

The normalization term

$$n_{+-} = \frac{1}{2}(n_A - n_B) = 0 \tag{D.32}$$

combined with (D.21) yields

$$n_A = n_B = n_+. \tag{D.33}$$

Substitution back into (D.30) and (D.31) gives

$$f_{AA}^2 - f_{BA}^2 = \frac{m_{--}}{n_+} = -(f_{AB}^2 - f_{BB}^2). \tag{D.34}$$

Finally,

$$\begin{aligned} m_{-+} &\equiv \langle\psi_2(-)|\psi_1(+)\rangle \\ &= \frac{1}{2}(\langle\psi_2(A)| - \langle\psi_2(B)|)(|\psi_1(A)\rangle + |\psi_1(B)\rangle) \\ &= \frac{1}{2}(m_{AA} - m_{BA} + m_{AB} - m_{BB}) \\ &= \frac{1}{2}\left(n_A(f_{AA}^2 + f_{BA}^2) - n_B(f_{AB}^2 + f_{BB}^2)\right) = 0 \end{aligned} \tag{D.35}$$

(D.20) + (D.35) and (D.20) - (D.35) yield

$$f_{AA}^2 + f_{BA}^2 = \frac{m_{++}}{n_+} = f_{AB}^2 + f_{BB}^2 \tag{D.36}$$

then (D.34) + (D.36) gives

$$f_{AA}^2 = f_{BB}^2 \tag{D.37}$$

while (D.36) − (D.34) gives

$$f_{AB}^2 = f_{BA}^2. \tag{D.38}$$

From (D.20)

$$\begin{aligned} m_{++} &= n_+(f_{AA}^2 + f_{AB}^2) \\ \rightarrow f_{AA}^2 + f_{AB}^2 &= \frac{m_{++}}{n_+} \end{aligned} \tag{D.39}$$

and from (D.34)

$$f_{AA}^2 - f_{AB}^2 = \frac{m_{--}}{n_+} \tag{D.40}$$

such that

$$f_{AA}^2 = f_{BB}^2 = \frac{m_{++} + m_{--}}{2n_+}, \qquad f_{AB}^2 = f_{BA}^2 = \frac{m_{++} - m_{--}}{2n_+}. \tag{D.41}$$

From the matrix unitarity property (D.18) $\frac{f_{AA}^2}{f_{AB}^2} = \frac{f_{BA}^2}{f_{BB}^2} \Rightarrow \frac{f_{AA}^2}{f_{AB}^2} = \frac{f_{AB}^2}{f_{AA}^2}$

$$(f_{AA}^2)^2 = (f_{AB}^2)^2 \tag{D.42}$$

$$\left(\frac{m_{++} + m_{--}}{2n_+}\right)^2 = \left(\frac{m_{++} - m_{--}}{2n_+}\right)^2 \tag{D.43}$$

$$(m_{++} + m_{--})^2 = (m_{++} - m_{--})^2 \tag{D.44}$$

$$\Rightarrow m_{++}m_{--} = 0 \tag{D.45}$$

meaning that m_{++} and/or m_{--} must be equal to zero. m_{++} is one of our directly measurable qutrit quantities, we expect $m_{++} \neq 0$, taking the measurement to verify this will allow us to conclude that $m_{--} = 0$. Assuming this to be true,

$$f_{AA}^2 = f_{AB}^2 = f_{BA}^2 = f_{BB}^2 = \frac{m_{++}}{2n_+}. \tag{D.46}$$

From (D.22)

$$f_{GA}^2 + f_{GB}^2 = \frac{2m_{+G}}{n_+}$$

and our second unitarity identity (D.18), $(\frac{f_{GB}^2}{f_{GA}^2})^* = \frac{f_{AA}^2}{f_{AB}^2} = 1 \Rightarrow f_{GB}^2 = f_{GA}^2$ and

$$f_{GA}^2 = f_{GB}^2 = \frac{m_{+G}}{n_+}. \tag{D.47}$$

Finally, from (D.23)

$$f_{AG}^2 + f_{BG}^2 = \frac{m_{G+}}{\omega n_G}$$

and (D.19), $f_{AG}^2 = f_{BG}^2$, giving the final matrix elements

$$f_{AG}^2 = f_{BG}^2 = \frac{m_{G+}}{2\omega n_G}. \tag{D.48}$$

D.2 Properties of two-qutrit encoding

In Section 5.3 we have demonstrated that the elements of the squared R and F matrices may be computed from overlaps of operations of two qutrits. However, one might ask, to what extent these two-qutrit operators themselves still encode the properties of the full non-Abelian sub-model $\{A, B, G\}$. Here we start by providing a brief examination of the fusion properties associated with the action of these states, before using an approach analogous to that in Appendix C.2 to demonstrate that the ribbon $\mathcal{F}^G_{\rho_1}$ and $\mathcal{F}^G_{\rho_2}$ still directly encode the braiding properties of the G anyons of this model.

In Appendix C.1, we found that the single-qudit operators creating pairs of the Abelian A and B anyons take the forms

$$F^A = T^e_+ + T^c_+ + T^{c^2}_+ + T^t_+ + T^{tc}_+ + T^{tc^2}_+, \tag{D.49}$$

$$= |e\rangle\langle e| + |c\rangle\langle c| + |c^2\rangle\langle c^2| + |t\rangle\langle t| + |tc\rangle\langle tc| + |tc^2\rangle\langle tc^2|, \tag{D.50}$$

$$F^B = |e\rangle\langle e| + |c\rangle\langle c| + |c^2\rangle\langle c^2| - |t\rangle\langle t| - |tc\rangle\langle tc| - |tc^2\rangle\langle tc^2|, \tag{D.51}$$

such that the linear combination

$$F^+ = 2(|e\rangle\langle e| + |c\rangle\langle c| + |c^2\rangle\langle c^2|). \tag{D.52}$$

This may be straightforwardly identified with the action $\mathbf{21}_3$ on the single-qutrit subspace $\{e, c, c^2\}$. Applying this operator to one qutrit out of the pair, one therefore obtains the following two-qutrit representation of the creation operator for the combination of A and B anyons

$$\mathcal{F}^+ = \mathbf{21}_3 \otimes \mathbf{1}_3. \tag{D.53}$$

With this set of simple two-qutrit operators $\mathcal{F}^+, \mathcal{F}^G_{\rho_1}, \mathcal{F}^G_{\rho_2}$ we can explicitly verify the fusion properties of the $\{A, B, G\}$ subgroup of $\mathbf{D}(\mathbf{S}_3)$. As discussed in Section 4.3.2, the fusion of two anyons may be simulated by the overlapping the ribbons that create them.

For example, in the simplest case

$$(\mathcal{F}^{+})^{2} = 2\mathcal{F}^{+}, \tag{D.54}$$

reproduces the expected fusion process

$$+ \times + = (A + B) \times (A + B) \tag{D.55}$$

$$= 2(A + B) \tag{D.56}$$

$$= 2+ \tag{D.57}$$

where $+ \equiv A + B$ is an effective composite of the Abelian A and B anyons. Similarly,

$$\mathcal{F}^{+}\mathcal{F}^{G}_{\rho_{1/2}} = 2\mathcal{F}^{G}_{\rho_{1/2}}, \tag{D.58}$$

corresponds to

$$+ \times G = 2G, \tag{D.59}$$

and finally, the non-Abelian fusion space of two G anyons $G \times G = A + B + G$ is derived by repeated application of the same ribbon as

$$(\mathcal{F}^{G}_{\rho_{1/2}})^{2} = 2\mathbf{1}_{3} + \mathcal{F}^{G}_{\rho_{1/2}} \tag{D.60}$$

$$= \mathcal{F}^{+} + \mathcal{F}^{G}_{\rho_{1/2}}. \tag{D.61}$$

Two-Qutrit operator tomography for the R matrix

In analogy with the approach presented in Appendix C.2, we provide a brief demonstration that the braiding information for the G anyons of the $D(S_3)$ quantum double is still encoded in the reduced qutrit operations $\mathcal{F}^{G}_{\rho_1}$ and $\mathcal{F}^{G}_{\rho_2}$. For the products of these qutrit operators acting on the reduced Hilbert space $\{e, c, c^2\}$, we obtain the following explicit

matrix representations

$$\mathcal{F}^G_{\rho_1}\mathcal{F}^G_{\rho_2} = \begin{pmatrix} 0 & 0 & 0 & 0 & \omega & \bar{\omega} & 0 & \bar{\omega} & \omega \\ 0 & 0 & 0 & 1 & 0 & \bar{\omega} & 1 & 0 & \omega \\ 0 & 0 & 0 & 1 & \omega & 0 & 1 & \bar{\omega} & 0 \\ 0 & \omega & \bar{\omega} & 0 & 0 & 0 & 0 & 1 & 1 \\ \omega & 0 & 1 & 0 & 0 & 0 & \omega & 0 & \omega \\ \bar{\omega} & 1 & 0 & 0 & 0 & 0 & \bar{\omega} & \bar{\omega} & 0 \\ 0 & \bar{\omega} & \omega & 0 & 1 & 1 & 0 & 0 & 0 \\ \bar{\omega} & 0 & 1 & \bar{\omega} & 0 & \bar{\omega} & 0 & 0 & 0 \\ \omega & 1 & 0 & \omega & \omega & 0 & 0 & 0 & 0 \end{pmatrix} \tag{D.62}$$

$$\mathcal{F}^G_{\rho_2}\mathcal{F}^G_{\rho_1} = \begin{pmatrix} 0 & 0 & 0 & 0 & \bar{\omega} & \omega & 0 & \omega & \bar{\omega} \\ 0 & 0 & 0 & \bar{\omega} & 0 & 1 & \omega & 0 & 1 \\ 0 & 0 & 0 & \omega & 1 & 0 & \bar{\omega} & 1 & 0 \\ 0 & 1 & 1 & 0 & 0 & 0 & 0 & \omega & \bar{\omega} \\ \bar{\omega} & 0 & \bar{\omega} & 0 & 0 & 0 & 1 & 0 & \bar{\omega} \\ \omega & \omega & 0 & 0 & 0 & 0 & 1 & \omega & 0 \\ 0 & 1 & 1 & 0 & \bar{\omega} & \omega & 0 & 0 & 0 \\ \omega & 0 & \omega & 1 & 0 & \omega & 0 & 0 & 0 \\ \bar{\omega} & \bar{\omega} & 0 & 1 & \bar{\omega} & 0 & 0 & 0 & 0 \end{pmatrix} \tag{D.63}$$

such that each element of $\mathcal{F}^G_{\rho_1}\mathcal{F}^G_{\rho_2}$ gains an additional phase relative to $\mathcal{F}^G_{\rho_2}\mathcal{F}^G_{\rho_1}$ according to the following prescription

$$|g_1, g_2\rangle\langle h_1, h_2| \to \begin{cases} \bar{\omega}\,|g_1, g_2\rangle\langle h_1, h_2| & \text{if } g_1 g_2 = h_1 h_2 \\ \omega\,|g_1, g_2\rangle\langle h_1, h_2| & \text{otherwise} \end{cases} \tag{D.64}$$

This result is identical to that derived for the full ribbon operators in Section 4.4. The terms corresponding to $|g_1, g_2\rangle\langle h_1, h_2|$ for $g_1 g_2 = h_1 h_2$ are once again interpreted

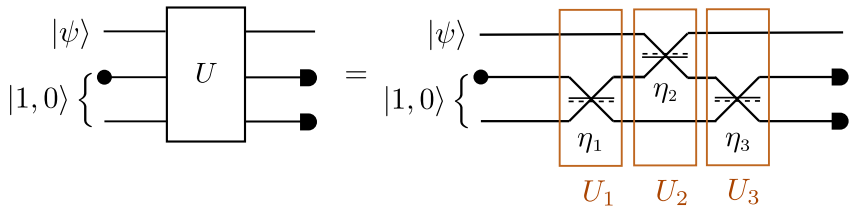

Figure D.1: The unitary U implementing the NS gate on the input state $|\psi\rangle$ may be decomposed as three asymmetric beamsplitters.

as 'flux-conserving' and thus correspond to the braiding of A or B anyons inducing a relative factor of $\bar{\omega}$. The terms for which $g_1 g_2 \neq h_1 h_2$ signal the G anyonic components with non-trivial flux, for which braiding gains a factor of ω. Thus re-deriving the matrix $(R^{GG})^2$ as in Equation (4.14).

D.3 The NS gate

For an arbitrary input state, the non-linear sign gate implements the transformation

$$\alpha\,|0\rangle + \beta\,|1\rangle + \gamma\,|2\rangle \mapsto \alpha\,|0\rangle + \beta\,|1\rangle - \gamma\,|2\rangle\,. \tag{D.65}$$

To enact this gate we require just two ancillary modes and three asymmetric beamsplitters as shown in Figure D.1. In keeping with the convention defined in Section 5.4.1, transmission through either side of the beamsplitter yields a phase $\sqrt{1-\eta}$ while reflection off the solid (dotted) side induces a phase $\sqrt{\eta}$ ($-\sqrt{\eta}$). In this way, the unitaries in Fig. D.1 have explicit forms

$$U_1 = \begin{pmatrix} 1 & 0 & 0 \\ 0 & \sqrt{\eta_1} & \sqrt{1-\eta_1} \\ 0 & \sqrt{1-\eta_1} & -\sqrt{\eta_1} \end{pmatrix}, \qquad U_2 = \begin{pmatrix} -\sqrt{\eta_2} & \sqrt{1-\eta_2} & 0 \\ \sqrt{1-\eta_2} & \sqrt{\eta_2} & 0 \\ 0 & 0 & 1 \end{pmatrix}, \tag{D.66}$$

with U_3 identical to U_1 under the exchanging of labels $1 \leftrightarrow 3$. Taking $\eta_1 = \eta_3 = \frac{1}{4-2\sqrt{2}}$ and $\eta_2 = 3 - 2\sqrt{2}$, the total circuit implements the unitary transformation

$$U = U_3 U_2 U_1 = \begin{pmatrix} 1-\sqrt{2} & \frac{1}{\sqrt{\sqrt{2}}} & \sqrt{\frac{3}{\sqrt{2}}-2} \\ \frac{1}{\sqrt{\sqrt{2}}} & \frac{1}{2} & \frac{1}{2}-\frac{1}{\sqrt{2}} \\ \sqrt{\frac{3}{\sqrt{2}}-2} & \frac{1}{2}-\frac{1}{\sqrt{2}} & \sqrt{2}-\frac{1}{2} \end{pmatrix}, \tag{D.67}$$

or equivalently

$$\begin{aligned} a_1^\dagger &\mapsto \left(1-\sqrt{2}\right) a_1^\dagger + \frac{1}{\sqrt{\sqrt{2}}} a_2^\dagger + \left(\sqrt{\frac{3}{\sqrt{2}}-2}\right) a_3^\dagger, \\ a_2^\dagger &\mapsto \frac{1}{\sqrt{\sqrt{2}}} a_1^\dagger + \frac{1}{2} a_2^\dagger + \left(\frac{1}{2}-\frac{1}{\sqrt{2}}\right) a_3^\dagger, \\ a_3^\dagger &\mapsto \left(\sqrt{\frac{3}{\sqrt{2}}-2}\right) a_1^\dagger + \left(\frac{1}{2}-\frac{1}{\sqrt{2}}\right) a_2^\dagger + \left(\sqrt{2}-\frac{1}{2}\right) a_3^\dagger. \end{aligned} \tag{D.68}$$

For the input state $|\psi\rangle = \alpha|0\rangle + \beta|1\rangle + \gamma|2\rangle$ on the top mode, the total input state including the ancillae is

$$|\Psi\rangle = |\psi\rangle \otimes |1,0\rangle \tag{D.69}$$

$$= \left(\alpha + \beta a_1^\dagger + \frac{\gamma}{\sqrt{2}}(a_1^\dagger)^2\right) a_2^\dagger |0,0,0\rangle . \tag{D.70}$$

Under the mode transformation of (D.68), the circuit in Figure D.1 thus maps $|\Psi\rangle$ to

$$|\Psi\rangle \mapsto \frac{1}{2}\left(\alpha|0\rangle + \beta|1\rangle - \gamma|2\rangle\right) \otimes |1,0\rangle + \ldots, \tag{D.71}$$

where terms for which the ancillae are not in the state $|1,0\rangle$ have not been explicitly included. Measuring $|1,0\rangle$ in modes 2 and 3 thus yields the desired transformation

$$\alpha|0\rangle + \beta|1\rangle + \gamma|2\rangle \mapsto \alpha|0\rangle + \beta|1\rangle - \gamma|2\rangle ,$$

with a probability of success $p_{\mathrm{NS}} = \left|\frac{1}{2}\right|^2 = \frac{1}{4}$.

Bibliography

[1] P. W. Anderson, "More is different: broken symmetry and the nature of the hierarchical structure of science.," *Science*, vol. 177, no. 4047, pp. 393–396, 1972.

[2] J. Bardeen, L. N. Cooper, and J. R. Schrieffer, "Theory of superconductivity," *Physical Review*, vol. 108, no. 5, p. 1175, 1957.

[3] M. Tinkham, *Introduction to superconductivity*. Courier Corporation, 2004.

[4] X.-G. Wen, "Topological orders in rigid states," *International Journal of Modern Physics B*, vol. 4, no. 02, pp. 239–271, 1990.

[5] M. Z. Hasan and C. L. Kane, "Colloquium: topological insulators," *Reviews of modern physics*, vol. 82, no. 4, pp. 3045–3067, 2010.

[6] X.-G. Wen, *Quantum field theory of many-body systems: From the origin of sound to an origin of light and electrons*. Oxford university press, 2004.

[7] P. W. Anderson, "Antiferromagnetism. theory of superexchange interaction," *Physical Review*, vol. 79, no. 2, p. 350, 1950.

[8] P. A. Lee, N. Nagaosa, and X.-G. Wen, "Doping a mott insulator: Physics of high-temperature superconductivity," *Reviews of modern physics*, vol. 78, no. 1, pp. 17–85, 2006.

[9] A. Auerbach, *Interacting electrons and quantum magnetism*. Springer Science & Business Media, 2012.

[10] A. Einstein, B. Podolsky, and N. Rosen, "Can quantum-mechanical description of physical reality be considered complete?," *Physical Review*, vol. 47, no. 10, p. 777, 1935.

[11] E. Schrödinger, "Die gegenwärtige situation in der quantenmechanik," *Naturwissenschaften*, vol. 23, no. 50, pp. 844–849, 1935.

[12] J. S. Bell, "On the Einstein Podolsky Rosen paradox," *Physics Physique Fizika*, vol. 1, no. 3, p. 195, 1964.

[13] A. Aspect, J. Dalibard, and G. Roger, "Experimental test of Bell's inequalities using time-varying analyzers," *Physical Review Letters*, vol. 49, no. 25, p. 1804, 1982.

[14] G. Weihs, T. Jennewein, C. Simon, H. Weinfurter, and A. Zeilinger, "Violation of Bell's inequality under strict Einstein locality conditions," *Physical Review Letters*, vol. 81, no. 23, p. 5039, 1998.

[15] M. A. Rowe, D. Kielpinski, V. Meyer, C. A. Sackett, W. M. Itano, C. Monroe, and D. J. Wineland, "Experimental violation of a Bell's inequality with efficient detection," *Nature*, vol. 409, no. 6822, pp. 791–794, 2001.

[16] B. Hensen, H. Bernien, A. E. Dréau, A. Reiserer, N. Kalb, M. S. Blok, J. Ruitenberg, R. F. Vermeulen, R. N. Schouten, C. Abellán, *et al.*, "Loophole-free Bell inequality violation using electron spins separated by 1.3 kilometres," *Nature*, vol. 526, no. 7575, pp. 682–686, 2015.

[17] A. K. Ekert, "Quantum cryptography based on Bell's theorem," *Physical Review Letters*, vol. 67, no. 6, p. 661, 1991.

[18] R. Horodecki, P. Horodecki, M. Horodecki, and K. Horodecki, "Quantum entanglement," *Reviews of modern physics*, vol. 81, no. 2, pp. 865–942, 2009.

[19] C. H. Bennett, G. Brassard, C. Crépeau, R. Jozsa, A. Peres, and W. K. Wootters, "Teleporting an unknown quantum state via dual classical and [e]instein-Podolsky-Rosen channels," *Physical Review Letters*, vol. 70, no. 13, p. 1895, 1993.

[20] D. Bouwmeester, J.-W. Pan, K. Mattle, M. Eibl, H. Weinfurter, and A. Zeilinger, "Experimental quantum teleportation," *Nature*, vol. 390, no. 6660, pp. 575–579, 1997.

[21] M. A. Nielsen and I. L. Chuang, *Quantum computation and quantum information*, vol. 2. Cambridge university press Cambridge, 2001.

[22] A. Y. Kitaev, "Fault-tolerant quantum computation by anyons," *Annals of physics*, vol. 303, no. 1, pp. 2–30, 2003.

[23] F. Wilczek, "Quantum mechanics of fractional-spin particles," *Physical Review Letters*, vol. 49, no. 14, p. 957, 1982.

[24] A. Kitaev, "Anyons in an exactly solved model and beyond," *Annals of Physics*, vol. 321, no. 1, pp. 2–111, 2006.

[25] J. K. Pachos, *Introduction to topological quantum computation*. Cambridge University Press, 2012.

[26] P. Yu, J. Chen, M. Gomanko, G. Badawy, E. Bakkers, K. Zuo, V. Mourik, and S. Frolov, "Non-Majorana states yield nearly quantized conductance in superconductor-semiconductor nanowire devices," *arXiv preprint arXiv:2004.08583*, 2020.

[27] M. Banerjee, M. Heiblum, V. Umansky, D. E. Feldman, Y. Oreg, and A. Stern, "Observation of half-integer thermal hall conductance," *Nature*, vol. 559, no. 7713, pp. 205–210, 2018.

[28] Y. Kasahara, T. Ohnishi, Y. Mizukami, O. Tanaka, S. Ma, K. Sugii, N. Kurita, H. Tanaka, J. Nasu, Y. Motome, *et al.*, "Majorana quantization and half-integer

thermal quantum Hall effect in a Kitaev spin liquid," *Nature*, vol. 559, no. 7713, pp. 227–231, 2018.

[29] P. Bonderson, A. Kitaev, and K. Shtengel, "Detecting non-abelian statistics in the ν= 5/2 fractional quantum hall state," *Physical Review Letters*, vol. 96, no. 1, p. 016803, 2006.

[30] N. Bohr, "Can quantum-mechanical description of physical reality be considered complete?," *Physical review*, vol. 48, no. 8, p. 696, 1935.

[31] E. Schrödinger, "Discussion of probability relations between separated systems," in *Mathematical Proceedings of the Cambridge Philosophical Society*, vol. 31, pp. 555–563, Cambridge University Press, 1935.

[32] S. J. Freedman and J. F. Clauser, "Experimental test of local hidden-variable theories," *Physical review letters*, vol. 28, no. 14, p. 938, 1972.

[33] A. Aspect, P. Grangier, and G. Roger, "Experimental tests of realistic local theories via bell's theorem," *Physical review letters*, vol. 47, no. 7, p. 460, 1981.

[34] M. A. Nielsen, "Quantum information theory," *arXiv preprint quant-ph/0011036*, pp. 165–171, 2000.

[35] R. Jozsa, "Illustrating the concept of quantum information," *IBM Journal of Research and Development*, vol. 48, no. 1, pp. 79–85, 2004.

[36] R. Jozsa, "Entanglement and quantum computation," *arXiv preprint quant-ph/9707034*, 1997.

[37] C. H. Bennett and S. J. Wiesner, "Communication via one-and two-particle operators on einstein-podolsky-rosen states," *Physical review letters*, vol. 69, no. 20, p. 2881, 1992.

[38] L. Amico, R. Fazio, A. Osterloh, and V. Vedral, "Entanglement in many-body systems," *Reviews of modern physics*, vol. 80, no. 2, pp. 517–576, 2008.

[39] J. Eisert, M. Cramer, and M. B. Plenio, "Colloquium: Area laws for the entanglement entropy," *Reviews of modern physics*, vol. 82, no. 1, pp. 277–306, 2010.

[40] M. B. Hastings, "An area law for one-dimensional quantum systems," *Journal of statistical mechanics: theory and experiment*, vol. 2007, no. 08, p. P08024, 2007.

[41] G. Vitagliano, A. Riera, and J. I. Latorre, "Volume-law scaling for the entanglement entropy in spin-1/2 chains," *New Journal of Physics*, vol. 12, no. 11, p. 113049, 2010.

[42] G. Ramírez, J. Rodríguez-Laguna, and G. Sierra, "From conformal to volume law for the entanglement entropy in exponentially deformed critical spin 1/2 chains," *Journal of Statistical Mechanics: Theory and Experiment*, vol. 2014, no. 10, p. P10004, 2014.

[43] G. Ramírez, J. Rodríguez-Laguna, and G. Sierra, "Breaking the area law: The rainbow state," in *Strongly Coupled Field Theories for Condensed Matter and Quantum Information Theory: Proceedings, International Institute of Physics, Natal, Rn, Brazil, 2–21 August 2015*, pp. 395–405, Springer, 2020.

[44] J. Rodríguez-Laguna, J. Dubail, G. Ramírez, P. Calabrese, and G. Sierra, "More on the rainbow chain: entanglement, space-time geometry and thermal states," *Journal of Physics A: Mathematical and Theoretical*, vol. 50, no. 16, p. 164001, 2017.

[45] N. Samos Sáenz de Buruaga, S. N. Santalla, J. Rodríguez-Laguna, and G. Sierra, "Piercing the rainbow state: Entanglement on an inhomogeneous spin chain with a defect," *Physical Review B*, vol. 101, no. 20, p. 205121, 2020.

[46] C. M. Langlett, Z.-C. Yang, J. Wildeboer, A. V. Gorshkov, T. Iadecola, and S. Xu, "Rainbow scars: From area to volume law," *Physical Review B*, vol. 105, no. 6, p. L060301, 2022.

[47] G. Ramírez, J. Rodríguez-Laguna, and G. Sierra, "Entanglement over the rainbow," *Journal of Statistical Mechanics: Theory and Experiment*, vol. 2015, no. 6, p. P06002, 2015.

[48] A. Pocklington, Y.-X. Wang, Y. Yanay, and A. A. Clerk, "Stabilizing volume-law entangled states of fermions and qubits using local dissipation," *Physical Review B*, vol. 105, no. 14, p. L140301, 2022.

[49] I. I. Manin, T. Raedschelders, and M. Van den Bergh, *Quantum groups and noncommutative geometry*. Springer, 1988.

[50] M. Fannes, B. Nachtergaele, and R. F. Werner, "Quantum spin chains with quantum group symmetry," *Communications in mathematical physics*, vol. 174, no. 3, pp. 477–507, 1996.

[51] C. Di Franco, M. Paternostro, and M. Kim, "Nested entangled states for distributed quantum channels," *Physical Review A—Atomic, Molecular, and Optical Physics*, vol. 77, no. 2, p. 020303, 2008.

[52] H.-J. Briegel, W. Dür, J. I. Cirac, and P. Zoller, "Quantum repeaters: the role of imperfect local operations in quantum communication," *Physical Review Letters*, vol. 81, no. 26, p. 5932, 1998.

[53] L. Innocenti, H. Majury, T. Giordani, N. Spagnolo, F. Sciarrino, M. Paternostro, and A. Ferraro, "Quantum state engineering using one-dimensional discrete-time quantum walks," *Physical Review A*, vol. 96, no. 6, p. 062326, 2017.

[54] A. Ekert and P. L. Knight, "Entangled quantum systems and the schmidt decomposition," *American Journal of Physics*, vol. 63, no. 5, pp. 415–423, 1995.

[55] U. Schollwöck, "The density-matrix renormalization group in the age of matrix product states," *Annals of physics*, vol. 326, no. 1, pp. 96–192, 2011.

[56] G. Vidal, "Entanglement monotones," *Journal of Modern Optics*, vol. 47, no. 2-3, pp. 355–376, 2000.

[57] V. Vedral, M. B. Plenio, M. A. Rippin, and P. L. Knight, "Quantifying entanglement," *Physical Review Letters*, vol. 78, no. 12, p. 2275, 1997.

[58] M. B. Plenio and S. Virmani, "An introduction to entanglement measures," *arXiv preprint quant-ph/0504163*, 2005.

[59] W. K. Wootters, "Entanglement of formation of an arbitrary state of two qubits," *Physical Review Letters*, vol. 80, no. 10, p. 2245, 1998.

[60] C. H. Bennett, D. P. DiVincenzo, J. A. Smolin, and W. K. Wootters, "Mixed-state entanglement and quantum error correction," *Physical Review A*, vol. 54, no. 5, p. 3824, 1996.

[61] S. A. Hill and W. K. Wootters, "Entanglement of a pair of quantum bits," *Physical Review Letters*, vol. 78, no. 26, p. 5022, 1997.

[62] Y.-X. Wang, L.-Z. Mu, V. Vedral, and H. Fan, "Entanglement rényi α entropy," *Physical Review A*, vol. 93, no. 2, p. 022324, 2016.

[63] H. Zhu, M. Hayashi, and L. Chen, "Coherence and entanglement measures based on rényi relative entropies," *Journal of Physics A: Mathematical and Theoretical*, vol. 50, no. 47, p. 475303, 2017.

[64] H. Li and F. D. M. Haldane, "Entanglement spectrum as a generalization of entanglement entropy: Identification of topological order in non-abelian fractional quantum hall effect states," *Physical Review Letters*, vol. 101, no. 1, p. 010504, 2008.

[65] I. Peschel and V. Eisler, "Reduced density matrices and entanglement entropy in free lattice models," *Journal of physics a: mathematical and theoretical*, vol. 42, no. 50, p. 504003, 2009.

[66] B. Nienhuis, M. Campostrini, and P. Calabrese, "Entanglement, combinatorics and finite-size effects in spin chains," *Journal of Statistical Mechanics: Theory and Experiment*, vol. 2009, no. 02, p. P02063, 2009.

[67] D. Poilblanc, "Entanglement spectra of quantum Heisenberg ladders," *Physical Review Letters*, vol. 105, no. 7, p. 077202, 2010.

[68] J. Schliemann, "Entanglement spectrum and entanglement thermodynamics of quantum hall bilayers at ν= 1," *Physical Review B—Condensed Matter and Materials Physics*, vol. 83, no. 11, p. 115322, 2011.

[69] R. Thomale, D. Arovas, and B. A. Bernevig, "Nonlocal order in gapless systems: Entanglement spectrum in spin chains," *Physical Review Letters*, vol. 105, no. 11, p. 116805, 2010.

[70] N. Regnault, B. A. Bernevig, and F. Haldane, "Topological entanglement and clustering of jain hierarchy states," *Physical Review Letters*, vol. 103, no. 1, p. 016801, 2009.

[71] R. Thomale, A. Sterdyniak, N. Regnault, and B. A. Bernevig, "Entanglement gap and a new principle of adiabatic continuity," *Physical Review Letters*, vol. 104, no. 18, p. 180502, 2010.

[72] A. Chandran, M. Hermanns, N. Regnault, and B. A. Bernevig, "Bulk-edge correspondence in entanglement spectra," *Physical Review B—Condensed Matter and Materials Physics*, vol. 84, no. 20, p. 205136, 2011.

[73] X.-L. Qi, H. Katsura, and A. W. Ludwig, "General relationship between the entanglement spectrum and the edge state spectrum of topological quantum states," *Physical Review Letters*, vol. 108, no. 19, p. 196402, 2012.

[74] F. Pollmann, A. M. Turner, E. Berg, and M. Oshikawa, "Entanglement spectrum of a topological phase in one dimension," *Physical Review B*, vol. 81, no. 6, p. 064439, 2010.

[75] P. Calabrese and A. Lefevre, "Entanglement spectrum in one-dimensional systems," *Physical Review A—Atomic, Molecular, and Optical Physics*, vol. 78, no. 3, p. 032329, 2008.

[76] P. Jordan and E. Wigner, "Über das paulische äquivalenzverbot," *Zeitschrift für Physik*, vol. 47, no. 9, pp. 631–651, 1928.

[77] R. Somma, G. Ortiz, J. E. Gubernatis, E. Knill, and R. Laflamme, "Simulating physical phenomena by quantum networks," *Physical Review A*, vol. 65, no. 4, p. 042323, 2002.

[78] M. A. Nielsen *et al.*, "The fermionic canonical commutation relations and the jordan-wigner transform," *School of Physical Sciences The University of Queensland*, vol. 59, p. 75, 2005.

[79] E. Lieb, T. Schultz, and D. Mattis, "Two soluble models of an antiferromagnetic chain," *Annals of Physics*, vol. 16, no. 3, pp. 407–466, 1961.

[80] J. Pachos and Z. Papic, "Quantifying the effect of interactions in quantum many-body systems," *SciPost Physics Lecture Notes*, p. 004, 2018.

[81] N. Bogoliubov, "On the theory of superfluidity," *J. Phys*, vol. 11, no. 1, p. 23, 1947.

[82] J. Latorre and A. Riera, "A short review on entanglement in quantum spin systems," *Journal of physics a: mathematical and theoretical*, vol. 42, no. 50, p. 504002, 2009.

[83] M.-C. Chung and I. Peschel, "Density-matrix spectra of solvable fermionic systems," *Physical Review B*, vol. 64, no. 6, p. 064412, 2001.

[84] S.-A. Cheong and C. L. Henley, "Many-body density matrices for free fermions," *Physical Review B*, vol. 69, no. 7, p. 075111, 2004.

[85] C. Gómez, M. Ruiz-Altaba, G. Sierra, and M. Ruiz-Altaba, *Quantum groups in two-dimensional physics*, vol. 139. Cambridge University Press Cambridge, 1996.

[86] M. T. Batchelor and C. Yung, "Q-deformations of quantum spin chains with exact valence-bond ground states," *International Journal of Modern Physics B*, vol. 8, no. 25n26, pp. 3645–3654, 1994.

[87] A. Klumper, A. Schadschneider, and J. Zittartz, "Equivalence and solution of anisotropic spin-1 models and generalized tj fermion models in one dimension," *Journal of Physics A: Mathematical and General*, vol. 24, no. 16, p. L955, 1991.

[88] R. A. Santos, F. N. Paraan, V. E. Korepin, and A. Klümper, "Entanglement spectra of the q-deformed affleck-kennedy-lieb-tasaki model and matrix product states," *Europhysics Letters*, vol. 98, no. 3, p. 37005, 2012.

[89] M. T. Batchelor, L. Mezincescu, R. I. Nepomechie, and V. Rittenberg, "q-deformations of the o(3) symmetric spin-1 Heisenberg chain," *Journal of Physics A: Mathematical and General*, vol. 23, no. 4, p. L141, 1990.

[90] A. Klümper, A. Schadschneider, and J. Zittartz, "Groundstate properties of a generalized vbs-model," *Zeitschrift für Physik B Condensed Matter*, vol. 87, no. 3, pp. 281–287, 1992.

[91] T. Quella, "Symmetry-protected topological phases beyond groups: The q-deformed affleck-kennedy-lieb-tasaki model," *Physical Review B*, vol. 102, no. 8, p. 081120, 2020.

[92] C. Dasgupta and S.-k. Ma, "Low-temperature properties of the random Heisenberg antiferromagnetic chain," *Physical Review B*, vol. 22, no. 3, p. 1305, 1980.

[93] D. S. Fisher, "Random transverse field ising spin chains," *Physical Review Letters*, vol. 69, no. 3, p. 534, 1992.

[94] D. S. Fisher, "Critical behavior of random transverse-field ising spin chains," *Physical Review B*, vol. 51, no. 10, p. 6411, 1995.

[95] I. Peschel, "Calculation of reduced density matrices from correlation functions," *Journal of Physics A: Mathematical and General*, vol. 36, no. 14, p. L205, 2003.

[96] T. M. Apostol, *Introduction to analytic number theory*. Springer Science & Business Media, 2013.

[97] D. Spector, "Supersymmetry and the möbius inversion function," *Communications in mathematical physics*, vol. 127, no. 2, pp. 239–252, 1990.

[98] B. Julia, "Statistical theory of numbers," in *Number Theory and Physics: Proceedings of the Winter School, Les Houches, France, March 7–16, 1989*, pp. 276–293, Springer, 1990.

[99] D. Cassettari, G. Mussardo, and A. Trombettoni, "Holographic realization of the prime number quantum potential," *PNAS nexus*, vol. 2, no. 1, p. 279, 2023.

[100] G. Mussardo, "The quantum mechanical potential for the prime numbers," *arXiv preprint cond-mat/9712010*, 1997.

[101] T. Franz, "Quantum correlations and quantum key distribution," 2013.

[102] M. Kunimi and T. Tomita, "Proposal for realizing Heisenberg-type quantum-spin models in Rydberg atom quantum simulators," *arXiv preprint arXiv:2507.22461*, 2025.

[103] H. Kuji, M. Kunimi, and T. Nikuni, "Proposal for realizing quantum-spin systems on a two-dimensional square lattice with Dzyaloshinskii-Moriya interaction by Floquet engineering using Rydberg atoms," *Physical Review A*, vol. 112, no. 2, p. 022614, 2025.

[104] S. Geier, N. Thaicharoen, C. Hainaut, T. Franz, A. Salzinger, A. Tebben, D. Grimshandl, G. Zürn, and M. Weidemüller, "Floquet Hamiltonian engineering of an isolated many-body spin system," *Science*, vol. 374, no. 6571, pp. 1149–1152, 2021.

[105] I. Pitsios, L. Banchi, A. S. Rab, M. Bentivegna, D. Caprara, A. Crespi, N. Spagnolo, S. Bose, P. Mataloni, R. Osellame, *et al.*, "Photonic simulation of entanglement growth and engineering after a spin chain quench," *Nature communications*, vol. 8, no. 1, p. 1569, 2017.

[106] S. N. Santalla, G. Ramírez, S. S. Roy, G. Sierra, and J. Rodríguez-Laguna, "Entanglement links and the quasiparticle picture," *Physical Review B*, vol. 107, no. 12, p. L121114, 2023.

[107] N. S. S. De Buruaga, S. N. Santalla, J. Rodríguez-Laguna, and G. Sierra, "Symmetry protected phases in inhomogeneous spin chains," *Journal of Statistical Mechanics: Theory and Experiment*, vol. 2019, no. 9, p. 093102, 2019.

[108] N. Samos Sáenz de Buruaga, S. N. Santalla, J. Rodríguez-Laguna, and G. Sierra, "Entanglement in noncritical inhomogeneous quantum chains," *Physical Review B*, vol. 104, no. 19, p. 195147, 2021.

[109] M. Aguado, G. Brennen, F. Verstraete, and J. I. Cirac, "Creation, manipulation, and detection of abelian and non-abelian anyons in optical lattices," *Physical Review Letters*, vol. 101, no. 26, p. 260501, 2008.

[110] J.-S. Xu, K. Sun, Y.-J. Han, C.-F. Li, J. K. Pachos, and G.-C. Guo, "Simulating the exchange of Majorana zero modes with a photonic system," *Nature communications*, vol. 7, no. 1, p. 13194, 2016.

[111] Z.-H. Liu, K. Sun, J. K. Pachos, M. Yang, Y. Meng, Y.-W. Liao, Q. Li, J.-F. Wang, Z.-Y. Luo, Y.-F. He, *et al.*, "Topological contextuality and anyonic statistics of photonic-encoded parafermions," *PRX Quantum*, vol. 2, no. 3, p. 030323, 2021.

[112] J. R. Wootton, "Demonstrating non-abelian braiding of surface code defects in a five qubit experiment," *Quantum Science and Technology*, vol. 2, no. 1, p. 015006, 2017.

[113] J. P. Stenger, N. T. Bronn, D. J. Egger, and D. Pekker, "Simulating the dynamics of braiding of Majorana zero modes using an IBM quantum computer," *Physical Review Research*, vol. 3, no. 3, p. 033171, 2021.

[114] C. Nayak, S. H. Simon, A. Stern, M. Freedman, and S. Das Sarma, "Non-abelian anyons and topological quantum computation," *Reviews of Modern Physics*, vol. 80, no. 3, pp. 1083–1159, 2008.

[115] M. Jimbo, "Introduction to the yang-baxter equation," *International Journal of Modern Physics A*, vol. 4, no. 15, pp. 3759–3777, 1989.

[116] P. Kulish and E. Sklyanin, "Solutions of the yang-baxter equation," *Journal of Soviet Mathematics*, vol. 19, no. 5, pp. 1596–1620, 1982.

[117] A. Tounsi, N. E. Belaloui, M. M. Louamri, A. Mimoun, A. Benslama, and M. T. Rouabah, "Systematic computation of braid generator matrix in topological quantum computing," *arXiv preprint arXiv:2307.01892*, 2023.

[118] F. Wilczek, "Magnetic flux, angular momentum, and statistics," *Physical Review Letters*, vol. 48, no. 17, p. 1144, 1982.

[119] F. Wilczek, "Remarks on dyons," *Physical Review Letters*, vol. 48, no. 17, p. 1146, 1982.

[120] V. G. Drinfeld, "Quantum groups," *Zapiski Nauchnykh Seminarov POMI*, vol. 155, pp. 18–49, 1986.

[121] A. Bols and S. Vadnerkar, "Classification of the anyon sectors of kitaev's quantum double model," *arXiv preprint arXiv:2310.19661*, 2023.

[122] A. Kitaev and J. Preskill, "Topological entanglement entropy," *Physical Review Letters*, vol. 96, no. 11, p. 110404, 2006.

[123] R. P. Feynman, "Simulating physics with computers," in *Feynman and computation*, pp. 133–153, cRc Press, 2018.

[124] D. P. DiVincenzo, "The physical implementation of quantum computation," *Fortschritte der Physik: Progress of Physics*, vol. 48, no. 9-11, pp. 771–783, 2000.

[125] J. D. Whitfield, J. Biamonte, and A. Aspuru-Guzik, "Simulation of electronic structure Hamiltonians using quantum computers," *Molecular Physics*, vol. 109, no. 5, pp. 735–750, 2011.

[126] M. Schlosshauer, "Decoherence, the measurement problem, and interpretations of quantum mechanics," *Reviews of Modern physics*, vol. 76, no. 4, pp. 1267–1305, 2004.

[127] G. Bacciagaluppi, "The role of decoherence in quantum mechanics," 2003.

[128] J. Preskill, "Quantum computing in the NISQ era and beyond," *Quantum*, vol. 2, p. 79, 2018.

[129] J. W. Z. Lau, K. H. Lim, H. Shrotriya, and L. C. Kwek, "NISQ computing: where are we and where do we go?," *AAPPS bulletin*, vol. 32, no. 1, p. 27, 2022.

[130] V. Lahtinen and J. Pachos, "A short introduction to topological quantum computation," *SciPost Physics*, vol. 3, no. 3, p. 021, 2017.

[131] Y.-S. Wu, "Braid groups, anyons and gauge invariance," *International Journal of Modern Physics B*, vol. 5, no. 10, pp. 1649–1664, 1991.

[132] G. Moore and N. Read, "Nonabelions in the fractional quantum hall effect," *Nuclear Physics B*, vol. 360, no. 2-3, pp. 362–396, 1991.

[133] S. Das Sarma, M. Freedman, and C. Nayak, "Topologically protected qubits from a possible non-abelian fractional quantum hall state," *Physical Review Letters*, vol. 94, no. 16, p. 166802, 2005.

[134] M. Dolev, M. Heiblum, V. Umansky, A. Stern, and D. Mahalu, "Observation of a quarter of an electron charge at the $\nu = 5/2$ quantum hall state," *Nature*, vol. 452, no. 7189, pp. 829–834, 2008.

[135] N. Read and D. Green, "Paired states of fermions in two dimensions with breaking of parity and time-reversal symmetries and the fractional quantum hall effect," *Physical Review B*, vol. 61, no. 15, p. 10267, 2000.

[136] D. A. Ivanov, "Non-abelian statistics of half-quantum vortices in p-wave superconductors," *Physical Review Letters*, vol. 86, no. 2, p. 268, 2001.

[137] S. Xu, Z.-Z. Sun, K. Wang, L. Xiang, Z. Bao, Z. Zhu, F. Shen, Z. Song, P. Zhang, W. Ren, *et al.*, "Digital simulation of projective non-abelian anyons with 68 superconducting qubits," *Chinese Physics Letters*, vol. 40, no. 6, p. 060301, 2023.

[138] e. a. Andersen, Trond I, "Non-abelian braiding of graph vertices in a superconducting processor," *Nature*, vol. 618, no. 7964, pp. 264–269, 2023.

[139] V. Mourik, K. Zuo, S. M. Frolov, S. Plissard, E. P. Bakkers, and L. P. Kouwenhoven, "Signatures of Majorana fermions in hybrid superconductor-semiconductor nanowire devices," *Science*, vol. 336, no. 6084, pp. 1003–1007, 2012.

[140] E. Dennis, A. Kitaev, A. Landahl, and J. Preskill, "Topological quantum memory," *Journal of Mathematical Physics*, vol. 43, no. 9, pp. 4452–4505, 2002.

[141] H. Bombin and M. A. Martin-Delgado, "Topological quantum distillation," *Physical Review Letters*, vol. 97, no. 18, p. 180501, 2006.

[142] D. Gottesman, "The Heisenberg representation of quantum computers," *arXiv preprint quant-ph/9807006*, 1998.

[143] S. Aaronson and D. Gottesman, "Improved simulation of stabilizer circuits," *Physical Review A—Atomic, Molecular, and Optical Physics*, vol. 70, no. 5, p. 052328, 2004.

[144] C. F. B. Lo, A. Lyons, R. Verresen, A. Vishwanath, and N. Tantivasadakarn, "Universal quantum computation with the s_3 quantum double: A pedagogical exposition," *arXiv preprint arXiv:2502.14974*, 2025.

[145] D. S. Dummit, R. M. Foote, *et al.*, *Abstract algebra*, vol. 3. Wiley Hoboken, 2004.

[146] C. Mochon, "Anyon computers with smaller groups," *Physical Review A*, vol. 69, no. 3, p. 032306, 2004.

[147] S. X. Cui, S.-M. Hong, and Z. Wang, "Universal quantum computation with weakly integral anyons," *Quantum Information Processing*, vol. 14, pp. 2687–2727, 2015.

[148] S. Goel, M. Reynolds, M. Girling, W. McCutcheon, S. Leedumrongwatthanakun, V. Srivastav, D. Jennings, M. Malik, and J. K. Pachos, "Unveiling the non-abelian statistics of $D(S_3)$ anyons via photonic simulation," *arXiv preprint arXiv:2304.05286*, 2023.

[149] S. Bravyi and A. Kitaev, "Universal quantum computation with ideal clifford gates and noisy ancillas," *Physical Review A—Atomic, Molecular, and Optical Physics*, vol. 71, no. 2, p. 022316, 2005.

[150] S. Bravyi and J. Haah, "Magic-state distillation with low overhead," *Physical Review A—Atomic, Molecular, and Optical Physics*, vol. 86, no. 5, p. 052329, 2012.

[151] M. Howard and E. Campbell, "Application of a resource theory for magic states to fault-tolerant quantum computing," *Physical Review Letters*, vol. 118, no. 9, p. 090501, 2017.

[152] V. T. Lahtinen, *Interacting non-Abelian anyons in an exactly solvable lattice model*. University of Leeds, 2010.

[153] X.-W. Luo, Y.-J. Han, G.-C. Guo, X. Zhou, and Z.-W. Zhou, "Simulation of non-abelian anyons using ribbon operators connected to a common base site," *Physical Review A*, vol. 84, no. 5, p. 052314, 2011.

[154] L. Chen, Y. Ren, R. Fan, and A. Jaffe, "A universal circuit set using the s 3 quantum double," *npj Quantum Information*, vol. 11, no. 1, p. 112, 2025.

[155] P. Bonderson, M. Freedman, and C. Nayak, "Measurement-only topological quantum computation," *Physical Review Letters*, vol. 101, no. 1, p. 010501, 2008.

[156] P. Bonderson, M. Freedman, and C. Nayak, "Measurement-only topological quantum computation via anyonic interferometry," *Annals of Physics*, vol. 324, no. 4, pp. 787–826, 2009.

[157] D. Grier and L. Schaeffer, "The classification of clifford gates over qubits," *Quantum*, vol. 6, p. 734, 2022.

[158] Y. Shi, "Both toffoli and controlled-not need little help to do universal quantum computation," *arXiv preprint quant-ph/0205115*, 2002.

[159] M. A. Nielsen and I. L. Chuang, *Quantum computation and quantum information*. Cambridge university press, 2010.

[160] A. Barenco, C. H. Bennett, R. Cleve, D. P. DiVincenzo, N. Margolus, P. Shor, T. Sleator, J. A. Smolin, and H. Weinfurter, "Elementary gates for quantum computation," *Physical review A*, vol. 52, no. 5, p. 3457, 1995.

[161] A. G. Fowler, M. Mariantoni, J. M. Martinis, and A. N. Cleland, "Surface codes: Towards practical large-scale quantum computation," *Physical Review A—Atomic, Molecular, and Optical Physics*, vol. 86, no. 3, p. 032324, 2012.

[162] D. Gottesman, *Stabilizer codes and quantum error correction*. California Institute of Technology, 1997.

[163] E. Knill, "Non-binary unitary error bases and quantum codes," *arXiv preprint quant-ph/9608048*, 1996.

[164] B. Eastin and E. Knill, "Restrictions on transversal encoded quantum gate sets," *Physical review letters*, vol. 102, no. 11, p. 110502, 2009.

[165] N. C. Jones, R. Van Meter, A. G. Fowler, P. L. McMahon, J. Kim, T. D. Ladd, and Y. Yamamoto, "Layered architecture for quantum computing," *Physical Review X*, vol. 2, no. 3, p. 031007, 2012.

[166] P. S. Tarabunga, E. Tirrito, T. Chanda, and M. Dalmonte, "Many-body magic via pauli-markov chains—from criticality to gauge theories," *PRX Quantum*, vol. 4, no. 4, p. 040317, 2023.

[167] B. W. Reichardt, "Quantum universality from magic states distillation applied to css codes," *Quantum Information Processing*, vol. 4, no. 3, pp. 251–264, 2005.

[168] P. Sales Rodriguez, J. M. Robinson, P. N. Jepsen, Z. He, C. Duckering, C. Zhao, K.-H. Wu, J. Campo, K. Bagnall, M. Kwon, *et al.*, "Experimental demonstration of logical magic state distillation," *Nature*, vol. 645, no. 8081, pp. 620–625, 2025.

[169] H. Goto, "Step-by-step magic state encoding for efficient fault-tolerant quantum computation," *Scientific Reports*, vol. 4, no. 1, p. 7501, 2014.

[170] S.-J. Huang and Y. Chen, "Generating logical magic states with the aid of non-abelian topological order," *arXiv preprint arXiv:2502.00998*, 2025.

[171] Y. Kim, M. Sevior, and M. Usman, "Magic state injection on ibm quantum processors above the distillation threshold," *arXiv preprint arXiv:2412.01446*, 2024.

[172] K. Laubscher, D. Loss, and J. R. Wootton, "Universal quantum computation in the surface code using non-abelian islands," *Physical Review A*, vol. 100, no. 1, p. 012338, 2019.

[173] A. Kómár and O. Landon-Cardinal, "Anyons are not energy eigenspaces of quantum double Hamiltonians," *Physical Review B*, vol. 96, no. 19, p. 195150, 2017.

[174] A. Coste, T. Gannon, and P. Ruelle, "Finite group modular data," *Nuclear Physics B*, vol. 581, no. 3, pp. 679–717, 2000.

[175] J. Siehler, "Near-group categories," *Algebraic &; Geometric Topology*, vol. 3, p. 719–775, Aug. 2003.

[176] S. H. Simon, *Topological quantum*. Oxford University Press, 2023.

[177] O. Buerschaper and M. Aguado, "Mapping kitaev's quantum double lattice models to levin and wen's string-net models," *Physical Review B—Condensed Matter and Materials Physics*, vol. 80, no. 15, p. 155136, 2009.

[178] H. Bombin and M. Martin-Delgado, "Family of non-abelian kitaev models on a lattice: Topological condensation and confinement," *Physical Review B*, vol. 78, no. 11, p. 115421, 2008.

[179] J. R. Wootton, *Dissecting topological quantum computation*. University of Leeds, 2010.

[180] I. Cong, M. Cheng, and Z. Wang, "Universal quantum computation with gapped boundaries," *Physical Review Letters*, vol. 119, no. 17, p. 170504, 2017.

[181] S. Bravyi, I. Kim, A. Kliesch, and R. Koenig, "Adaptive constant-depth circuits for manipulating non-abelian anyons," *arXiv preprint arXiv:2205.01933*, 2022.

[182] N. Tantivasadakarn, A. Vishwanath, and R. Verresen, "Hierarchy of topological order from finite-depth unitaries, measurement, and feedforward," *PRX Quantum*, vol. 4, no. 2, p. 020339, 2023.

[183] R. Verresen, N. Tantivasadakarn, and A. Vishwanath, "Efficiently preparing schr\" odinger's cat, fractons and non-abelian topological order in quantum devices," *arXiv preprint arXiv:2112.03061*, 2021.

[184] L. Hormozi, G. Zikos, N. E. Bonesteel, and S. H. Simon, "Topological quantum compiling," *Physical Review B—Condensed Matter and Materials Physics*, vol. 75, no. 16, p. 165310, 2007.

[185] B. Field and T. Simula, "Introduction to topological quantum computation with non-abelian anyons," *Quantum Science and Technology*, vol. 3, no. 4, p. 045004, 2018.

[186] D. Aharonov, V. Jones, and Z. Landau, "A polynomial quantum algorithm for approximating the jones polynomial," in *Proceedings of the thirty-eighth annual ACM symposium on Theory of computing*, pp. 427–436, 2006.

[187] J. L. O'Brien, "Optical quantum computing," *Science*, vol. 318, no. 5856, pp. 1567–1570, 2007.

[188] J. L. O'Brien, A. Furusawa, and J. Vučković, "Photonic quantum technologies," *Nature photonics*, vol. 3, no. 12, pp. 687–695, 2009.

[189] J. Wang, F. Sciarrino, A. Laing, and M. G. Thompson, "Integrated photonic quantum technologies," *Nature photonics*, vol. 14, no. 5, pp. 273–284, 2020.

[190] A. Aspuru-Guzik and P. Walther, "Photonic quantum simulators," *Nature physics*, vol. 8, no. 4, pp. 285–291, 2012.

[191] E. Knill, R. Laflamme, and G. J. Milburn, "A scheme for efficient quantum computation with linear optics," *nature*, vol. 409, no. 6816, pp. 46–52, 2001.

[192] P. Kok, W. J. Munro, K. Nemoto, T. C. Ralph, J. P. Dowling, and G. J. Milburn, "Linear optical quantum computing with photonic qubits," *Reviews of modern physics*, vol. 79, no. 1, pp. 135–174, 2007.

[193] J. Pachos, W. Wieczorek, C. Schmid, N. Kiesel, R. Pohlner, and H. Weinfurter, "Revealing anyonic features in a toric code quantum simulation," *New Journal of Physics*, vol. 11, no. 8, p. 083010, 2009.

[194] T. Dai, Y. Ao, J. Bao, J. Mao, Y. Chi, Z. Fu, Y. You, X. Chen, C. Zhai, B. Tang, *et al.*, "Topologically protected quantum entanglement emitters," *Nature Photonics*, vol. 16, no. 3, pp. 248–257, 2022.

[195] C.-Y. Lu, W.-B. Gao, O. Gühne, X.-Q. Zhou, Z.-B. Chen, and J.-W. Pan, "Demonstrating anyonic fractional statistics with a six-qubit quantum simulator," *Physical Review Letters*, vol. 102, no. 3, p. 030502, 2009.

[196] C. Liu, H.-L. Huang, C. Chen, B.-Y. Wang, X.-L. Wang, T. Yang, L. Li, N.-L. Liu, J. P. Dowling, T. Byrnes, *et al.*, "Demonstration of topologically path-independent anyonic braiding in a nine-qubit planar code," *Optica*, vol. 6, no. 3, pp. 264–268, 2019.

[197] J. Noh, T. Schuster, T. Iadecola, S. Huang, M. Wang, K. P. Chen, C. Chamon, and M. C. Rechtsman, "Braiding photonic topological zero modes," *Nature Physics*, vol. 16, no. 9, pp. 989–993, 2020.

[198] G. Brennen, M. Aguado, and J. I. Cirac, "Simulations of quantum double models," *New Journal of Physics*, vol. 11, no. 5, p. 053009, 2009.

[199] R. Sarkar and T. J. Yoder, "The qudit pauli group: non-commuting pairs, non-commuting sets, and structure theorems," *Quantum*, vol. 8, p. 1307, 2024.

[200] S. Stanisic, N. Linden, A. Montanaro, and P. S. Turner, "Generating entanglement with linear optics," *Physical Review A*, vol. 96, no. 4, p. 043861, 2017.

[201] P. V. Parellada, V. G. i Garcia, J. J. Moyano-Fernández, and J. C. Garcia-Escartin, "No-go theorems for photon state transformations in quantum linear optics," *Results in Physics*, vol. 54, p. 107108, 2023.

[202] N. Goss, A. Morvan, B. Marinelli, B. K. Mitchell, L. B. Nguyen, R. K. Naik, L. Chen, C. Jünger, J. M. Kreikebaum, D. I. Santiago, *et al.*, "High-fidelity qutrit entangling gates for superconducting circuits," *Nature communications*, vol. 13, no. 1, p. 7481, 2022.

[203] X.-M. Ye, Z.-F. Zheng, D.-M. Lu, and C.-P. Yang, "Circuit qed: generation of two-transmon-qutrit entangled states via resonant interaction," *Quantum Information Processing*, vol. 17, no. 4, p. 99, 2018.

[204] L.-X. Cen, B.-P. Hou, and M.-L. Chen, "Implementation of qutrit-based quantum information processing via state-dependent forces on trapped ions," *arXiv preprint quant-ph/0608105*, 2006.

[205] Z. Jin, W.-J. Gong, A.-D. Zhu, S. Zhang, Y. Qi, and S.-L. Su, "Dissipative preparation of qutrit entanglement via periodically modulated rydberg double antiblockade," *Optics Express*, vol. 29, no. 7, pp. 10117–10133, 2021.

[206] C. Schaeff, R. Polster, M. Huber, S. Ramelow, and A. Zeilinger, "Experimental access to higher-dimensional entangled quantum systems using integrated optics," *Optica*, vol. 2, no. 6, pp. 523–529, 2015.

[207] D. Ghosh, T. Jennewein, and U. Sinha, "Entanglement certification and quantification in spatial-bin photonic qutrits," *arXiv preprint arXiv:1909.01367*, 2019.

[208] A. Zeilinger, "General properties of lossless beam splitters in interferometry," *American Journal of Physics*, vol. 49, no. 9, pp. 882–883, 1981.

[209] H. Fearn and R. Loudon, "Quantum theory of the lossless beam splitter," *Optics communications*, vol. 64, no. 6, pp. 485–490, 1987.

[210] M. Reck, A. Zeilinger, H. J. Bernstein, and P. Bertani, "Experimental realization of any discrete unitary operator," *Physical Review Letters*, vol. 73, no. 1, p. 58, 1994.

[211] C. Myers and R. Laflamme, "Linear optics quantum computation: an overview," *arXiv preprint quant-ph/0512104*, 2005.

[212] N. Lütkenhaus, J. Calsamiglia, and K.-A. Suominen, "Bell measurements for teleportation," *Physical Review A*, vol. 59, no. 5, p. 3295, 1999.

[213] L. Vaidman and N. Yoran, "Methods for reliable teleportation," *Physical Review A*, vol. 59, no. 1, p. 116, 1999.

[214] Q. A. Turchette, C. J. Hood, W. Lange, H. Mabuchi, and H. J. Kimble, "Measurement of conditional phase shifts for quantum logic," *Physical Review Letters*, vol. 75, no. 25, p. 4710, 1995.

[215] I. L. Chuang and Y. Yamamoto, "Simple quantum computer," *Physical Review A*, vol. 52, no. 5, p. 3489, 1995.

[216] J. H. Shapiro, "Single-photon kerr nonlinearities do not help quantum computation," *Physical Review A—Atomic, Molecular, and Optical Physics*, vol. 73, no. 6, p. 062305, 2006.

[217] H. Watanabe, M. Cheng, and Y. Fuji, "Ground state degeneracy on torus in a family of zn toric code," *Journal of Mathematical Physics*, vol. 64, no. 5, 2023.

[218] S. Bravyi, M. B. Hastings, and S. Michalakis, "Topological quantum order: stability under local perturbations," *Journal of mathematical physics*, vol. 51, no. 9, 2010.

[219] J.-S. Xu, K. Sun, J. K. Pachos, Y.-J. Han, C.-F. Li, and G.-C. Guo, "Photonic implementation of Majorana-based Berry phases," *Science advances*, vol. 4, no. 10, p. eaat6533, 2018.

[220] S. Bravyi, D. Poulin, and B. Terhal, "Tradeoffs for reliable quantum information storage in 2d systems," *Physical Review Letters*, vol. 104, no. 5, p. 050503, 2010.

[221] H. Gao, K. Wang, D. Qu, Q. Lin, and P. Xue, "Demonstration of a photonic router via quantum walks," *New Journal of Physics*, vol. 25, no. 5, p. 053011, 2023.

[222] B. M. Terhal and G. Burkard, "Fault-tolerant quantum computation for local non-markovian noise," *Physical Review A—Atomic, Molecular, and Optical Physics*, vol. 71, no. 1, p. 012336, 2005.

[223] J.-K. Li, K. Sun, Z.-Y. Hao, J.-H. Liang, J. K. Pachos, L. Byles, J.-S. Xu, Y.-J. Han, C.-F. Li, and G.-C. Guo, "High-fidelity realisation of CNOT gate in Majorana-based optical platform," *arXiv preprint arXiv:2508.14641*, 2025.

[224] F. Mezzadri, "How to generate random matrices from the classical compact groups," *arXiv preprint math-ph/0609050*, 2006.

[225] P. Hayden, D. Leung, P. W. Shor, and A. Winter, "Randomizing quantum states: Constructions and applications," *Communications in Mathematical Physics*, vol. 250, no. 2, pp. 371–391, 2004.

[226] A. M. Steane, "Overhead and noise threshold of fault-tolerant quantum error correction," *Physical Review A*, vol. 68, no. 4, p. 042322, 2003.

[227] E. Knill, "Scalable quantum computing in the presence of large detected-error rates," *Physical Review A—Atomic, Molecular, and Optical Physics*, vol. 71, no. 4, p. 042322, 2005.

[228] M. D. Horner, "Emergent spacetime in quantum lattice models," *arXiv preprint arXiv:2212.12548*, 2022.

[229] A. Daniel, T. Bhore, J. K. Pachos, C. Liu, and A. Hallam, "Quantum teleportation between simulated binary black holes," *arXiv preprint arXiv:2503.10761*, 2025.

[230] R. J. Garcia, K. Bu, and A. Jaffe, "Resource theory of quantum scrambling," *Proceedings of the National Academy of Sciences*, vol. 120, no. 17, p. e2217031120, 2023.

[231] E. Iyoda and T. Sagawa, "Scrambling of quantum information in quantum many-body systems," *Physical Review A*, vol. 97, no. 4, p. 042330, 2018.

[232] P. Hosur, X.-L. Qi, D. A. Roberts, and B. Yoshida, "Chaos in quantum channels," *Journal of High Energy Physics*, vol. 2016, no. 2, pp. 1–49, 2016.

[233] A. Nahum, S. Vijay, and J. Haah, "Operator spreading in random unitary circuits," *Physical Review X*, vol. 8, no. 2, p. 021014, 2018.

[234] A. Touil and S. Deffner, "Quantum scrambling and the growth of mutual information," *Quantum Science and Technology*, vol. 5, no. 3, p. 035005, 2020.

[235] L. Lao and B. Criger, "Magic state injection on the rotated surface code," in *Proceedings of the 19th ACM International Conference on Computing Frontiers*, pp. 113–120, 2022.

[236] M. A. Nielsen, "Cluster-state quantum computation," *Reports on Mathematical Physics*, vol. 57, no. 1, pp. 147–161, 2006.

[237] D. Litinski, "A game of surface codes: Large-scale quantum computing with lattice surgery," *Quantum*, vol. 3, p. 128, 2019.

[238] C. Mochon, "Anyons from nonsolvable finite groups are sufficient for universal quantum computation," *Physical Review A*, vol. 67, no. 2, p. 022315, 2003.

[239] M. Ringbauer, M. Meth, L. Postler, R. Stricker, R. Blatt, P. Schindler, and T. Monz, "A universal qudit quantum processor with trapped ions," *Nature Physics*, vol. 18, no. 9, pp. 1053–1057, 2022.

[240] P. Hrmo, B. Wilhelm, L. Gerster, M. W. van Mourik, M. Huber, R. Blatt, P. Schindler, T. Monz, and M. Ringbauer, "Native qudit entanglement in a trapped ion quantum processor," *Nature Communications*, vol. 14, no. 1, p. 2242, 2023.

[241] N. Goss, S. Ferracin, A. Hashim, A. Carignan-Dugas, J. M. Kreikebaum, R. K. Naik, D. I. Santiago, and I. Siddiqi, "Extending the computational reach of a superconducting qutrit processor," *npj Quantum Information*, vol. 10, no. 1, p. 101, 2024.

[242] V. Tripathi, N. Goss, A. Vezvaee, L. B. Nguyen, I. Siddiqi, and D. A. Lidar, "Qudit dynamical decoupling on a superconducting quantum processor," *Physical Review Letters*, vol. 134, no. 5, p. 050601, 2025.

[243] G.-C. Wick, "The evaluation of the collision matrix," *Physical Review*, vol. 80, no. 2, p. 268, 1950.

[244] L. G. Molinari, "Notes on Wick's theorem in many-body theory," *arXiv preprint arXiv:1710.09248*, 2017.

[245] W. Pfeifer, "The Lie algebras su(N)," in *The Lie Algebras su (N) An Introduction*, pp. 15–21, Springer, 2003.

[246] P. P. Kulish and N. Y. Reshetikhin, "Quantum linear problem for the sine-gordon equation and higher representations," *Journal of Soviet Mathematics*, vol. 23, no. 4, pp. 2435–2441, 1983.

[247] V. G. Drinfel'd, "Hopf algebras and the quantum yang-baxter equation," in *Soviet Math. Dokl.*, vol. 32, pp. 254–258, 1985.

[248] M. Jimbo, "A q-difference analogue of u (g) and the yang-baxter equation," *Letters in Mathematical Physics*, vol. 10, no. 1, pp. 63–69, 1985.

[249] M. Jimbo, "Quantumr matrix for the generalized toda system," *Communications in Mathematical Physics*, vol. 102, no. 4, pp. 537–547, 1986.

[250] M. Jimbo, "A q-analogue of u (g [(n+ 1)), hecke algebra, and the yang-baxter equation," *Letters in Mathematical Physics*, vol. 11, no. 3, pp. 247–252, 1986.

[251] C. Kassel, *Quantum groups*, vol. 155. Springer Science & Business Media, 2012.

[252] S. Majid, *Foundations of quantum group theory*. Cambridge university press, 2000.

[253] L. Faddeev, "How algebraic bethe ansatz works for integrable model," *arXiv preprint hep-th/9605187*, 1996.

[254] V. Chari and A. N. Pressley, *A guide to quantum groups*. Cambridge university press, 1995.

[255] A. Klümper, "The spin-1/2 heisenberg chain: thermodynamics, quantum criticality and spin-peierls exponents," *The European Physical Journal B-Condensed Matter and Complex Systems*, vol. 5, no. 3, pp. 677–685, 1998.